Doublet microtubule inner proteins exhibit a stabilizing and regulatory role in the ciliary axoneme

Ahmad Abdelzaher Zaki Khalifa

Anatomy and Cell Biology

McGill University

Montreal, Quebec, Canada

December 2019

A thesis submitted to McGill University in partial fulfillment of the requirements of the degree of Master of Science

Table of contents

List of figures

Abstract

Microtubules are tubular structures involved in structural support, microtubule-based transport and the organization of organelles. The building blocks of the microtubule, the α- and β-tubulin heterodimers, polymerize into a variety of tubular structures such as singlet, doublet and triplet microtubules. Doublet microtubules, which consist of a complete 13-protofilament A-tubule and a partial 10-protofilament B-tubule, exist in the cilia where high stability is required for ciliary beating and function. The doublet microtubule maintains its stability through the binding of microtubule inner proteins in the lumen of the A- and B-tubules and via unique interactions at its two junctions, where the A- and B-tubules meet.

Here, I present the complete answer regarding the identity, localization and structure of the doublet microtubule inner junction proteins. I identified two previously unknown inner junction proteins FAP276 and FAP106 and an inner-junction associated protein, FAP126. I performed atomic modeling of all such proteins, which shows that those three, together with FAP52 and inner junction proteins FAP20 and PACRG form an interaction hub at the inner junction, which involves tubulin's sites for post-translational modifications.

I also identified and performed atomic modeling of two homologs of the Rib43a family of proteins in the lumen of the A-tubule. The atomic models reveal, for the first time, the binding of a native protein to the taxane-binding pocket, where taxol and microtubule-stabilizing drugs are known to bind. I further show that Rib43a appear to have a regulatory role in ciliary waveform, besides its potential stabilizing effect.

Résumé

Les microtubules sont des fibres macromolécules impliquées dans l'intégrité structurale des cellules, le transport intracellulaire, et l'organization des organelles. Les microtubules se présentent sous la forme de microtubule simple, ou sous la forme de doublets ou de triplets. Ils sont formés à partir de hétérodimères de tubulines composées de tubiline α et de tubuline β. Les doublets de microtubules sont la conséquence de l'assemblage d'un tubule-A composé de 13 protofilaments, et un microtubule partiel composé de 10 sous-unités, le tubule-B. L'axe moteur des cils et des flagelles sont tous deux consitués d'un doublet de microtubules et tirent bénéfice de la stabilité intrinsèque de ceux-ci. Cette stabilité est le fruit de l'intéraction entre les protéines intaluminales, ainsi que des intéractions aux deux sites de jonction entre les tubules A et B.

Je présente ici un portrait complet concernant l'indentité, la localisation et la structure des protéines composant la region de jonction du doublet de microtubules. Mes travaux ont permis d'identifier deux nouvelles protéines de la jonction interne, FAP276 et FAP106, et une nouvelle proteine associée à la jonction interne, FAP126. J'ai par la suite procédé à la modélisation à l'échelle atomique de la structure de ces trois protéines, de FAP52 et des protéines de la jonction interne, FAP20 et PACGR. Ces travaux ont révélés que ces protéines, situées à la jonction interne, constituaient un multiplex d'interaction impliqué dans la modification post-traductionielles à plusieurs sites des sous-unitées de tubuline.

J'ai aussi identifié et procédé à la modélisation à l'échelle atomique de deux protéines de la famille des protéines Rib43a. Rib43a sont des proteines lumenales du tubule-A et nos efforts de modélisation à l'échelle atomique nous ont permis de révéler, qu'elles étaient capables de lier le site de liaison aux taxanes de la tubuline, qui jusqu'à présent était supposé être exclusif au taxol ou à d'autres drogues stabilisant les microtubules. Mise à part de stabiliser les microtubules, j'ai également démontré que Rib43 pourrait aussi avoir un rôle sur la fonction ondulatoire des cils.

Acknowledgements

This thesis was supported by the Al-Ghurair foundation for education and CIHR funding from my supervisor's fund (Dr. Khanh Huy Bui, CIHR PJT-156354).

I would like to thank Dr. Khanh Huy Bui, who constantly had an open door for continuous and direct communication throughout my thesis. His relentless supervision, scrutinizing critiques and attention to detail surely elevated my skillset to a higher level. I would like to thank my mentor Dr. Joaquin Ortega and committee members Dr. Javier Vargas and Dr. Jean Francois Trempe for their friendliness, approachability and valuable feedback on my work. I want to thank Dr. Alba Guarné for her expert opinion and valuable feedback on various work.

I would like to thank all members of the Bui lab, particularly Dr. Muneyoshi Ichikawa for cryo-electron microscopy supervision, Daniel Dai, Shun Kai Yang and Corbin Black for miscellaneous help. I want to thank Dr. Simone Veyron from the Trempe lab and Dr. Vikash Jha from the Ortega lab for help with molecular modeling. I want to thank Dr. Eric Boucher for translating the abstract of this thesis to the French language.

I want to dedicate this thesis to the memory of my father, chief engineer Abdelzaher Zaki Khalifa, who was a first-generation university student, a role model and a source of inspiration and pride for me throughout my life.

Preface

Contribution to original knowledge

In this manuscript-based thesis, I present new insights on the architecture of the doublet microtubule, the main component of a macromolecular machine with important implications in human health, which is the cilia. Two manuscripts are described here:

I. Khalifa, A., M. Ichikawa, D. Dai, S. Kubo, C. Black, K. Peri, T. S. McAlear, S. Veyron, S. K. Yang, J. Vargas, S. Bechstedt, J.-F. Trempe and K. H. Bui (2019). "The inner junction complex of the cilia is an interaction hub that involves tubulin post-translational modifications." bioRxiv: 774695.

II. Ichikawa, M., A. A. Z. Khalifa, S. Kubo, D. Dai, K. Basu, M. A. F. Maghrebi, J. Vargas and K. H. Bui (2019). "Tubulin lattice in cilia is in a stressed form regulated by microtubule inner proteins." Proceedings of the National Academy of Sciences 116(40): 19930-19938.

The doublet microtubule is a remarkably stable microtubule-based structure that forms the outer circumference of the cilia. Cilia are very important macromolecular structures that function in embryonic development, cell signaling and as a mechanical propeller for driving the sperm motility and moving the mucous and fluids around the cell in the lung, brain, kidney, inner ear and many other tissues. Defects in the cilia lead to disorders with heterogenous phenotypes that are hard to characterize and understand. Studying the structure of the cilia is, therefore, essential to achieve a molecular understanding of such disorders and develop therapy.

The doublet microtubule is composed of a partial 10-protofilament B-tubule docked on top of a complete 13-protofilament A-tubule. This creates two junctions between the two tubules, whose structural properties are essential for doublet microtubule stability and integrity during ciliary beating and movement. This stability is often attributed to a unique feature of the doublet microtubule, which is the binding of microtubule inner proteins in both the lumens of the A- and B- tubules.

In the first manuscript, I identified three previously unknown proteins, FAP276, FAP106 and FAP126 that are part of the inner junction, thus revealing the complete identity and localization of the doublet microtubule inner junction proteins. Furthermore, I performed atomic modeling of all the proteins of the inner junction, PACRG, FAP20, FAP52 as well as the three proteins mentioned

above, thus providing new insights into the inner junction interactions, microtubule inner proteins and doublet microtubule architecture at the atomic level.

In the second manuscript, I identified two electron densities in the lumen of the A-tubule as two homologs that belong to the Rib43a family of proteins. The atomic modeling of such proteins revealed the first evidence of i) a native microtubule inner protein that binds to the taxane-binding pocket, where taxol and microtubule stabilizing drugs are known to bind, thus revealing a potential new mechanism that helps stabilize the doublet microtubule and ii) a microtubule inner protein that directly alter the tubulin lattice architecture.

Contribution of authors

I. Khalifa, A., M. Ichikawa, D. Dai, S. Kubo, C. Black, K. Peri, T. S. McAlear, S. Veyron, S. K. Yang, J. Vargas, S. Bechstedt, J.-F. Trempe and K. H. Bui (2019). "The inner junction complex of the cilia is an interaction hub that involves tubulin post-translational modifications." bioRxiv: 774695.

Contribution of Khalifa, A.: all figures except for what is to follow, cryo-electron microscopy data processing and data analysis with help of Bui, K. H., all model building, atomic refinement and structure analysis. Ichikawa, M. (post-doctoral fellow): Figure 2.8.1, Figure 2.8.6 F, Figure 2.8.7 B and Figure 2.9.1, the doublet isolation and purification and cryo-electron microscopy. Dai, D.: Figure 2.8.6 G and H, Figure 2.9.6 C-E and mass spectrometry (Table 1, Table 2 and Supplementary Table 1). Khalifa, A., Bui, K. H. Ichikawa, M. and Dai, D. contributed to the writing of the manuscript with the following percentages: 40%, 40%, 10% and 10%, respectively. Other co-authors contributed intellectually to the discussion of the current manuscript.

II. Ichikawa, M., A. A. Z. Khalifa, S. Kubo, D. Dai, K. Basu, M. A. F. Maghrebi, J. Vargas and K. H. Bui (2019). "Tubulin lattice in cilia is in a stressed form regulated by microtubule inner proteins." Proceedings of the National Academy of Sciences 116(40): 19930-19938.

Contribution of Khalifa, A.: Figure 3.10.2 A and F-K, Figure 3.10.3, Figure 3.10.5 B-H, except for panel F, Figure 3.11.2, Figure 3.11.3 A-J and Figure 3.11.5 D and E, cryo-electron microscopy data processing and data analysis with help of Bui, K. H., all model building and atomic refinement. Kubo, S.: molecular dynamics simulation and analysis (Figure 3.11.3 K-

N). Ichikawa, M. (post-doctoral fellow): the rest of the figures and tables, the doublet isolation and purification and cryo-electron microscopy. Dai, D. and Maghrebi, M. A. F. helped with cryo-EM data processing. Basu, K. helped with cryo-EM data collection. Khalifa, A., Bui, K. H. Ichikawa, M. and Dai, D. contributed to the writing of the manuscript with the following percentages: 30%, 30%, 30% and 10%, respectively.

List of abbreviations

Cryo-EM	Cryo-electron microscopy
Doublet	Doublet microtubule
PF	Protofilament
MIP	Microtubule inner protein
IFT	Intra-flagellar transport
PCD	Primary ciliary dyskinesia
PACRG	PArkin-CoRegulated Gene
FAP	Flagella-associated protein
ATP	Adenosine triphosphate
Chlamydomonas	*Chlamydomonas reinhardtii*
Tetrahymena	*Tetrahymena thermophila*
Rib43a-S	Rib43a-short
Rib43a-L	Rib43a-long
Tubulin	α- and β-tubulin heterodimer

Introduction, rational and objectives

Cilia and flagella are cellular structures that perform a plethora of vital functions. Their role ranges from cell motility to cell signaling and embryonic development [1-3]. Defects in the cilia and flagella are known to cause many disorders such as infertility, chronic respiratory problems, hydrocephalus, organ laterality defects, retinal dystrophy, renal abnormalities, anosmia, hearing loss, obesity, hepatic disease, ataxia, brain malformation, epilepsy, mental disability and skeletal anomalies [4]. Understanding the structure of cilia and flagella is, therefore, essential to understand and tackle such disorders.

The structure of cilia and flagella is conserved by evolution [5]. The motile cilia and flagella are composed of nine doublet microtubules (doublet) surrounding a central pair of singlet microtubules, which are absent in non-motile cilia (Figure 1.5.1B) [6]. The doublet consists of a complete A-tubule and a partial B-tubule docked on top of it (Figure 1.5.1E).

One of the unique features of the doublet is its remarkable stability. This stability was recently attributed to the binding of microtubule inner proteins (MIPs) in the lumens of its A- and B-tubules [7, 8] and the structural properties of its junctions, where the A- and B-tubules meet (Figure 1.5.2A, B) . The identities, localization, structure and mechanism of action of such proteins, however, remain undetermined to date. Furthermore, the nature of the two junctions between the A- and B-tubules of the doublet and the mechanism by which the junctions maintain their integrity during ciliary beatings remain unknown to date. Therefore, the objectives of this thesis are to:

I. Produce an atomic structure of the doublet microtubule inner junction proteins by cryo-electron microscopy.
II. Identify and produce atomic structures of certain microtubule inner proteins, to study their function, the order of assembly and their interactions with the tubulin lattice.

In contrast to X-ray crystallography, cryo-electron microscopy (cryo-EM) allows the structure determination of large and flexible *ex vivo* structures that are isolated from the cell [9]. The recent advances in cryo-EM now facilitate the generation of near-atomic resolution electron density maps in the range of 3 to 5 Å [10-13]. These resolutions can be sufficient to build atomically accurate models which would open a window to investigate the protein function. In addition, the structure conservation between the human cilia and the cilia and flagella of the model organisms used in

this study: *Chlamydomonas reinhardtii* and *Tetrahymena thermophila*, their well-studied genetics and ease of culturing and maintenance [14, 15] make them excellent models to study the ciliary ultrastructure and tackle the objectives of my thesis. Furthermore, comparing the structure in two species provide an opportunity to compare the structural similarities and differences, which would help to infer protein function.

Chapter 1: Literature review

1.1 Cilia and flagella

Cilia and flagella are hair-like structures that emerge from a modified centriolar structure, termed the basal body (Figure 1.5.1C), to perform vital functions in different tissues and organisms. Historically, they were given two different names based on their external morphology before their structures were studied. Cilia is the term describing the numerous short hair-like structures, which are typically found on the inner mucosa of the lung. The word flagella were used to refer to only one or two of such structures that had a significantly longer length, like the tail of the sperm, Due to the identical structure and functions of the cilia and flagella, I will be using the word "cilia" to refer to both.

Cilia are known to be of two types, motile cilia and non-motile cilia, which are also known as primary or sensory cilia. The length and diameter of the motile and non-motile cilia vary greatly between different tissues and cell types. Depending on its type and localization, the cilia possess a range of functions, from cell motility to embryonic development and cell signaling [1-3]. Single-celled protists such as *Chlamydomonas* and *Tetrahymena*, the epithelial lining of the lungs and the sperm tail are three of the most classic examples of where the motile cilia can be found. Motile cilia further exist in epithelial cells lining the oviduct, the middle ear, in ependymal cells of the brain ventricles where they move the cerebrospinal fluid [16] and in the primitive node, where they function in directing the morphogens that establish left-right body symmetry during embryonic development [17]. Non-motile cilia, on the other hand, are a lot more ubiquitous and exist in many types of cells in the human body [6]. The most classic examples of non-motile cilia are the photoreceptor cells and olfactory neurons cilia.

The primary function of motile cilia is locomotion. Locomotion occurs directly in the propulsion of the sperm and single-celled organisms by the different waveforms that are associated with the cilia. Locomotion also occurs indirectly by moving the fluids and mucous surrounding stationary cells in different tissues and cell types. Primary or sensory cilia, on the other hand, act as sensory organelles that receive external signals from the environment and transmit it to the cell to regulate

a variety of functions [18]. The review by Mitchison and Valente presents a more thorough discussion of both motile and non-motile ciliary functions [19].

The importance of the cilia, their diverse functions and implications in disease gave rise to multiple model organisms to study their structures. The model organisms to study the cilia include the nematode *Caenorhabditis elegans*, the algal protist *Chlamydomonas reinhardtii*, the ciliates *Paramecium* and *Tetrahymena*, and the kinetoplastid *Trypanosoma [*20]. Despite their hard-to-manipulate genetics, mammal and vertebrate model organisms such as mice, zebrafish and *Xenopus* are also used to study cilia [20]. When it comes to studying the cilia, every model organism has its advantages and disadvantages. For example, genetic studies are easier in *C. elegans*, *Xenopus* is a great model to study the cilia *in vivo* while *Trypanosoma* is the model organism of choice to test ciliary gene functions [20]. *Chlamydomonas* and *Tetrahymena*, on the other hand, are easy to grow and culture, give sufficient yield of easy-to-isolate cilia that maintain intact ultrastructure and have a high degree of conservation with mammalian cilia [14, 15]. In addition, *Chlamydomonas* has a well-studied flagellar proteome and an expanding mutant library, which would facilitate studies of the ciliary ultrastructure.

1.2 Structure and formation of the cilia

The structure of the cilia is conserved by evolution [5]. The motile cilium is composed of an arrangement of nine doublet microtubules (DMT) surrounding a central pair of singlet microtubules, which are missing in the non-motile cilium (Figure 1.5.1B) [6]. Nodal cilia are an exception as it lacks the central pair [21]. The nine doublets arrangement without the surrounding plasma membrane is commonly referred to as the axoneme (Figure 1.5.1B). The doublets of the cilium are connected via the nexin-dynein regulatory complex, which restricts their sliding resulting in a bending motion (Figure 1.5.2A) [22]. The beating of the cilium itself is driven by axonemal dyneins, which differ from cytoplasmic dyneins. Axonemal dyneins are anchored to the doublet microtubules on two sides, outwards and inwards (Figure 1.5.2A, B), and its activation via Adenosine triphosphate (ATP) causes the doublets to slide past one another generating the ciliary waveforms [23].

The formation of the cilium (ciliogenesis) is a complex process that involves multiple signaling pathways and shuttling machinery during assembly and disassembly. The shuttling machinery involved in ciliogenesis is known as the intra-flagella transport system (IFT). The IFT is composed of two subcomplexes: A and B, accessory proteins that help IFT assembly at the ciliary base called the BBSome, and kinesin type 2 and cytoplasmic dynein (type 2) as the anterograde and retrograde transport motors, respectively [24-26]. IFT proteins run on tracks along the axonemal length and carry cargo towards the tip of the cilium and back towards the minus end during assembly and disassembly, respectively.

Ciliogenesis starts with the transformation of the mother centriole of the centrosome into a structure that anchors the cilium to the cell body, known as the basal body (Figure 1.5.1C) [27]. The basal body remains connected to the daughter centriole of the centrosome by a structure termed the "rootlet" (Figure 1.5.1D and iv, respectively) [27]. The ciliary membrane is a continuation of the plasma membrane; however, it exhibits multiple modifications and ultrastructure suited towards ciliary function. The membrane of the cilia has multiple receptors and ion channels that can receive signals and transmit molecules into the cell [18]. At the base of the ciliary, multiple protein structures such as the Y shaped structure, the distal appendages and sub-distal appendages (Figure 1.5.1C: i, ii and iii), act as a gateway which establishes cellular compartmentalization and controls the passage of signaling molecules, proteins and IFT cargo as they enter and exit the ciliary compartment [28].

1.3 Cilia in disease

Our expanding knowledge of ciliary genes and proteins narrowed the gap between previously known disease phenotypes and their unknown disease etiology [29]. As a consequence, multiple review articles emerged recently to better describe the disorders that arise from both motile and non-motile ciliary dysfunctions. Such disorders are collectively grouped under the term "ciliopathies" [4, 19, 30, 31]. Since ciliopathies can occur due to defects in ciliary genes or non-ciliary proteins, they can be classified into first-order and second-order ciliopathies, respectively [4]. Another way is to describe ciliopathies is to classify them into motile and non-motile ciliopathies, depending on the type of cilia involved in the disease [4].

Motile ciliopathies are grouped under the term “primary ciliary dyskinesia (PCD)” [32]. PCD is an autosomal recessive disorder of a heterogeneous origin. It involves 37 currently known genes, which are expanding [32]. The most common cause of the disorder is a mutation in the dynein components, which is the main motor for ciliary motility, or the central apparatus [32]. PCD results in phenotypes such as infertility and bronchitis due to the loss of motility of the sperm and the accumulation of mucus in the lungs, in addition to other phenotypes such as hydrocephaly, *situs inversus* and the loss of hearing [4]. It is logical to think that mutations in the recently identified ciliary proteins: FAP20, FAP52 and PACRG [7, 33, 34], which impact ciliary motility, will result in PCD if it existed in patients. In fact, the gene deletion of the human ortholog of FAP52 has been shown to cause *situs inversus* in patients [35].

Since non-motile cilia are more ubiquitous and have a broader range of sensory functions, non-motile ciliopathies comprise a larger group of disorders, which have a multi-phenotypic presentation. The underlying etiologies of non-motile ciliopathies can range from defects in cilia formation and length maintenance to mutations in the signal transduction and ciliary trafficking components [4]. Although motile cilia can also perform a sensory function, the phenotypic presentation of PCD is quite distinct from non-motile ciliopathies [4].

Given the non-motile cilia’s role in Hedgehog signaling, an essential developmental signaling pathway, it can lead to many developmental diseases [4]. While this can occur due to mutations in components such as the Hedgehog receptor PTCH1 of the ciliary membrane, the majority of such disorders arise from aberrations in IFT and BBsome components, which the Hedgehog signal transduction depends on [4]. Such disorders include polydactyly in Bardet–Biedl syndrome and defects of the neural tube in Meckel syndrome, which are multifactorial syndromes themselves [4]. The main phenotypic presentations of IFT defects are skeletal abnormalities due to Hedgehog’s involvement in bone formation and maturation [4, 19].

In addition, the non-motile cilia in the kidney play a sensory role of urine composition, flow and osmolarity [19]. A variety of defects in such sensing mechanisms, which involves multiple signaling pathways, can lead to polycystic kidney disease and nephronophthisis [19]. On the other hand, the interruption of retinal and olfactory sensory ciliary at varying nodes leads to phenotypes such as retinal degeneration and the lack of the sense of smell (anosmia) [4]. While the cilia can

have an intact structure in syndromes that result from signaling defects, usually the signaling defects further affect key ciliary structures such as the basal body and the transition zone [4].

The non-motile ciliopathies are indeed plenty, and their phenotypic presentation includes syndromes that affect the brain, pancreas, liver and other organ systems [19]. Review articles [4, 19, 30, 31] present a more thorough discussion of non-motile ciliopathies and possible underlying mechanisms, which are beyond the subject of this thesis. However, the most apparent fact is that the complexity and heterogeneity of ciliopathies mandates a necessity to study the structure of the cilia, its protein composition and interactions in order to understand, characterize and tackle all such disorders.

1.4 The doublet microtubule

Similar to singlet microtubules, the building blocks of the ciliary doublet microtubule are the α- and β-tubulin heterodimers. The α- and β-tubulin heterodimers polymerize longitudinally to form protofilaments (PFs), which associate laterally to form the cylinder-like hollow microtubule (Figure 1.5.1F). The α- and β-tubulin (tubulin) heterodimers is composed of two monomers: α-tubulin and β-tubulin (Figure 1.5.3A, B). The luminal surface of tubulin contains the loops involved in lateral interactions: the m-loop of one tubulin monomer and the H1'-S2 and H2-S3 loops of the adjacent monomer [36] and the K40 loop of α-tubulin, which is the sole site of luminal post-translational modifications (acetylation) (Figure 1.5.3B) [37]. The C-termini of both α- and β-tubulin face the outer surface of the microtubule and are the sites for a variety of other post-translational-modifications (Figure 1.5.3A) [38]. To date, there is no structure of any of the tubulin's sites for post-translational modifications due to their flexibility.

The doublet microtubule, as the name suggests, is composed of two microtubules fused together: a complete 13-PF A-tubule and a partial 10-PF B-tubule docked on top of it (Figure 1.5.1E) [39]. Like the microtubule, the doublet also possesses directional polarity; its distal end is dubbed the plus end, while the proximal end is referred to as the minus end. Besides the nexin-dynein regulatory complex, radial spokes proteins and axonemal dynein, there are numerous other proteins that associate with the doublet microtubule (Figure 1.5.2B). Most of these proteins bind inside the lumen of the A- and B-tubules and are thought to be important for ciliary function and stability [8]. The stability of the doublet is, indeed, one of its remarkable features. The doublet can withstand low temperatures and high salt concentration treatments [8]. Furthermore, the doublet's

stability is most evident when contrasted to cytoplasmic microtubules, which often undergo assembly and disassembly in a process referred to as the dynamic instability.

The doublet also possesses varying degrees of stability throughout the entire structure. Early studies showed that increasing detergent concentrations solubilize the doublet in the following order: i) the outer B-tubule wall, ii) the remainder of the B-tubule, iii) the outer A-tubule wall and iv) the remainder of the A-tubule [40]. Finally, the remaining structure composed of PF A11, A12 and A13 makes the most stable part of the doublet [40]. This structure is often referred to as the PF ribbon.

1.4.1 Microtubule inner proteins

MIPs were first observed as electron-dense regions in early electron microscopy studies of the neurons and axoneme [41-44]. Cryo-electron tomography studies allowed the visualization of clear densities in the lumen of the A- and B-tubules of the doublet microtubule (Figure 1.5.2B) [45-47]. The near-atomic resolution details obtained by single particle analysis of the doublet microtubule allowed the better characterization of MIP localization, periodicity, architecture and topology [48]. MIPs are believed to have a stabilizing effect on the doublet evident by its long-lived nature compared to singlet microtubules [7, 8]. This led to an increased interest to uncover the MIP identities and study their localization and function. The stability of the PF ribbon, in particular, gained more attention leading to multiple biochemical, proteomic and cryo-electron microscopy studies to identify their protein composition. The study by Linck et al. narrowed down the proteins of the ribbon region to two classes: i) tektins and ii) ribbon proteins such as Rib43 and Rib72 [49].

From recent cryo-electron tomography studies, only a handful of MIPs have been identified and mapped to the doublet microtubule. FAP85 was identified and mapped to the A-tubule near PF A7 in *Chlamydomonas* [50]. Rib72A and Rib72B were also identified as A-tubule MIPs, in *Tetrahymena,* that bind near PF A5, although there were multiple missing densities in various places of the A-tubule associated with Rib72KO as well [51]. FAP52 and FAP45, on the other hand, were identified as B-tubule MIPs that bind in the region between B7 and B10 in *Chlamydomonas* [7]. Most of the remaining densities inside the lumens of the A- and B-tubules remain unknown to date. Despite identifying the previous MIPs, there are no known atomic structures for any of them to confirm and explain their role, assembly, mechanism of action and mode of binding onto the tubulin lattice.

1.4.2 The doublet's outer and inner junctions

The nature of the junctions between the A and B tubules of the doublet is an ongoing topic of research [52]. The canonical lateral interactions between adjacent PFs in the doublet are mediated by loop-loop interactions (Figure 1.5.3B) [36]. The outer junction, however, involve non-canonical three α-β-tubulin dimers interactions, while the inner junction is made of non-tubulin proteins (Figure 1.5.2B) [47, 52]. Only a few candidates have been identified as inner junction proteins of the doublet [33]. From biochemical and transmission electron microscopy studies, FAP20 was confirmed to be an inner junction protein [33]. The proteins tektin and PACRG showed decreased levels in FAP20null mutants suggesting they are also inner junction proteins or have assembly dependence on FAP20. Mutations in inner junction proteins can cause functional defects. In *Chlamydomonas*, FAP20 knockout leads to a phenotype that cannot swim with flagella that shows splitting, fraying and lack of stability [33].

The PACRG gene shares a bi-directional promotor with the parkin gene [53, 54], which is implicated in Parkinson's disease. Past studies in *Chlamydomonas* suggests that PACRG binds to microtubules and tubulin dimers in vitro, and mainly localizes at the wall of the doublet [55]. More recent studies showed that PACRG indeed has cilia associated function [56, 57]. In 2019, a cryo-electron tomography study by Dymek et al. confirmed that both FAP20 and PACRG form the doublet's inner junction in *Chlamydomonas reinhardtii* [34].

PACRG, the better-studied protein of the two, appears to be involved in many vital ciliary functions. The gene deletion of PACRG was identified as the cause of sterility in quaking viable mice, while its exogenous expression resulted in the restoration of spermiogenesis [58]. In a different study, PACRG gene deletion was associated with defective ciliary motility in ependymal cells and hydrocephalus in quaking viable mice [59]. PACRG-morpholino knockdown in Xenopus embryo showed gastrulation and neural tube closure defects [60]. Due to the lack of a high-resolution structure, no atomic models of FAP20 or PACRG exist to date. Furthermore, the identity of other proteins in the lumen of the A- and B-tubules and at the inner junction, along with their localization and function are yet to be determined.

1.5 Figures

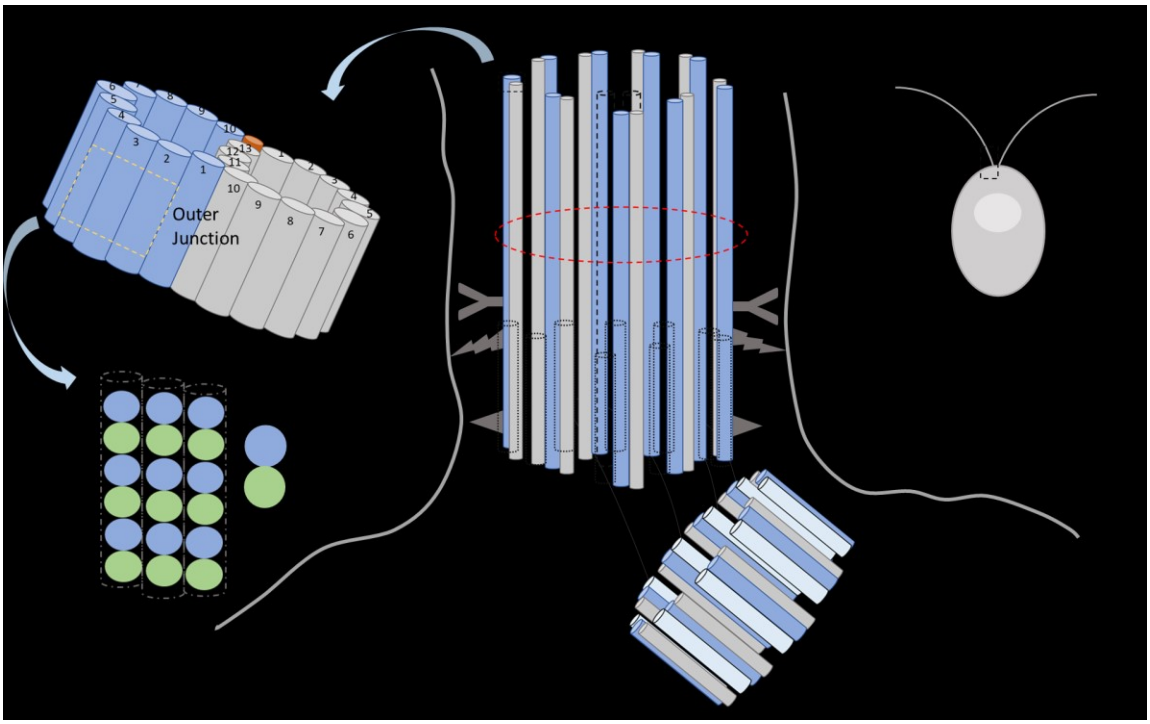

Figure 1.5.1 Schematic of the motile cilia showing the 9+2 arrangement of the doublet microtubules and the central pair.

A) A schematic of the biflagellate algal protist *Chlamydomonas reinhardtii*. B) The ciliary axoneme, which is composed of nine doublets, surrounding a central pair. C) The basal body of the cilia is a modified structure of the mother centriole where it has triplet microtubules that transition into doublets at the distal appendages (ii). The basal body remains connected to the daughter centriole (D) by a structure termed the rootlets (iv). The Distal appendages (ii), and other structures such as the Y shaped structures (i) and subdistal appendages (iii) act as a gateway to control trafficking between the ciliary compartment and the cellular compartment. E) A magnified doublet showing the A- and B-tubules of the doublet, their 10 and 13 PFs, respectively, and their outer and inner junctions. F) A schematic showing the longitudinal polymers of the α- and β-tubulin heterodimers, which makes up the PFs of the A- and B-tubules.

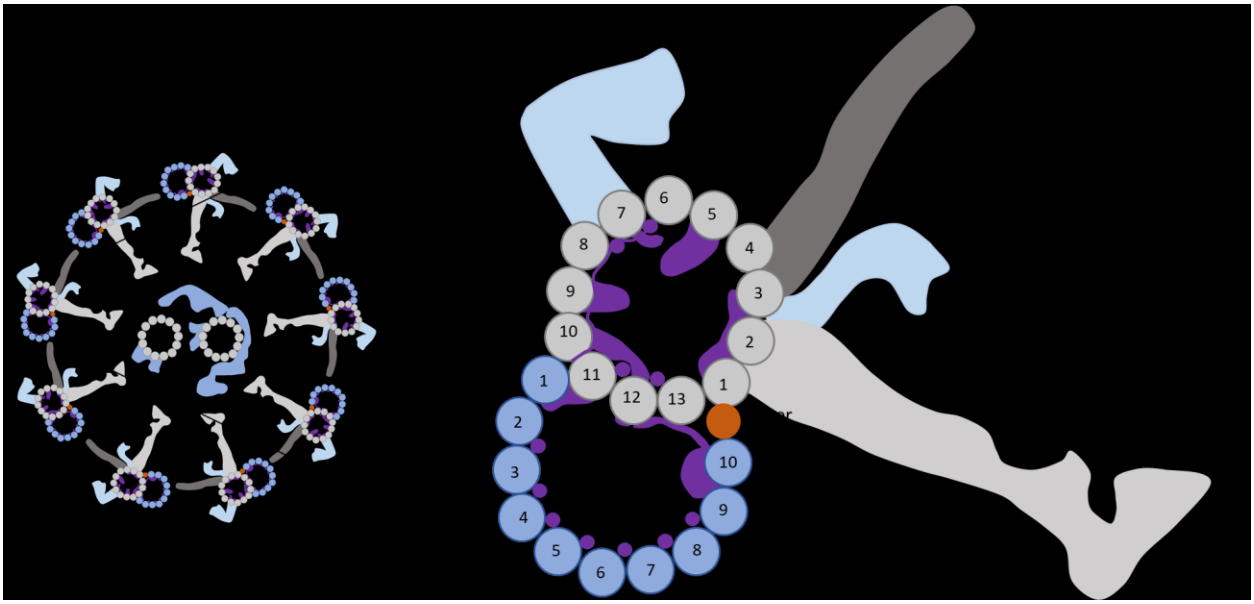

Figure 1.5.2 A cross section of the motile cilia and a magnified view of the doublet microtubule.

A) A cross section of the motile cilia axoneme (red circle in Figure 1.5.1B) showing the arrangement of nine doublet microtubules surrounding a central pair. The doublets are connected by the nexin-dynein regulatory complex which restricts their sliding resulting in bending. The radial spokes project towards the central pairs, which also regulate ciliary bending. The outer and inner arm dynein are the motors responsible for ciliary beating. The inner junction between the A- and B-tubules faces inwards (orange circle). B) The doublet is composed of a complete 13-PF A-tubule and a partial 10-PF B-tubule. There inner junction forms between A1 and B10, while the outer junction forms between B1, A10 and A11. There are many unknown electron densities (purple and dark blue) that associate with the doublet microtubules and the central pair. The schematic of the unknown densities was drawn from both [48] and [7] and reflects the combined densities from *Chlamydomonas* and *Tetrahymena* doublets.

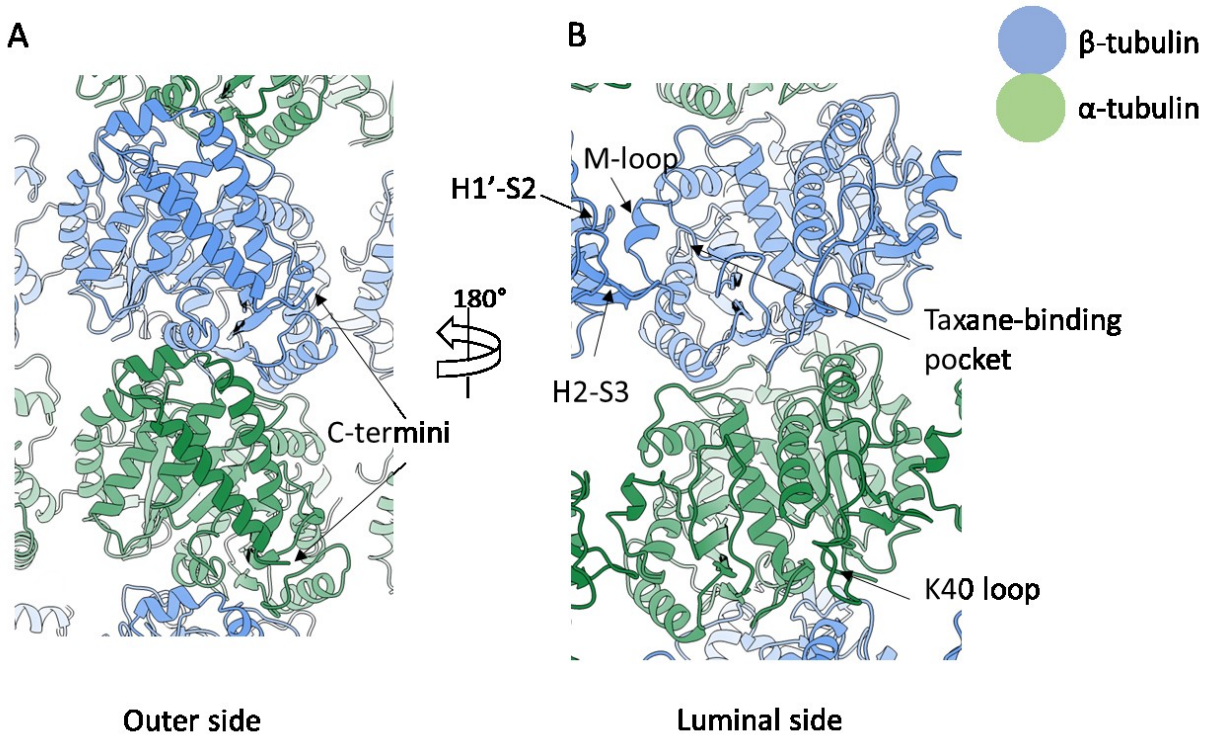

Figure 1.5.3 Atomic model of *Chlamydomonas* α-β-tubulin heterodimer.

A) View from the outside surface of the microtubule showing the C-termini of both α- and β-tubulins. The C-termini of both α- and β-tubulins are a hot spot for a variety of post translational modifications. B) The luminal side of the microtubule showing the taxane-binding pocket of β-tubulin, the loops involved in lateral interactions, which are the same for α-tubulin as well and the K40 loop of α-tubulin, which marks the sole site for luminal post-translational modifications.

Chapter 2: The inner junction complex of the cilia is an interaction hub that involves tubulin post-translational modifications

Ahmad Abdelzaher Zaki Khalifa[1,4§], Muneyoshi Ichikawa[1§†], Daniel Dai[1,4], Shintaroh Kubo[3,4], Corbin Black[1,4], Katya Peri[1], Thomas S. McAlear[1,4], Simon Veyron[2,4], Shun Kai Yang[1,4], Javier Vargas[1,4], Susanne Bechstedt[1,4], Jean-Francois Trempe[2,4], Khanh Huy Bui[1,4*]

[1]Department of Anatomy and Cell Biology, McGill University, Montréal, Québec, Canada, H3A 0C7

[2]Department of Pharmacology, McGill University, Montréal, Québec, Canada, H3A 0C7

[3]Department of Biophysics, Graduate School of Science, Kyoto University, Kyoto 606-8502, Japan

[4]Centre de Recherche en Biologie Structurale - FRQS, McGill University, Montreal, Quebec, Canada

[§] These researchers contributed equally to this work

[†]Present address: Department of Systems Biology, Graduate School of Biological Sciences, Nara Institute of Science and Technology, 8916-5, Takayama-cho, Ikoma, Nara 630-0192, Japan

[*] **Corresponding author. E-mail: huy.bui@mcgill.ca**

Short: Inner junction complex of the cilia

Keywords: microtubule, cilia, axoneme, cryo-electron microscopy, acetylation, inner junction

2.1 Preface

In this chapter, I reveal the complete identity of the *Chlamydomonas* inner junction proteins. I identified three previously unknown inner junction proteins: FAP276, FAP106 and FAP126. I modelled all such proteins as well as the previously identified proteins: FAP20, FAP52 and PACRG. I present a structure-based discussion of the role of each protein, potential mechanisms of doublet assembly and potential explanation of previously reported mutant phenotypes.

2.2 Abstract

Microtubules are cytoskeletal structures involved in stability, transport and organization in the cell. The building blocks, the α- and β-tubulin heterodimers, form protofilaments that associate laterally to form the hollow microtubule. Protofilaments can further form highly stable doublet microtubules in the cilia where stability is needed for ciliary beating and function. The doublet microtubule maintains its stability through interactions at its inner and outer junctions where its A- and B-tubules meet.

Here, using cryo-electron microscopy, bioinformatics and mass spectrometry, we identified two new inner junction proteins, FAP276 and FAP106, and an inner junction associated protein, FAP126, thus presenting the complete answer to the inner junction identity and localization. We show with atomic models that these proteins, together with PACRG, FAP20 and FAP52 form an interaction hub at the inner junction, where tubulin's post-translational modifications occur. We further compare the inner junction structure between two species: *Chlamydomonas* and *Tetrahymena.*

2.3 Introduction

Cilia and flagella are highly conserved organelles present in protists all the way to humans. They are commonly classified into two forms: motile and non-motile cilia. Motile cilia are responsible for mucus clearance in the airway, cerebrospinal fluid circulation and sperm motility [1]. The non-motile cilia, namely primary cilia, function as the cellular antennas that sense chemical and mechanical changes. Cilia are essential for growth and development and therefore human health. Defects in cilia often result in abnormal motility or stability, which lead to cilia-related diseases such as primary ciliary dyskinesia, retinal degeneration, hydrocephalus and polydactyly [2].

Both cilia types are comprised of a bundle of nine specialized microtubule structures termed doublet microtubules (doublets). Ciliary components, important for motility such as the outer and inner dynein arms, radial spokes and the dynein regulatory complex (DRC) are assembled onto the surface of the doublet [3-6]. Inside the doublets, is a weaving network of proteins, termed microtubule-inner-proteins (MIPs), that bind to the inner lumen surface of the doublet [7, 8]. These MIPs act to stabilize the microtubule and very likely regulate the ciliary waveform through interactions with the tubulin lattice [8].

Doublets consists of a complete 13-protofilament (PF) A-tubule, similar to a 13-PF cytoplasmic microtubule and a partial 10-PF B-tubule forming on top of the A-tubule. To this day there still exists a long-standing question of how the junctions between the two tubules are formed [9-11]. Recent high-resolution cryo-EM structure of the doublet shows that the outer junction is formed by a non-canonical tubulin interaction between PF B1 and PF A10 and A11 [7]. The inner junction (IJ), which bridges the inner gap between the B-tubule and A-tubule is formed by non-tubulin proteins. Both primary and motile cilia have been observed to contain the IJ [11, 12].

In vitro formation of a B-tubule-like hook (i.e. the outer junction like interaction) was assembled onto pre-existing axonemal and mitotic spindle microtubule with the addition of purified brain tubulin [13]. More recently, the B-tubule-like hook can be achieved by adding purified tubulins onto existing subtilisin treated microtubule [14]. However, these hooks are not closed and appear to be very flexible [14]. This supports the notion that the IJ is composed of non-tubulin proteins that are indispensable to the stability of the IJ.

The IJ is composed of FAP20 as shown through cryo-electron tomography and BCCP-tagging [15]. Dymek et al [16] reported that PArkin Co-Regulated Gene (PACRG) and FAP20 proteins form the IJ. PACRG and FAP20 are arranged in an alternating pattern to form the IJ linking the A- and B-tubule protofilaments A1 and B10 of the axonemal doublets. In addition, both FAP20 and PACRG are important components for motility. Both PACRG and FAP20 are conserved among organisms with cilia, suggesting a common IJ between species.

PACRG shares a bi-directional promoter with the Parkinson's disease-related gene parkin [17, 18]. Due to its axonemal functions, knockdown of PACRG genes in *Trypanosoma brucei* and *Xenopus*, lead to defects in the doublet structure and, therefore, impaired flagellar motility. In vertebrates, defects in left-right body symmetry, neural tube closure were observed from knockdowns of PACRG [19]. In mice, PACRG knockout results in male sterility [20] and hydrocephalus [21]. FAP20 knockout mutants in *Chlamydomonas* have motility defects and frequent splaying of the axoneme [15]. Similarly, FAP20 knockdown in *Paramecium* has an altered waveform [22]. A recent report identified other MIPs near the IJ, namely FAP52 and FAP45 [23]. Knockouts of FAP52 or FAP45 lead to an unstable B-tubule in *Chlamydomonas*. Double knockouts of FAP52 or FAP45 together with FAP20 leads to severe damage of the B-tubule. The gene deletion of the human homolog of FAP52 has been shown to cause heterotaxy and *situs inversus totalis* in patients [24].

Cryo-EM structures of isolated doublets from *Tetrahymena* show that there are different tethering densities that connect the B-tubule to the A-tubule aside from the IJ [7, 8]. However, the identity of such protein remains unknown to date. Taken together, these data suggest that there is a complex interaction at the IJ region involving multiple proteins in addition to PACRG, FAP20, FAP45 and FAP52. These interactions may play a role in regulating ciliary motility via stability.

Despite all the phenotypes known about these IJ proteins, there are no high-resolution structures to explain the molecular mechanism of the B-tubule closure and the IJ stability. In this study, we present the high-resolution cryo-EM structure of the IJ region from the *Chlamydomonas* doublet. Using a combination of bioinformatics and mass spectrometry, we were able to identify two new IJ proteins, FAP276 and FAP106, and a new IJ-associated MIP, FAP126. Our results suggest that the IJ is made up of a complex of proteins involving PACRG, FAP20, FAP52, FAP276, FAP106

and FAP126. We also compare the *Chlamydomonas* structure with the *Tetrahymena* structure to understand the common and species-specific features of the IJ.

2.4 Results

2.4.1 Multiple tether proteins exist at the IJ

To better understand the IJ, we obtained the 48-nm repeating unit of taxol stabilized and salt treated *Chlamydomonas* doublet at 4.5 Å resolution (Figure 2.8.1A-B and Figure 2.9.1A-C). Due to the salt wash, some MIPs were lost when compared to the intact tomographic doublet structure (dashed parts in Figure 2.8.1B) [5]. When comparing to the cryo-EM structure of the 48-nm repeating unit of *Tetrahymena* [7, 8], the IJ region bridging PF B10 and A1 remained intact (Figure 1A-D). Based on previous studies [15, 16, 23], we were able to localize FAP52, FAP45 in both *Tetrahymena* and *Chlamydomonas* (FAP52, light green and FAP45, yellow-green in Figure 2.8.1E, G), and PACRG and FAP20 (PACRG, light gray and FAP20, dark gray in Figure 2.8.1F) in *Chlamydomonas*.

In this study, we termed the structure formed by the repeating units of PACRG and FAP20, the IJ protofilament (IJ PF), and refer to the IJ complex as all the proteins involved in the attachment of the B-tubule to the A-tubule. Most of the proteins in this IJ complex are attached to PFs B8 to B10 and the IJ PF.

The presence of the IJ PF stabilizes the B-tubule of the *Chlamydomonas* doublet relative to *Tetrahymena*, as evidenced by local resolution measurements (Figure 2.9.1D). Despite having a good resolution in the A-tubule, the *Tetrahymena* doublet has a significantly lower resolution in the IJ area of the B-tubule.

Inside the B-tubule of both species, it is clear that the IJ region is held up by many tether densities along the doublet connecting the B-tubule to PF A13 (Figure 2.8.1E-G). First, the B-tubule is held up by tether density 1 (red, Figure 2.8.1H), referred to as MIP3b previously [7, 8]. Tether density 1 connects the PF B9/B10 and A13. The second connection is named Tether density 2 (red, Figure 2.8.1E-G), projecting from the proximal lobe of the FAP52 density (referred to as MIP3a previously [7]) and connecting to PF A13 (Figure 2.8.1H). In *Chlamydomonas*, there is another Y-shaped density (purple) cradling the FAP52 proximal lobe density and projects into the gap between the IJ PF and PF B10 (Figure 2.8.1H).

FAP45, which is referred to as MIP3c previously [23] is a filamentous MIP binding at the inner ridge between PF B7 and B8. In both species, FAP45 forms an L-shape density which contacts FAP52 once every 48-nm. This explains the zero-length cross-link observed in a recent study [23]. In *Tetrahymena*, there exists a tether density 3 (pale violet, Figure 2.8.1), projecting from the distal lobe of the FAP52 density and connecting to PF A13. This Tether density 3 is not present in the *Chlamydomonas* doublet, suggesting that this density is specific to *Tetrahymena*. All the tether densities described above repeat with 16-nm.

The IJ PF is formed by a heterodimer of PACRG and FAP20 repeating every 8-nm with the same repeating unit as tubulin dimers (Figure 2.8.1F). This is to be expected as the purpose of the IJ PF is to bridge the tubulin dimers from PFs B10 and A1. In the 48-nm *Chlamydomonas* doublet map, however, is one PACRG unit with a less defined density compared to the others (dashed box, Figure 2.8.1F). It has been shown that there is one PACRG density missing in every 96-nm repeat [6, 16]. Since our doublet map is a 48-nm repeat unit, the less defined density of PACRG corresponds to the average from one unit of PACRG and one missing unit, i.e. half the signal. This missing unit of PACRG in the 96-nm repeat allows the basal region of the DRC to anchor onto the doublet [6] (Figure 2.9.1F, G).

The entire IJ filament of PACRG and FAP20 seems to be missing in the *Tetrahymena* structure. Upon adjusting the threshold value of the surface rendering, we observed one dimer of PACRG and FAP20 remaining in the structure, previously named the IJ small structure (Figure 2.9.1E) [7]. This can be a result of a specific region every 96-nm of the *Tetrahymena* doublet that can hold this dimer in place preventing its detachment during sample preparation.

2.4.2 PACRG, FAP20, FAP52 and FAP276 form an IJ complex

Since the majority of IJ proteins repeat with 8-nm and 16-nm, we obtained first the 16-nm repeating unit from *Chlamydomonas* and *Tetrahymena* at 3.9 Å resolution (Figure 2.8.2A-B and Figure 2.9.1C). Using focused refined, the IJ complex of *Chlamydomonas* was improved to 3.6 Å resolution. Without the IJ PF, the B-tubule is flexible in *Tetrahymena*, which leads to significantly lower resolution in the IJ area as shown by local resolution measurement (Figure 2.9.1D). In contrast, the IJ region of *Chlamydomonas* has good resolution due to the stability of the B-tubule

as a result of the intact IJ PF. It is worth mentioning that PFs A3-A6 in *Chlamydomonas* have lower resolution due to the lack of MIPs in this region. At 3.6 Å resolution, we were able to segment, trace and *de novo* model PACRG, FAP20 and FAP52 in *Chlamydomonas* (Figure 2.8.2A, B and Figure 2.9.2A-F). We could not model FAP45 since FAP45 repeats with 48-nm, and therefore is averaged out in the 16-nm averaged map.

We were able to trace and, therefore, estimate the molecular weight of the Y-shaped density to ~10 kDa. Since this density is repeating with 16-nm and has a large binding interface with FAP52, we hypothesized that this protein would be missing in FAP52 knockout cells. Therefore, we did mass spectrometry of split doublets isolated from *Chlamydomonas* FAP52 knockout cells and performed relative quantification of axonemal proteins compared to the wild type [25]. We observed 12 missing and 26 proteins reduced by at least 2-fold (Table 1 and Supplementary Table 1). PACRG, FAP20 and FAP45 levels are unchanged in FAP52 mutants since their binding interfaces with FAP52 are not as large as supported by our structure. The level of tektin, another suggested IJ protein, did not change as well.

Among the proteins missing in the FAP52 knockout flagella, FAP276 fits our search criteria in terms of molecular weight (Table 1). The secondary structure prediction of FAP276 and the side chains agree unambiguously with the density signature in this region (Figure 2.9.2G, H). This leaves no doubt that the Y-shaped density is indeed FAP276. Thus, the IJ complex is made up of two copies of PACRG and FAP20, one copy of FAP52 and FAP276 and one copy of Tether density 1 and 2 per 16-nm (Figure 2.8.2C). This represents a high stoichiometry compared to other proteins in the axoneme such as CCDC39 and CCDC40, which have only one copy per 96-nm [26].

The PACRG structure is composed mainly of α-helices with a long unstructured N-terminal region. PACRG contains an alpha solenoid architecture, similar to the microtubule binding TOG domain, which is present in many microtubule polymerases [27, 28]. On the other hand, FAP20 has a beta jelly roll architecture, which consists of mainly β-sheets with a small α-helix. The C-terminus of FAP20 is located at the outside of the doublet, in agreement with a tomographic study of FAP20 with a Biotin Carboxyl Carrier Protein tag at the C-terminus. [15].

PACRG and FAP20 have two microtubule-binding sites, one on the surface of the A-tubule similar to well-studied microtubule-associated protein binding sites such as TOG [28], and one on the lateral side of the B-tubule (Figure 2.8.2D). The lateral binding site is unique and has never been observed in previously known microtubule-associated proteins. PACRG binds to the inter-dimer interface of PF B10 in the region of MEIG1 binding loop [29] and β-tubulin from PF A1. The interaction with PF B10 involves residues Y125, R137, S139 and R265 with E88 and E111 from β-tubulin and D160 and D127 from α-tubulin (Figure 2.8.2E). FAP20 is sandwiched by the tubulin dimer from PF B10 and the α-tubulin from PF A1 (Figure 2.8.2D).

The interactions of PACRG and FAP20 with tubulin from PF A1 appear to be electrostatic. The outside surfaces of α- and β-tubulins are highly negatively charged while the corresponding interacting surfaces of PACRG and FAP20 are positively charged (Figure 2.8.2F). Despite the fact that PACRG contains alpha solenoid architecture like TOG domains, the binding orientation of PACRG to the surface of tubulin is different from TOG domain binding [28].

In addition to the interactions highlighted above, we also observed the interaction of the β-tubulin C-terminus from PF A1 with PACRG (Figure 2.8.2G, H). The C-termini of α- and β-tubulins are a hot spot for post-translational modifications such as polyglutamylation and polyglycylation [30]. However, due to its flexibility, densities for the α- and β-tubulin C-termini are usually not visible in microtubule cryo-EM reconstructions. This is also the case for the outside of the A- and B-tubules in our *ex vivo* structure. However, in the lumen of the B-tubule, the β-tubulin C-terminus from PF A1 appears to be stabilized by two key interactions with PACRG: the hydrogen bond between D432 together with the hydrophobic burial and the stable T-shaped stacking of F436 with N251 and Y249 of PACRG, respectively (Figure 2.8.2H). Both interactions stabilize the β-tubulin C-terminus forming a helical turn in segment E432-E437, which otherwise wouldn't be present due to its flexibility.

This structuring of the β-tubulin C-terminus in PF A1 appears to be the result of the steric proximity with the N-terminus of PACRG. Thus, both interactions are important in maintaining the stability of the IJ by preventing steric clashing between the two. It could also be an indication of further post-translational modifications that occur in this region, which could have a potential role in IJ formation and stability.

In our structure, we also observe that the distance between FAP20 and the proximal PACRG is closer compared to the distal PACRG, thus PACRG and FAP20 likely form a heterodimer instead of a continuous protofilament (Figure 2.8.3A). The PACRG and FAP20 binding interface appears to involve multiple hydrogen bonds with complementary surface charges, suggesting a specific and strong interaction (Figure 2.8.3B, C). This FAP20 binding loop of PACRG is well-conserved among species (Figure 2.8.3D), but is not present in the PACRG-like protein, a homolog of PACRG and exists in the basal body [29]. FAP20, on the other hand, has a high degree of sequence conservation (Figure 2.9.3).

The cryo-EM structure of the *Chlamydomonas* PACRG is highly similar to the crystal structure of the human PACRG binding to MEIG1 (PDB: 6NDU) [29], suggesting a conserved role of PACRG. *Chlamydomonas* PACRG has a long N-terminus that binds on top of PF A13 and into the wedge between PF A1 and A13 (Figure 2.8.2I, Figure 2.9.2A). This N-terminal region is not conserved in humans or *Tetrahymena* [29]. This could indicate organism-specific adaptations to achieve finely tuned degrees of ciliary stability.

2.4.3 FAP52 forms an interaction hub and stabilizes α-tubulin's acetylated K40 loop

Next, we investigated the structure of FAP52 (Figure 2.9.2C). FAP52 consists of eight WD40 domains forming two seven-bladed beta-propellers. The two beta-propellers form a V-shape that docks onto PF B10 and B9. The proximal beta-propeller docks onto the inside of the α- and β-tubulin intra-dimer interface, while the distal beta-propeller is aligned with the next inter-dimer interface towards the plus end (Figure 2.8.4A).

The distal beta-propeller of FAP52 has a 3-point contact with the inner surface of the B-tubule (Figure 2.8.4B, C). Two of the FAP52 contacts involve the K40 loop of α-tubulin from PF B9 and B10. The α-K40 acetylation was first discovered in *Chlamydomonas* flagella, which is almost fully acetylated [31]. This α-K40 loop has not been fully visualized in reconstituted studies of acetylated tubulins. In our structure, the α-K40 loop is fully structured in this position (Figure 2.8.4D, E and Figure 2.9.4D-G). For the first contact point, residue R225 of FAP52 seems to interact with D39 of α-tubulin from PF B10 (Figure 2.8.4F, G). At the second tubulin contact point, FAP52 segment G142-P143 appears to interact with T41 of α-tubulin from PF B9. In the lower region of FAP52, residue N275 from the distal beta-propeller's V268-L279 loop interacts with segment P25-A27 of the N-terminus of PACRG (Figure 2.8.4G). The density of the aforementioned loop is not present

in the FAP52 structure in *Tetrahymena* doublet (Figure 2.9.4A, B). This long loop (V268 to L279) of *Chlamydomonas* FAP52 is, in fact, deleted in other species (Figure 2.9.4C). The interaction of this loop with *Chlamydomonas* PACRG suggests that it is a *Chlamydomonas* specific feature that stabilizes PACRG and, hence the IJ PF.

We then investigated the α-K40 loops from *Chlamydomonas* and *Tetrahymena* doublets (Figure 2.9.4D-G). When there is no interacting protein, this loop is flexible consistent with previous literature [32]. Despite having low resolution in the B-tubule in *Tetrahymena*, we still observed the α-K40 loop of PF B9 and B10 interacts with FAP52 (Figure 2.9.4B). We were also able to visualize the loop in several places in both *Chlamydomonas* and *Tetrahymena* where there is an interacting protein (Figure 2.9.4F, G). The conformation of the loop appeared to be different depending on its interacting protein. This suggests that the α-K40 loop could have a role in MIP recognition and binding.

Furthermore, because of the V-shape of FAP52, its interacting interface with tubulin is small. The existence of a cradling protein such as FAP276 then is logical from a functional standpoint since it appears to support and mediate the interaction between FAP52 and tubulin (Figure 2.8.4H). Segment L52-H57 from FAP276 forms beta sheet-like stacking interactions with segment L375-V380 from FAP52 (Figure 2.8.4H, I). FAP276 itself forms numerous interactions with tubulin with both of its N- and C-termini, thus it provides strong anchorage for FAP52 to the tubulin lattice (Figure 2.8.4H-K). Given the numerous interactions of FAP52 with all the proteins mentioned, FAP52 is likely to function as an interaction hub, which could play an important role during IJ assembly.

2.4.4 FAP106 is the Tether loop, consisting of Tether density 1 and 2

We were able to trace the Tether density in the 16-nm averaged map. Tether density 1 is connected to Tether density 2 (Figure 2.8.5A-D), forming a Tether loop, through which the A- and B-tubules are connected. The loop connecting the Tether density 1 binds on top of PF A12 and then into the outside wedge between A12 and A13 before connecting with Tether density 2. Therefore, the entire Tether loop is a single polypeptide, conserved between *Tetrahymena* and *Chlamydomona*s (Figure 2.8.5A-B). Part of this Tether loop resembles Tau binding to the microtubule [33]. There is a small helical region in this loop that binds to α-tubulin of PF A12 (Figure 2.9.5A, B).

To identify the protein that makes up the Tether loop, the protein needs to satisfy the following criteria: (i) has a high stoichiometry (1 per 16-nm of the doublet); (ii) has a minimum molecular weight of ~25kD (based on a poly-Alanine trace) and (iii) conserved in both *Chlamydomonas* and *Tetrahymena*.

We calculated the stoichiometry of proteins in the doublet after salt extraction by normalizing the averaged quantitative spectral count of each protein by their molecular weight. The triplicate mass spectrometry data comes from Dai et al. [25]. The top 35 proteins by copy numbers are shown in Table 2. In our calculation, some radial spoke and central pair proteins displayed high stoichiometry such as RSP9 and PF16. Remarkably, all the IJ proteins are in the top 35 (PACRG, FAP52, FAP20, FAP45 ranked 4, 9, 10 and 35 respectively) as supported by our structure. This validates the quality of the stoichiometry calculation. Although FAP276 should have the same stoichiometry as FAP52, it does not appear in high stochiometric numbers. This can be explained that by the small size of FAP276, which is not well detected in mass spectrometry.

Among the proteins that have high stoichiometry, the following proteins satisfy the three criteria above: FAP115, FAP106, FAP252, FAP161, FAP77 and FAP71. However, the homologs of FAP115 and FAP161 in *Tetrahymena* are too big. Our analysis of the secondary structure prediction places FAP106 at the top of the list of candidates for the Tether loop (Figure 2.9.5D). Furthermore, the sequence agrees with the density signature unambiguously, which leaves no doubt that the Tether loop is FAP106. This allowed us to model segments P20-A148 and W189-I226 where the density had sufficient signal (Figure 2.8.5C, D). Segments M1-R19 and R227-D240 have low SNR and are likely to be highly flexible. Helix H3 and H4 of FAP106 insert into the interdimer interfaces between PF B9 and B10 forming the anchor point to the B-tubule (Figure 2.8.5E) while helix H1 and H2 bind to β-tubulin of PF A13 and α-tubulin of PF A12 (Figure 2.8.5D). FAP106 is a homolog of ENKURIN (ENKUR), a conserved protein in sperms of many species [34, 35]. Enkur knockout mice have abnormal sperm motility with asymmetric flagellar waveform and therefore low fertility rate [35]. In addition, mutations in ENKUR is linked to situs inversus in human and mouse [36, 37]. However, the IQ motif of Enkurin that binds Calmodulin is not conserved in *Chlamydomonas* (Figure 2.9.4C).

In *Tetrahymena*, the Tether density 3 connects the distal lobe of FAP52 and binds across the wedge between PF A13 and A1. (Figure 2.8.5F). Upon superimposing the *Chlamydomonas* PACRG structure onto the *Tetrahymena* IJ area, the N-terminus of PACRG will have a steric clash with Tether density 3 (Figure 2.8.5G). This explains the shorter N-terminus of *Tetrahymena* PACRG relative to the *Chlamydomonas* PACRG. Tether density 3 might interact with and perform the same function as the N-terminus of PACRG in *Chlamydomonas*, which induces high curvature of PF A13 and A1.

2.4.5 FAP126, a FLTOP homolog, interacts with the tether loop, FAP106

We also were able to trace a density that lies on top of PF A13 and goes into the wedge between PF A12 and A13 (Figure 2.8.6A, turquoise). This density was described previously as part of MIP5 [7], and is mostly disordered. It is not present in the *Tetrahymena* map and was traced as a single polypeptide.

The density in this region had multiple clear side chains that could be identified, and so we applied two search strategies to identify this protein. We used a local search against the entire proteome of *Chlamydomonas* using a regular expression that matches a pattern of WxPxxxxW which was observed in the density. This resulted in one unique hit, which is FAP126. We then applied the same strategy to search for this protein as FAP106. The criteria were: (i) a high stoichiometry number; (ii) a size of ~15 kDa and (iii) no homolog in *Tetrahymena*. In this case, the only protein that satisfied these criteria among high stoichiometry proteins (Table 2) was also FAP126. Furthermore, the remainder of the FAP126 sequence agrees unambiguously with the density signature in this region (Figure 2.8.6B and Figure 2.9.6B).

FAP126 is a homolog of the human FLTOP protein, which is shown to be important for basal body docking and positioning in mono- and multi-ciliated cells [38]. Multiple alignment sequence alignment of FAP126 shows that the *Chlamydomonas* FAP126 lacks the proline-rich regions of other species (Figure 2.9.6A).

FAP126 appears to interact with FAP106 (Figure 2.8.6B). Segment F75-Q77 of FAP126 is in proximity to segment T128-K130 of FAP106. Q77 and Q129 of FAP126 and FAP106, respectively, are within favorable distance and orientation to form a hydrogen bond with one another (Figure 2.8.6B). Therefore, FAP126 might play a role in recruiting FAP106 or vice versa.

Almost half of FAP126 density runs along the wedge between PF A12 and A13, close to the tubulin lateral interface with complementary surface charge (Figure 2.8.6C, D). FAP126 might act as a low curvature inducer from the outside similar to Rib43a from the inside since the curvature of A12 and A13 is significantly lower compared to 13-PF singlet (Figure 2.8.6E, F) [8].

To support whether FAP126 interacts with FAP106, we analysed the normalized RNA expression of FAP126 with FAP106 (ENKUR) and FAP52 from different human tissues (Figure 2.8.6G, H and Figure 2.9.5C). FAP126 showed high correlation with both FAP106 (ENKUR) and FAP52(r=0.89, p-value =<0.0001, r=0.94, p-value=<0.0001, respectively). This indicates that FAP126 might be functionally related to other members of the IJ such as FAP106 and FAP52, which further supports the identity of these proteins.

2.5 Discussion

In this study, we describe the complete molecular details of the IJ complex using a combination of mass spectrometry and cryo-EM. The IJ complex in *Chlamydomonas* is made up of PACRG, FAP20, FAP52, FAP276, FAP106 (Tether loop) and associated proteins such as FAP126 and FAP45 (Figure 2.8.7A). We identified two new members of the IJ, FAP106 and FAP276. FAP276, a *Chlamydomonas* specific protein, anchors and mediates FAP52's binding onto tubulins from PF B9 and B10. FAP106 tethers the B-tubule to the A-tubule, through its interactions with the PF A12 and A13, FAP52 and FAP276, while the IJ PF, composed of PACRG and FAP20, closes the IJ gap. For the doublet to withstand the mechanical strain during ciliary beating, it needs all its unique structural features and interactions for proper stability. Tektin, a coiled-coil protein, was also proposed to be another component of the IJ complex in *Chlamydomonas* by biochemical experiments [15]. However, no filamentous density corresponding to tektin was found at the IJ PF in our *Chlamydomonas* map.

Reconstituted doublet microtubules [14] indicate that the B-tubule cannot be closed and is extremely flexible without the IJ PF. Therefore, the IJ PF is necessary to dock the B-tubule onto the A-tubule. In our *Tetrahymena* doublet, in which the IJ PF was washed away, even with the presence of FAP52 and FAP106, the doublet is still flexible which can be seen by the lower resolution of the B-tubule compared to the A-tubule (Figure 2.9.1D). In addition, the B-tubule can be subjected to depolymerization when the IJ PF is not fully formed [23]. Therefore, the IJ PF serves as an anchor, which protects the B-tubule from depolymerization by shielding the lateral

side of PF B10 (Figure 2.8.7B). Because of the complexity of interactions and the diverse protein composition of the IJ complex, it is reasonable to assume that the IJ is assembled after the outer junction nucleates and expands towards the IJ. The IJ complex might be assembled or co-assembled at the same time as PF B10 for the closure of the B-tubule (Figure 2.8.7B).

During doublet assembly, the unorderly binding of PACRG and FAP20 to any of the PFs in the B-tubule lateral interfaces would lead to an incomplete B-tubule [29]. To facilitate a successful IJ assembly, chaperones might be needed for the transport of PACRG and FAP20. PACRG forms a complex with MEIG1 [29]. Even though MEIG1 is not present in lower eukaryotes and that the MEIG1 binding loop is not conserved between *Chlamydomonas* and humans, a chaperone similar to MEIG1 can function to target PACRG to the lateral interface of the PF B10. Our atomic models support that PACRG and FAP20 might form a heterodimer before their transport and assembly into the cilia (Figure 2.8.3A). Surprisingly, FAP20 shows a similar fold and mode of binding to a class of proteins called carbohydrate-binding modules. Carbohydrate binding modules form a complex with carbohydrate-active enzymes and are known to have a substrate targeting and enzyme-concentrating function [39]. This supports the role of FAP20 as an assembly chaperone in a FAP20-PACRG complex. Furthermore, both studies from Yanagisawa et al. [15] and Dymek et al. [16] show reduced endogenous PACRG in *Chlamydomonas* FAP20 knockout mutant. In the latter study, it was shown that the assembly of exogenous PACRG was less efficient in the FAP20 knockout compared to conditions where FAP20 was intact. This implies that PACRG assembly might indeed depend on FAP20 [15]. However, since the expression patterns of PACRG and FAP20 have surprisingly low correlation compared to the rest of the IJ proteins (Figure 2.9.5E), it suggests that FAP20 might have an additional function outside the IJ of the cilia.

Furthermore, our atomic models could explain the severe motility phenotypes observed in PACRG and FAP20 mutants compared to FAP52 mutant. Mutants in either PACRG or FAP20 might affect the stability of the DRC, which can severely affect the regulation of ciliary beating. This is supported by the fact that FAP20 mutant is prone to splaying of the cilia [15]. Our results could also explain how the double knockout of FAP20 along with FAP45 or FAP52 can affect B-tubule stability at the IJ [23]. In such conditions, both the IJ PF and the FAP52 or FAP52-mediated anchorage between the A- and B-tubules will be completely lost.

By comparing *Chlamydomonas* and *Tetrahymena*, we show that the conserved IJ components are PACRG, FAP20, FAP45, FAP52 and FAP106. There are also species-specific proteins such as FAP276 and FAP126 in *Chlamydomonas* and the Tether density 3 in *Tetrahymena*. The Tether density 3 clashes with a superimposed *Chlamydomonas* FAP276 structure, suggesting that it takes over its role in mediating the interactions between FAP52 and tubulin in *Tetrahymena*. This suggests that there is a common framework for the IJ complex in all species. Species-specific proteins may then fine-tune this framework according to the organism's survival needs.

In this study, we revealed that FAP106/ENKUR, an important protein for sperm motility, is a MIP and an IJ protein. Knockout of ENKUR leads to the asymmetric waveform of sperm flagella while mutations in ENKUR disturb the left-right symmetry axes in vertebrates. It is shown that knockout ENKUR shows a loss of Ca^{++} responsiveness while wild type sperm shows highly curved flagella [35]. The IQ domain responsible for Ca^{++} binding of ENKUR is not conserved in the *Chlamydomonas* sequence, although an alternative means of Ca^{++} binding or inducing a Ca^{++} mediated response is still possible.

In this study, we also identified FAP126, an IJ-associated MIP. The homolog of FAP126 in human and mouse, the FLTOP protein, exists in the cilia and basal bodies and is thought to function in the positioning of the basal body [38]. In Flattop knockout mice, cilia formation in the lung is significantly affected. In the inner ear, Flattop interacts with a protein called Dlg3 in the process of basal body positioning to the actin skeleton in the inner ear. Therefore, it is possible that FAP126 might perform both functions (i) as a MIP that stabilizes the basal body in the same fashion as shown here for the cilia and (ii) in basal body positioning and planar cell polarity [38]. The high correlation of FAP126 and FAP106 co-expression, and also with FAP52 in different human tissue suggests they might function similarly or co-operatively in cilia assembly. *Tetrahymena*, which lacks FAP126, probably implements an alternative mechanism to substitute for FAP126 functions.

Our study demonstrates that all the protein components associated with the IJ complex such as PACRG, FAP20, FAP52, FAP126 and FAP106 in the IJ complex is of high importance for the assembly and proper motility of the cilia. Multiple studies have indeed showed the implication of such proteins in human disease [20, 24, 37]. Remarkably, these proteins are MIPs existing inside the doublet except for PACRG and FAP20. This revelation supports the notion that MIPs can directly influence the tubulin lattice and hence the motility of the cilia [8]. In the regions, where

MIPs are not present due to preparation, the local resolution is significantly worse than the global resolution (Figure 2.9.1D). In addition, the structures of the IJ components such as PACRG and FAP126 also highlight the unique roles of the MIPs in curvature inducing or sensing as shown previously with Rib43a [8]. FAP126 binds tightly to the wedge PF A12 and A13 while the N-terminus of *Chlamydomonas* PACRG penetrates the wedge between PF A13 and A1 and forces the PF pairs into a high-curvature conformation (Figure 2.8.6E). From our curvature analysis of the doublet (Figure 2.8.6F), this region of PF A12-A1 contains extreme high and low curvatures compared to the 13-PF singlet. Alternatively, the curvature might be enforced by MIPs inside the A-tubule. This inter-PF curvature could help to facilitate the specific binding and anchoring of FAP126 and PACRG to the right position. It has been shown that doublecortin can sense the curvature of the 13-PF microtubule [40]. In *Tetrahymena*, Tether density 3, which is not present in *Chlamydomonas* seems to be a high curvature inducer/sensor and an IJ complex stabilizer.

Post-translational modifications in tubulin are known to be important for the activity of the cilia. There have been many studies about the effect of acetylation on the properties of microtubule such as stability [41, 42]. In 3T3 cells, the K40 acetyltransferase, αTAT1 promotes rapid ciliogenesis [43]. The absence of acetylating enzymes has indeed been shown to affect sperm motility in mice [44] while SIRT2 deacetylation decreases axonemal motility in vitro [45]. A recent cryo-EM study of reconstituted acetylated microtubules showed, using molecular dynamics, that the acetylated α-K40 loop has less conformational flexibility, but a full α-K40 loop in the cryo-EM map has not been visualized due to its flexibility. In this work, we show that the acetylated K40 loop binds to FAP52 and forms a fully structured loop. This loop remains flexible and unstructured when there is no interacting protein. This suggests that the α-K40 loop has a role in protein recruitment and interactions, especially, MIPs. We hypothesize that the acetylation disrupts the formation of an intra-molecular salt bridge between K40 and D39, which affects the loop's sampling conformations and allows D39 to take part in atomic interactions with other proteins. This, in turn, improves the stability of the doublet and therefore, correlates with axonemal motility. In neurons, microtubules are also highly acetylated and are known to be stable. Our hypothesis suggests that in neuron microtubules, there might exist MIPs with a similar stabilizing effect as in the doublet. Previous studies on olfactory neurons demonstrate that there are densities of proteins inside the microtubule, suggesting the existence of MIPs inside cytoplasmic microtubules [46].

Another interesting insight from our study is the structured C-terminus of β-tubulin. The C-termini of tubulin in the doublet normally have polyglycylation and polyglutamylation, in particular, the B-tubule [47]. In reconstituted microtubules and other places in the doublet, the C-termini are highly flexible and cannot be visualized. However, we observed the C-terminus of β-tubulin in PF A1 which appears to interact with PACRG and FAP20. In addition, the position of FAP126 and FAP106 binding on top of tubulin molecules also suggest they are interacting with the C-termini of tubulins. In vitro study shows that the C-tails of tubulins must be suppressed for the outer junction to be formed [14]. This suggests that the C-terminus might have a role in the assembly and or stability of the doublet. Defects in tubulin polyglutamylase enzyme have indeed led to partially formed B-tubules [48]. This could indicate a role for polyglutamylation in the interaction and recruitment at the IJ PF, specifically PACRG and FAP20. Lack of polyglutamylation can lead to an easily detachable PACRG and FAP20 and hence the partial assembly of the B-tubule. Finally, it is possible that MIPs can act as readers of tubulin post-translational modifications for their orderly recruitment and assembly.

2.6 Materials and methods

Preparation of doublet samples

WT *Chlamydomonas* cells (cc124) were obtained from *Chlamydomonas* source center and cultured either on Tris-acetatephosphate (TAP) media with shaking or stirring with 12 hr light-12 hr dark cycle. For flagella purification, *Chlamydomonas* cells were cultured in 1.5 L of liquid TAP media with stirring until OD600 reached around 0.5-0.6 and harvested by low-speed centrifugation (700g for 7 min at 4℃). *Chlamydomonas* flagella were purified by dibucaine method [49], resuspended in HMDEKP buffer (30 mM HEPES, pH 7.4, 5 mM MgSO4, 1 mM DTT, 0.5 mMc, 25 mM Potassium Acetate, 0.5% polyethylene glycol, MW 20,000) containing 10 μM paclitaxel, 1 mM PMSF, 10 μg/ml aprotinin and 5 μg/ml leupeptin. Paclitaxel was added to the buffer since *Chlamydomonas* doublets were more vulnerable to high salt extraction compared with *Tetrahymena* doublets (data not shown). Isolated flagella were demembraned by incubating with HMDEKP buffer containing final 1.5% NP40 for 30 min on ice. After NP40 treatment, *Chlamydomonas* doublets were incubated with final 1 mM ADP for 10 min at room temperature to activate dynein and then incubated with 0.1 mM ATP for 10 min at room temperature to induce doublet sliding. Since the *Chlamydomonas* doublets were harder to split compared to *Tetrahymena* doublet, sonication was done before ADP/ATP treatment. After this, *Chlamydomonas* doublets were incubated twice with HMDEKP buffer containing 0.6 M NaCl for 30 min on ice, spinned down (16,000 g and 10 minutes), and resuspended. *Chlamydomonas* doublets were not dialyzed against low salt buffer since it was difficult to remove radial spokes.

Tetrahymena doublets were isolated according to our previous work [7, 8].

Cryo-electron microscopy

3.5 ul of sample of doublets (~4 mg/ml) was applied to a glow-discharged holey carbon grid (Quantifoil R2/2), blotted and plunged into liquid ethane using Vitrobot Mark IV (Thermo Fisher Scientific) at 25℃ and 100% humidity with a blot force 3 or 4 and a blot time of 5 sec.

9,528 movies were obtained on a Titan Krios (Thermo Fisher Scientific) equipped with Falcon II camera at 59,000 nominal magnification. The pixel size was 1.375 Å/pixel. Dataset for *Tetrahymena* was described in Ichikawa et al. [8]. *Chlamydomonas* dataset was collected with a dose of 28-45 electron/Å2 with 7 frames. The defocus range was set to between -1.2 and -3.8 um.

The *Chlamydomonas* doublet structures were performed according to Ichikawa et al. [8]. In short, movies were motion corrected using MotionCor2 [50]. The contrast transfer function were estimated Gctf [51]. The doublets were picked using e2helixboxer [52].

270,713 and 122,997 particles were used for the reconstruction of 16-nm and 48-nm repeating unit of *Chlamydomonas*. 279,850 particles were used for the 16-nm reconstruction of *Tetrahymena*. The final Gold Standard FSC resolutions of the 16-nm and 48-nm reconstruction for *Chlamydomonas* after contrast transfer function refinement and polishing using 0.143 FSC criterion in Relion3 [53] are 4.5 and 3.8 Å, respectively. Using focus refinement of the IJ of the 16-nm reconstruction for *Chlamydomonas*, the resolution reaches 3.6 Å resolution. The resolution for the 16-nm reconstruction of *Tetrahymena* was 3.6 Å. Focus refinement of the IJ of *Tetrahymena* did not improve the resolution of the IJ due to the flexibility of this region. The maps were local sharpened [8]. Local resolution estimation was performed using MonoRes [54].

Modelling

***C. reinhardtii* α-β-tubulin**

A homology model of *C. reinhardtii* α-β-tubulin (Uniprot sequence α: P09204, β: P04690) was constructed in Modeller v9.19 [55] using PDB 5SYF as template. The model was refined using real-space refinement [56] and validated using comprehensive validation for cryo-EM in Phenix v1.16 [57].

PACRG and FAP20

A partial homology model of *C. reinhardtii* PACRG (B1B601) was constructed using the crystal structure of the human homolog (Q96M98-1) as template [58]. The model was completed by building segments N2-D148 and Y249-L270 de novo in density using Coot v0.8.9.1 [59]. The density for segment M89-K101 is missing, likely due to flexibility in this region. *C. reinhardtii* FAP20 (A8IU92) was completely built de novo in density. Both models were refined and validated as described for α-β-tubulin.

FAP52

The density was traced in Coot v0.8.9.1 [59] according to a double beta-propeller topology similar to PDB 2YMU, which agrees with the I-TASSER [60] tertiary structure prediction of FAP52

(Uniprot: A0A2K3D260). The bulky residues of FAP52 were used as anchors to maintain the correct registry in lower resolution areas. The model could be overfit in segment D341-P627 where the density signal is significantly lower, likely due to heterogeneity. The final model was refined and validated as described above.

FAP276

The density for FAP276 was segmented and traced to around 80 amino acids and ~9 kDa in mass. Candidates from the wild type mass spectrometry data were compared to the FAP52 knockout data and reduced to only FAP276, which was completely missing in the latter. The secondary structure prediction [61] as well as the sequence of FAP276 (Phytozome: Cre04.g216250) agree unambiguously with the density signature in that region. The model was traced, refined and validated as described above.

FAP106

The identity of the density was narrowed down to FAP106 as discussed in the results section. This was based on a trace of ~220-240 amino acids due to missing and likely flexible segments in the protein. The sequence secondary structure prediction of FAP106 had high confidence in four α-helices and a long disordered segment, which agrees with the density topology in this region. The identity of FAP106 was further confirmed by a local search against the *Chlamydomonas reinhardtii* proteome (Uniprot: UP000006906) using a regular expression pattern that matches the density signature around residue W127 ([FHY]xWxxKxx[FHY]). This returned two matches: FAP106 and A8I9A1 (a transcription factor). As before, the amino acid side chains of FAP106 had unambiguous agreement with the density throughout the entire sequence. Segments M1-R19, K149-K188 and R227-D240 could not be modeled due to poor density in this area. The model was built and refined as mentioned above.

FAP126

The density for FAP126, which is mostly disordered, was traced as before to 133 amino acids and ~15 kDa. The density had clear side chains signature, particularly in an area where it appeared to have a Trp residue followed by an unknown residue, then a Proline, four more amino acids and another Trp. Doing a local search against the entire *Chlamydomonas reinhardtii* proteome, in both C- and N-termini directions, using a regular expression matching the pattern above (WxPxxxxW), gives a single hit: FAP126. Furthermore, inspecting candidates in the wild type mass spectrometry

that has a similar abundance to IJ proteins after normalizing the quantitative peptide value by the molecular weight places FAP126 in the top list of candidates for this density. As before, the sequence has matching secondary structure prediction and unambiguous density signature agreement throughout the entire sequence. The model was modelled and refined as mentioned above.

Inter-PF angle (lateral curvature) measurement

The inter-PF angle between each PF pair are measured according to Ichikawa *et al*., [7].

Visualization

The maps and models were segmented, coloured and visualized using Chimera [62] and ChimeraX [63].

Mass spectrometry

Sample preparation and mass spectrometry of FAP52 mutant and relative quantification compared to wild type *Chlamydomonas* was done according to Dai et al., 2019. (25). The ratio between the averaged quantitative values from the mass spectrometry (n=3) and a proteins molecular weight was used to calculate their stoichiometry in the axoneme.

Transcriptomics analysis

Transcriptomics analysis of PACRG, FAP20, FAP52, FAP126, FAP106, FAP45 and DCX using consensus normalized expression levels for 55 tissue types and 7 blood cell types was done according to [29].

Data availability

Cryo-EM maps have been deposited in EM data bank (EMDB) with accession numbers of EMD-20855 (48-nm averaged *Chlamydomonas* doublet), EMD-20858 (16-nm averaged *Chlamydomonas* IJ region) and EMD-20856 (16-nm averaged *Tetrahymena* IJ region). The model of IJ of *Chlamydomonas* is available in Protein Data Bank (PDB) with an accession number of PDB: 6URD.

The mass spectrometry is deposited in DataDryad (doi:10.5061/dryad.d51c59zxt). Available privately at:

https://datadryad.org/stash/share/bkrXp5Ww0iQUis6ocuEya2ivHWQ_YiTFO-VLeIjkQcM

2.7 Acknowledgements

We acknowledge the Facility for Electron Microscopy Research of McGill University where our cryo-EM experiments were conducted, particularly, Drs. Kaustuv Basu and Kelly Sears. We are indebted to Dr. Masahide Kikkawa for sharing the FAP52 knockout *Chlamydomonas* strain. This research was financially supported by Natural Sciences and Engineering Research Council of Canada (RGPIN-2016-04954), Canada Institute of Health Research (CIHR PJT-156354) and the Canada Institute for Advanced Research Arzieli Global Scholars Program to K.H.B., M.I. and S.K. were supported by Japan Society for the Promotion of Science (JSPS) for JSPS Overseas Research Fellowships and JSPS Overseas Challenge Program for Young Researchers, respectively. A.A.Z.K. is supported by CIHR and the Al Ghurair Foundation for Education. We declare no competing financial interests.

2.8 Figures

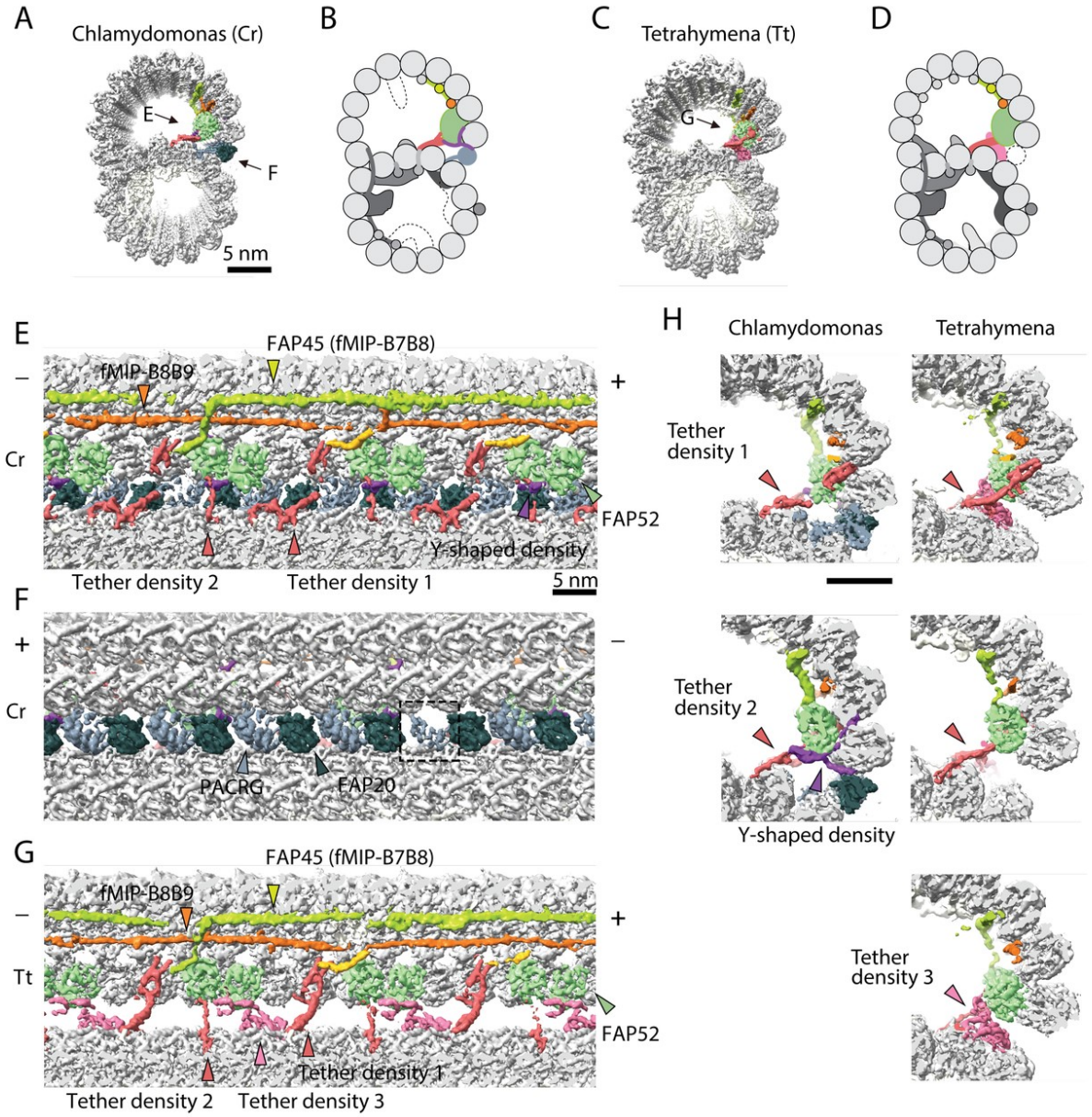

Figure 2.8.1 The IJ structures of *Chlamydomonas* and *Tetrahymena* doublet.

(A-D) Surface renderings and schematics of the 48-nm repeat cryo-EM maps of *Chlamydomonas* (A, B) and *Tetrahymena* (C, D) doublets viewed from the tip of the cilia. Black arrow indicates longitudinal view in (E), (F) and (G). (E-F) The longitudinal section of the *Chlamydomonas* doublet at the IJ complex from the inside (E) and outside (F). (G) The longitudinal section of *Tetrahymena* doublet viewed from the inside. Color scheme: FAP20: dark gray; PACRG: gray;

FAP52: light green, Y-shaped density: purple; FAP45: yellow green; fMIP-B8B9: orange; Tubulin: light gray; Rest of MIPs: white; Tether density 1 and 2: red; Tether density 3, pink. Plus and minus ends are indicated by + and - signs. (H) Cross sectional views of the different Tether densities from *Chlamydomonas* (left) and *Tetrahymena* (right). In *Chlamydomonas*, there is a Y-shaped density (purple) that cradles the FAP52 density. The Y-shaped density is absent in *Tetrahymena*. In *Tetrahymena*, we observed Tether density 3, which is absent in *Chlamydomonas*.

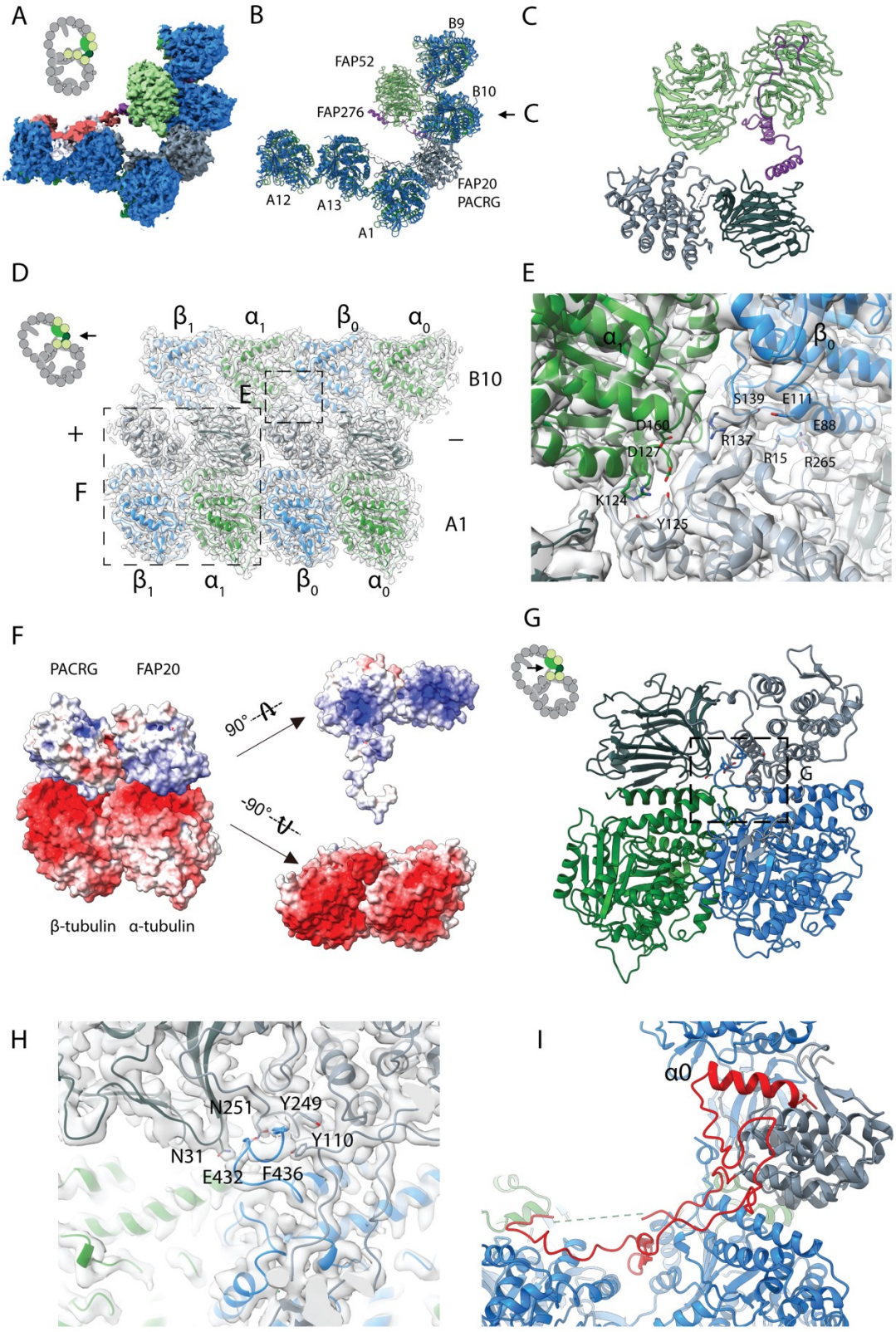

Figure 2.8.2 16-nm structure of *Chlamydomonas* doublet.

(A, B) 16-nm repeat structure of *Chlamydomonas* doublet and model at the IJ region. (C) Atomic model of the IJ complex, consisting of PACRG, FAP20, FAP52 and FAP276. (D) Maps and model of PF A1 and B10, and IJ PF. The view is indicated in the schematic. Dashed boxes indicate the views in (E) and (F). Color scheme: α-tubulin: green; β-tubulin: blue; PACRG: gray; FAP20: dark gray; FAP276: purple. (E) The iinteraction of PACRG with the inter-dimer interface of tubulins from PF B10 is shown. (F) Electrostatic surface charge of PACRG, FAP20 and α- and β-tubulins of PF A1. Tubulin surface is negatively charged while the interacting interface of PACRG and FAP20 are positively charged. (G) The C-terminus of β-tubulin of PF A1 interacts with PACRG and FAP20. (H) Potential residues involved in the interaction of C-tail of β-tubulin and PACRG and FAP20. (I) The N-terminus of PACRG going into the wedge between PF A13 and A1. The N-terminus of *Chlamydomonas* PACRG (red color) forms a stable triple helix arrangement with the core of the protein. This is not observed in the human PACRG.

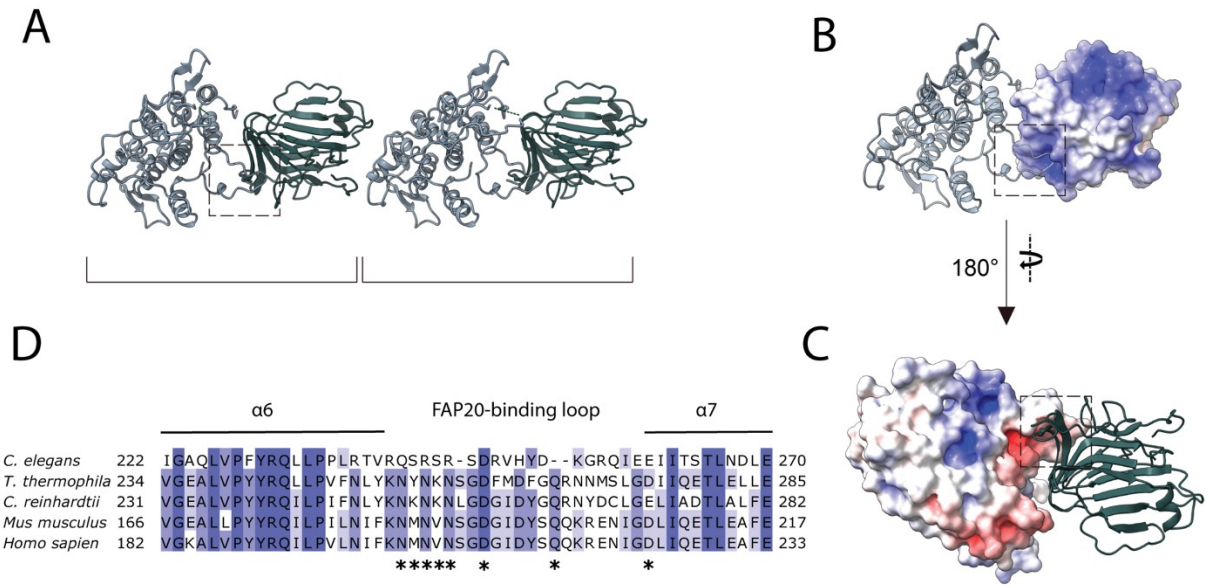

Figure 2.8.3 PACRG and FAP20 form a homo dimer.

(A) Consecutive molecules of PACRG and FAP20 in the IJ protofilament. PACRG and FAP20 form a heterodimer as indicated by brackets. (B, C) Electrostatic interactions between PACRG and FAP20 illustrated by their surface charge. The dashed boxes in (A, B, C) highlight the interacting loops between PACRG and FAP20. (D) Multiple sequence alignment of PACRG in the regions of FAP20-binding loop. Asterisks indicate residues that are involved in FAP20 binding.

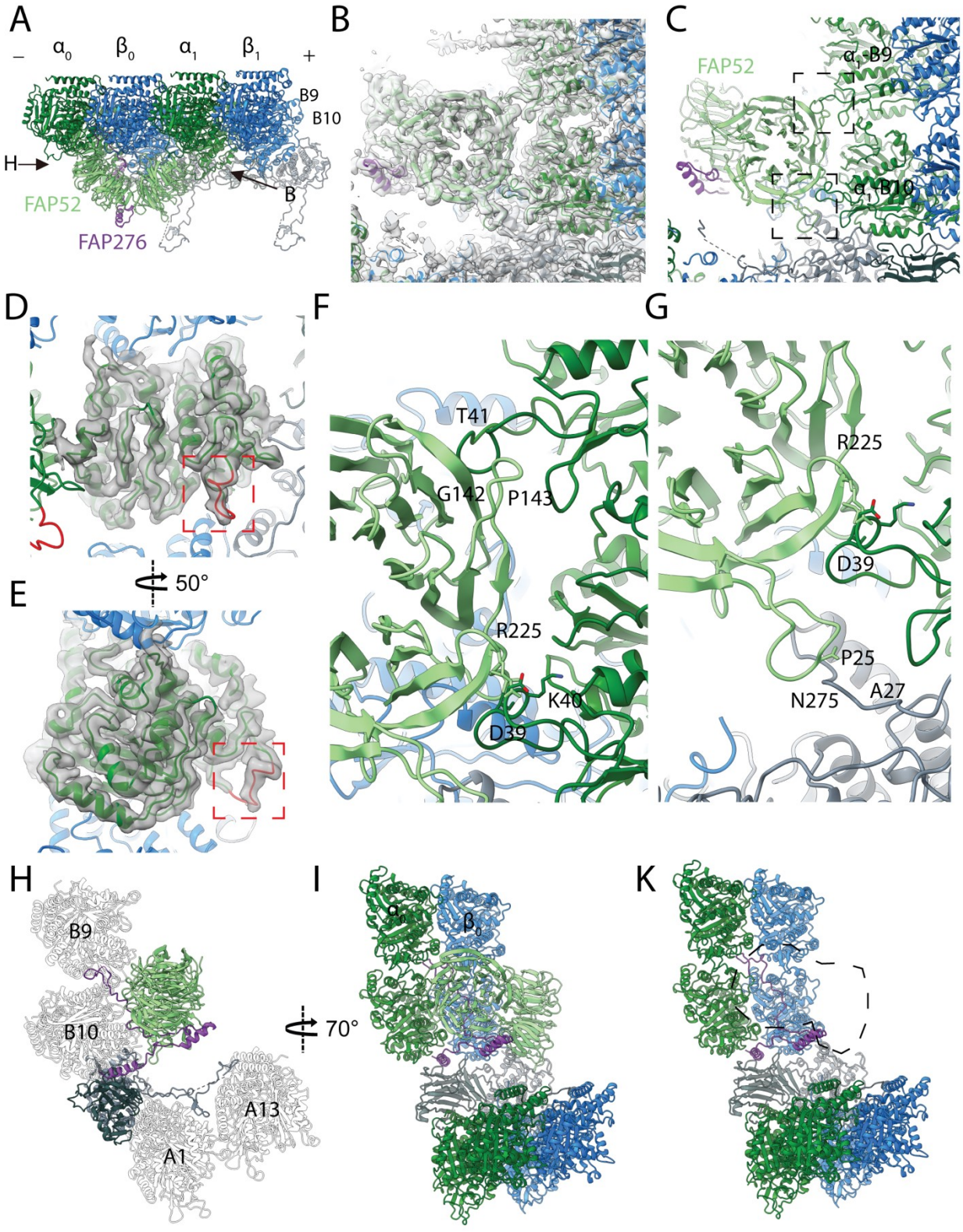

Figure 2.8.4 Structure of FAP52 and its interaction with tubulins and PACRG.

(A) Structure of FAP52 in a top view from the outside of the B-tubule looking down on the A-tubule. Black arrows indicate the direction of view in (B) and (H). (B, C) Interactions of FAP52 with α-tubulins from PF B8 and B9 and PACRG with (B) and without map overlay (C). (D-E) The structure of the α-K40 loop from PF B10. Red dashed boxes indicate the α-K40 loop. (F) Interaction of α-K40 loop of PF B9 and B10 with FAP52. In PF B10, residue D39 of α-tubulin appears to form a salt bridge with R225 from FAP52. In PF B9, T41 of α-tubulin appears to interact with segment G142-P143 from FAP52. (G) N275 from loop V268-L279 of FAP52 appears to interact with the N-terminus of PACRG in segment P25-A27. Loop V268-L279 in *Chlamydomonas* FAP52 is missing in the *Tetrahymena* and the human structures. (H-K) Interactions of FAP276 with FAP52, FAP20 and tubulins. In (K) FAP52 model is digitally removed to show the interactions underneath.

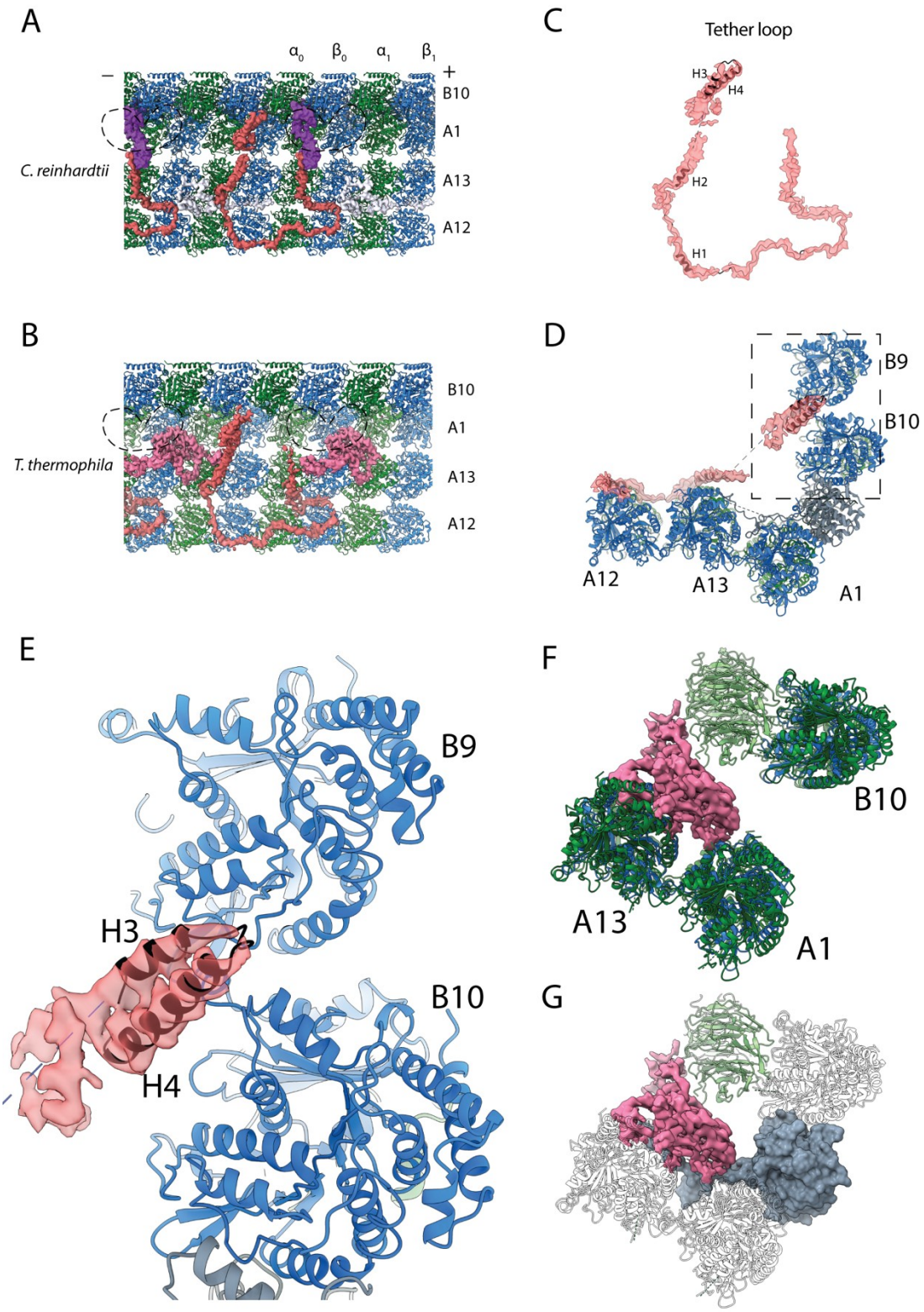

Figure 2.8.5 Structure of the Tether densities.

(A-B) At higher resolution, Tether densities 1 and 2 appear to be a single polypeptide chain in both *Chlamydomonas* (A) and *Tetrahymena* (B). The dashed regions indicate the location of FAP52, which has been digitally removed to show the Tether densities underneath. (C) Model of FAP106 fitted inside the segmented Tether loop from *Chlamydomonas*. (D) Model of FAP106 tethering the B-tubule and A-tubule. Dashed box indicates view in (E). (E) Helix H3 and H4 of FAP106 insert into the gap formed by four tubulin dimers of PF B9 and B10. (F) Structure of Tether density 3 from *Tetrahymena*, which binds on top of the wedge between PF A13 and A1. (G) Overlay of the PACRG from *Chlamydomonas* onto the structure of *Tetrahymena* shows a hypothetical steric clash of a long *Tetrahymena* PACRG N-terminus with Tether density 3.

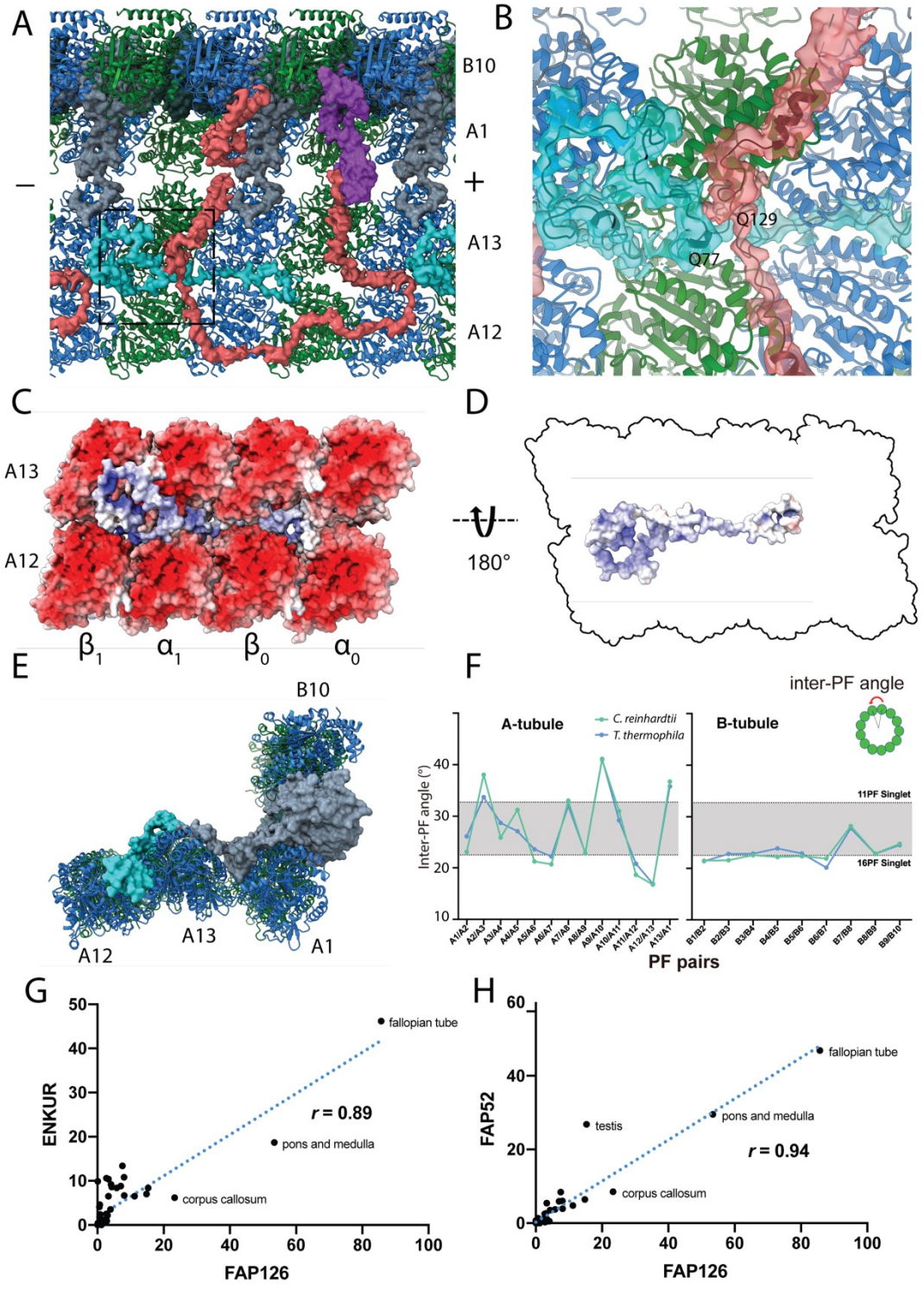

Figure 2.8.6 Structure of FAP126 and its interaction.

View from the top of the PF A12 and A13 showing the density of FAP126 (dark turquoise). Dashed box indicates view in (B). (B) Close up view of FAP126's interaction with the Tether loop, FAP106 at residues N74-T76 and Q129. (C) Complimentary electrostatic surface charges of tubulins and FAP126. (D) Electrostatic charge of FAP126 on the tubulin interacting surface. (E) The N-terminus of PACRG and the hook density go into the wedges between PF A12 and A13, and PF A13 and A1, respectively. This likely contributes to the curvature of this region. (F) Inter-PF angles of the A- and B-tubules from *Chlamydomonas* and *Tetrahymena* showing very similar angle distributions. (G) and (H) Correlation graphs of consensus normalized expression levels for two selected pairs of genes (ENKURIN(FAP106)/FAP126 and FAP52/FAP126). Tissues showing high levels of expression of one or both genes are labeled. Correlation coefficients (*r*) are indicated.

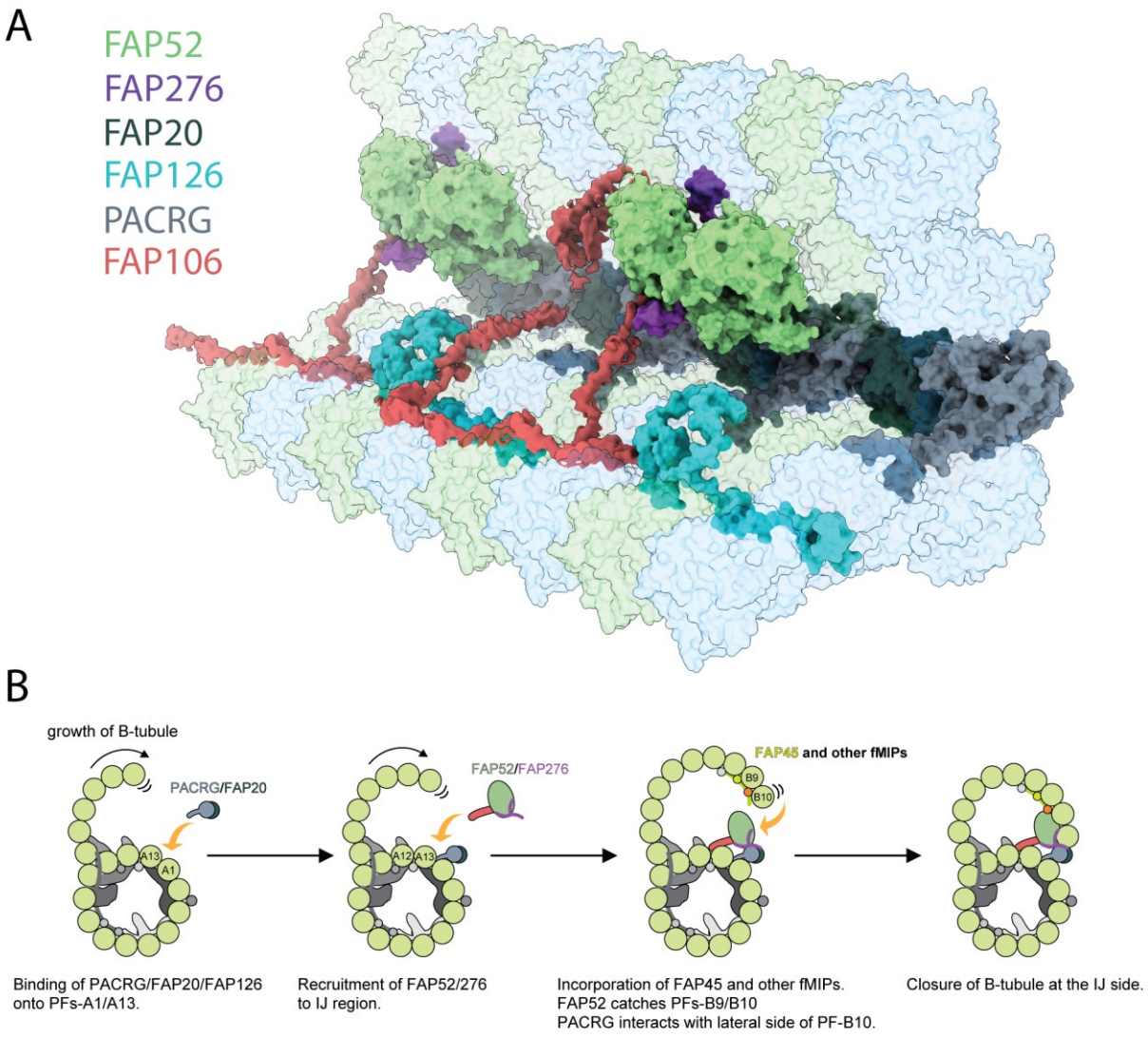

Figure 2.8.7 Proposed mechanism of IJ formation and B-tubule closure.

(A) Model of the IJ complex including PACRG, FAP20, FAP52, FAP126, FAP276 and the Tether loop. FAP45 is not depicted here. Tubulin is depicted as transparent. (B) The B-tubule starts growing laterally from the outer junction side as shown in [14]. PACRG and FAP20 form a hetero-dimer, which binds onto the outside surface of PF A1. After which, multiple alternative hypotheses are possible. One hypothesis is that FAP52, FAP276 and the Tether density proteins would bind onto PF A12 and A13. FAP45 and other fMIP proteins would then be incorporated inside the B-tubule, which fixes the proper curvature so that PF B9 and B10 can interact with other IJ proteins.

FAP52 binds both PF B9 and B10 through their K40 loops and finally, PACRG and FAP20 interact with the lateral side of PF B10 allowing for B-tubule closure.

Table 1: Proteins completely missing in FAP52 knockout mutant

Names	**Mol. weight (kDa)**	**p-values (WT vs FAP52)**	**Exclusive unique peptide counts in WT (**quantitative values after normalization)
ARL3	20	0.0013	2, 2, 1 (2, 1, 2)
CHLREDRAFT_171815	57	0.035	2, 6, 1 (2, 5, 2)
CHLREDRAFT_156073	11	0.024	1, 1, 1 (2, 1, 2)
FAP276	10	0.015	3, 3, 2 (8 ,7, 14)
FAP52	66	0.0046	27, 21, 15 (59, 73, 105)
FAP36	41	0.0023	3, 3, 1 (3, 3, 2)
CrCDPK1	54	<0.0001	3, 5, 2 (3, 4, 4)
CHLREDRAFT_176830	110	0.024	2, 1, 2 (2, 1, 1)
FAP173	33	0.012	3, 3, 1 (5, 3, 2)
FAP29	112	0.00045	2, 3, 2 (3, 3, 4)
CHLREDRAFT_181390	41	0.028	1, 1, 1 (1, 1, 2)
ANK2	60	0,0041	1, 2, 1 (1, 1, 2)

Table 2: Normalized spectral count of proteins detected by mass spectrometry.

Name	Molecular Weight in kDa (MW)	Average Quantitative Value (AQV)	Rough Stoichiometric Peptide Abundance (RSPA)*	*T.thermophila* Homologs**	Human Homologs***	Localization in *C. reinhardtii*
TUA1	50	1077.97	215.59	TBA_TETTH	TUBA1C	Doublet
TUB1	50	625.46	125.09	TBB_TETTH	TUBB4B	Doublet
RIB72	72	116.72	16.21	TTHERM_00143690	EFHC1	MIP
PACRG	25	38.39	15.35	TTHERM_00446290	PACRG	IJ
PF16	50	74.09	14.82	TTHERM_000157929	SPAG6	Central Pair
RSP9	30	41.79	13.93	TTHERM_00430020	RSPH9	Radial Spoke
FAP86	30	36.11	12.04	-	-	Doublet
FAP1	22	26.46	12.03	-	-	Doublet
FAP52	66	79.12	11.99	TTHERM_01094880	CFAP52	MIP
FAP20	22	26.08	11.86	TTHERM_00418580	CFAP20	IJ
FAP126	15	16.89	11.26	-	CFAP126	MIP
RSP1	88	98.73	11.22	TTHERM_00047490	RSPH1	Radial Spoke
FAP115	27	29.98	11.10	TTHERM_00193760	-	Doublet
FAP106	27	29.81	11.04	TTHERM_00137550	ENKUR	IJ?
Tektin	53	57.61	10.87	-	TEKT5	IJ?
RSP3	57	60.55	10.62	TTHERM_00566810	RSPH3	Radial Spoke
FAP252	39	39.97	10.25	TTHERM_00899430	CETN3	Axonemal
RSP2	77	77.95	10.12	-	CALM2	Radial Spoke
FAP161	43	43.50	10.12	TTHERM_00155380	CFAP161	Axonemal
IDA4	29	27.29	9.41	TTHERM_00841210	DNALI1	Dynein
FAP107	26	23.66	9.10	-	FLG2	Axonemal
DHC2	457	414.12	9.06	TTHERM_01027670	DNAH1	Dynein
FAP12	54	48.85	9.05	-	DAGLB	Cytoplasmic
RSP7	34	30.62	9.01	TTHERM_00194419	CALML5	Radial Spoke
RSP5	56	49.32	8.81	-	-	Radial Spoke
FAP230	45	39.59	8.80	-	-	Axonemal
FAP77	29	23.88	8.24	TTHERM_00974270	CFAP77	Axonemal

FAP55	111	90.47	8.15	-	MYH14	Axonemal
FAP90	28	22.35	7.98	-	WBP11	Axonemal
RSP10	24	19.10	7.96	TTHERM_00378600	RSPH1	Radial Spoke
FAP71	32	24.86	7.77	TTHERM_00077710	EWSR1	Axonemal
EEF1	51	39.04	7.66	TTHERM_00655820	Multiple	Axonemal
FAP182	49	36.69	7.49	TTHERM_01049330	C9orf116	Axonemal
				TTHERM_00624660	RIBC2	MIP
Rib43a	43	32.06	7.46	TTHERM_00641119		
FAP45	59	43.20	7.32	TTHERM_001164064	CFAP45	MIP

*RSPA was calculated by (AQV)/(MW)*10

** *T. thermophila* homologs were BLASTed using the Uniprot database

*** Human homologs were taken from the ChlamyFP project

2.9 Supplementary materials

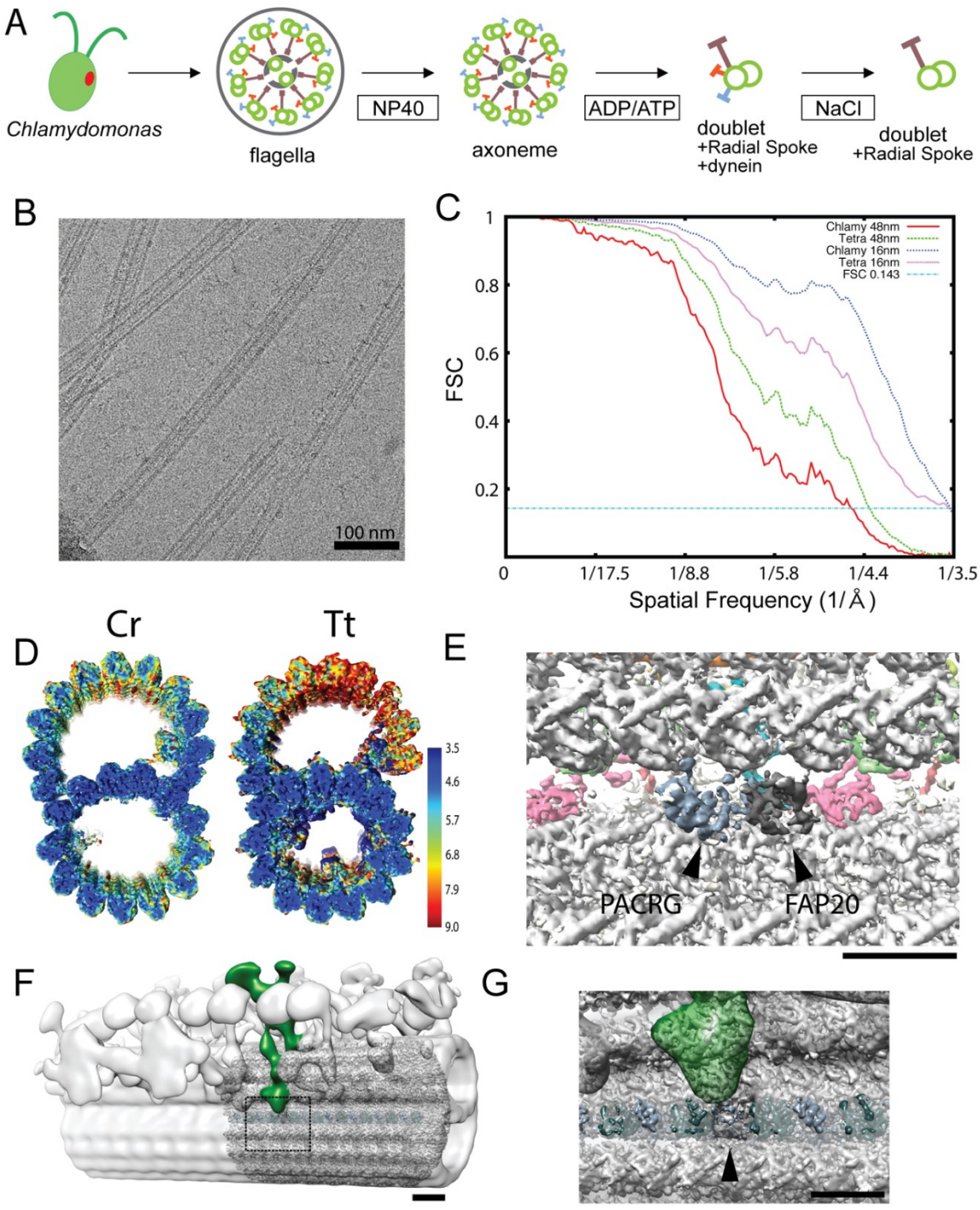

Figure 2.9.1 Data related to the doublet structures.

(A) Schematics of fractionation of the axoneme in this study. Doublets were split from axoneme, and outside proteins were removed to obtain a simpler sample for cryo-EM. (B) A typical cryo-EM image of *Chlamydomonas* doublets. (C) Gold-standard Fourier Shell Correlation of the 48-nm repeat and 16-nm repeat doublet maps of *Chlamydomonas* and *Tetrahymena*. (D) Local resolution estimation of the 16-nm repeat maps from *Chlamydomonas* and *Tetrahymena* using MonoRes. The resolution of the B-tubule in *Tetrahymena* is lower due to the loss of the IJ PF. (E) The remaining PACRG- and FAP20-like densities in the *Tetrahymena* doublet structure. (F) Superimposition of the tomographic structure of the intact doublet (EMD-2132) with the 48-nm structure of the *Chlamydomonas* doublet in this study. The DRC is colored green. (G) Enlarged view of the missing PACRG unit at the IJ PF, where the DRC binds.

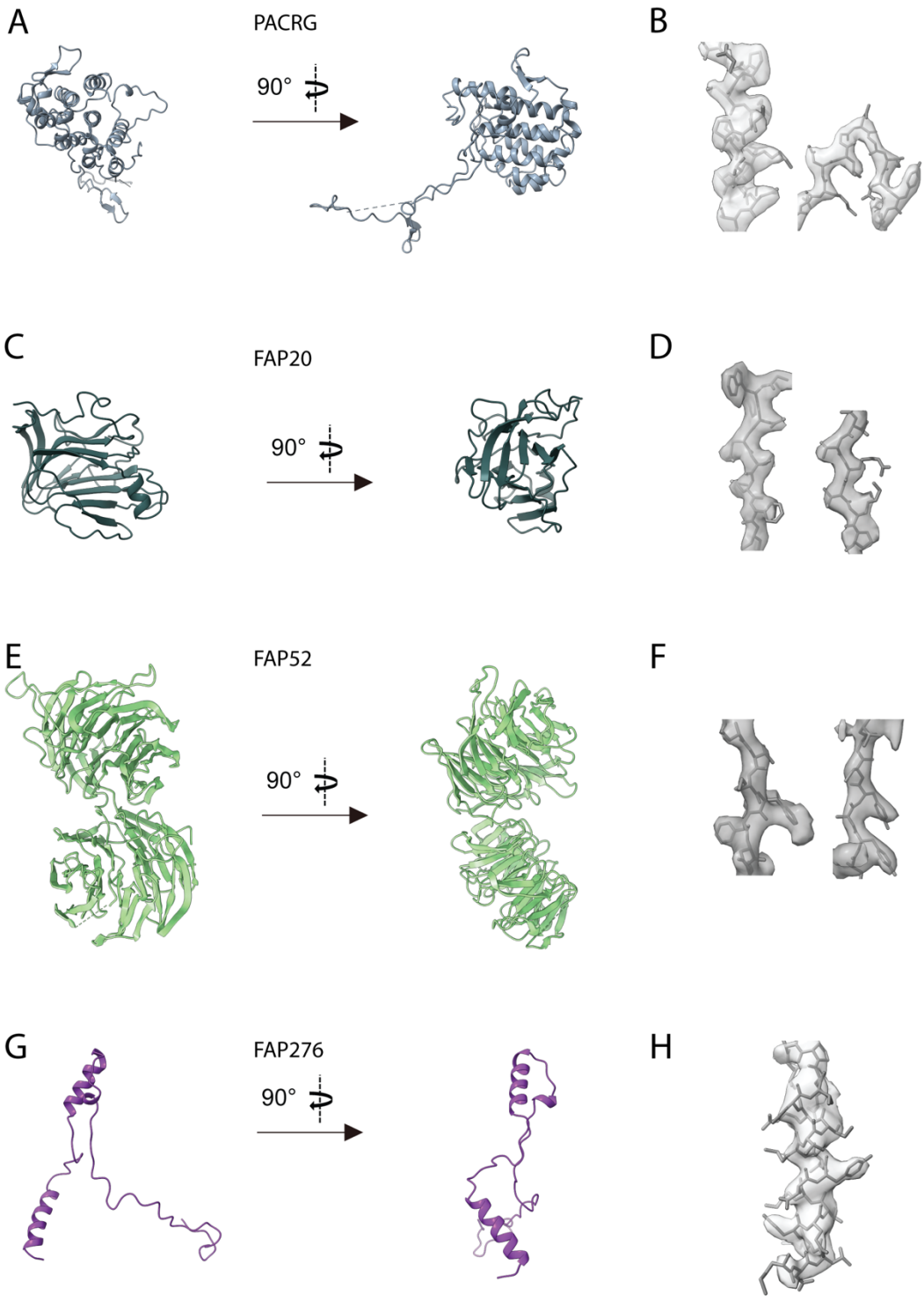

Figure 2.9.2 Atomic models of PACRG, FAP20, FAP52 and FAP276.

Atomic model of (A) PACRG, (C) FAP20, (E) FAP52 and (G) FAP276. Illustration of the cryo-EM density quality at selected regions of (B) PACRG, (D) FAP20, (F) FAP52 and (H) FAP276.

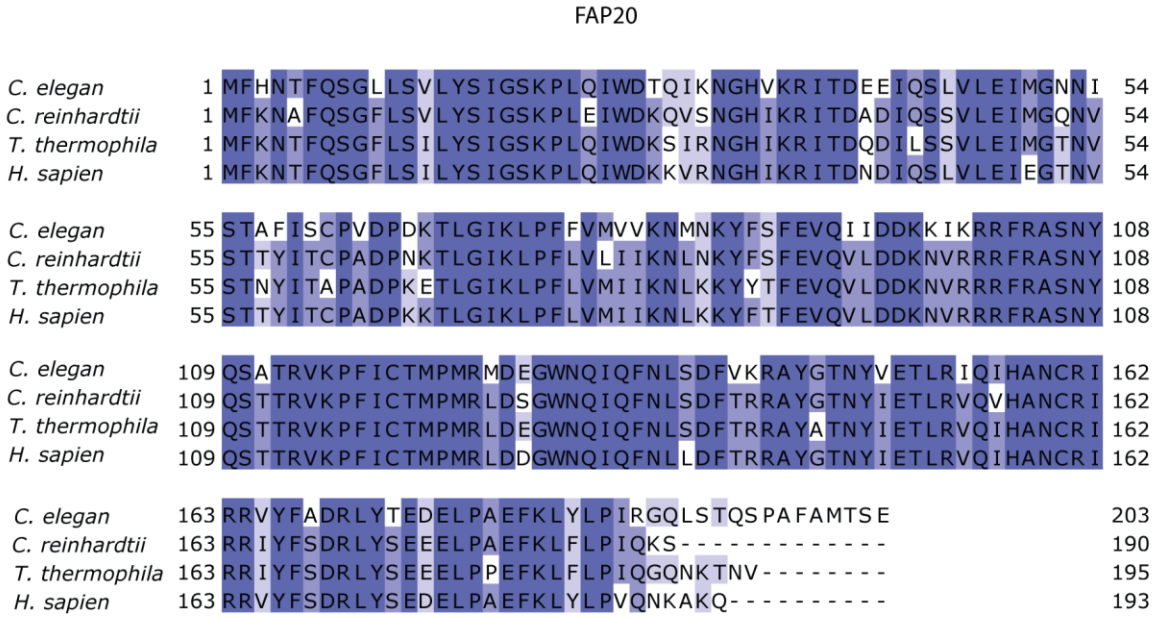

Figure 2.9.3 Multiple sequence alignment of FAP20 shows that it is highly conserved.

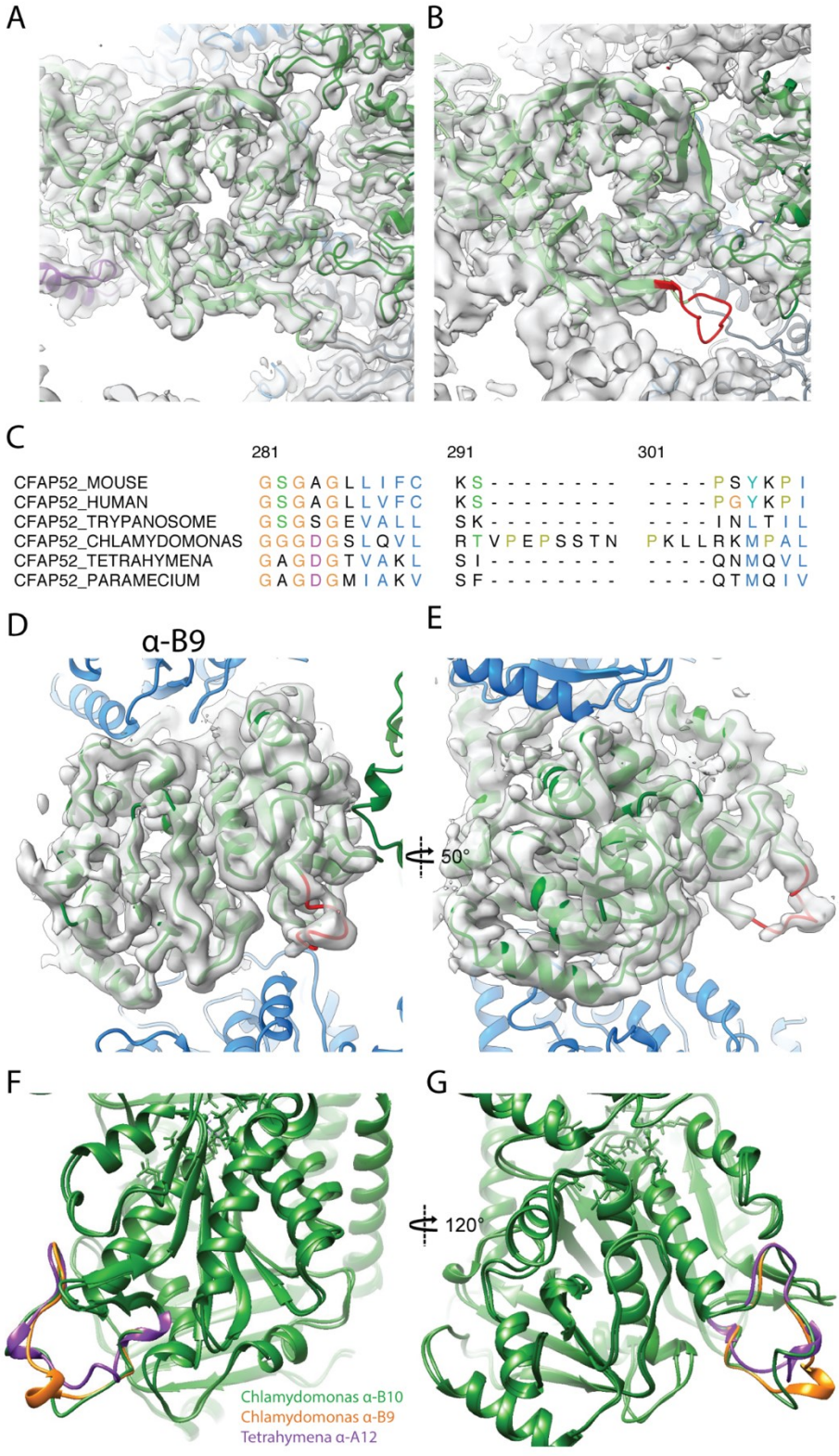

Figure 2.9.4 Data related to FAP52.

(A) Atomic model of *Chlamydomonas* FAP52 from inside the *Chlamydomonas* density map. (B) Atomic model of *Chlamydomonas* FAP52 fitted inside the *Tetrahymena* map highlights the longer loop (red) from *Chlamydomonas*. (C) Alignment of FAP52 from several species shows that *Chlamydomonas* has a longer loop in one beta propeller blade. The long loop is responsible for the interaction with PACRG. (D, E) α-K40 loop from PF B9 in *Chlamydomonas*. (F, G) Superimposition of the acetylated α-K40 loops from *Chlamydomonas* PF B9, B10 and *Tetrahymena* A12.

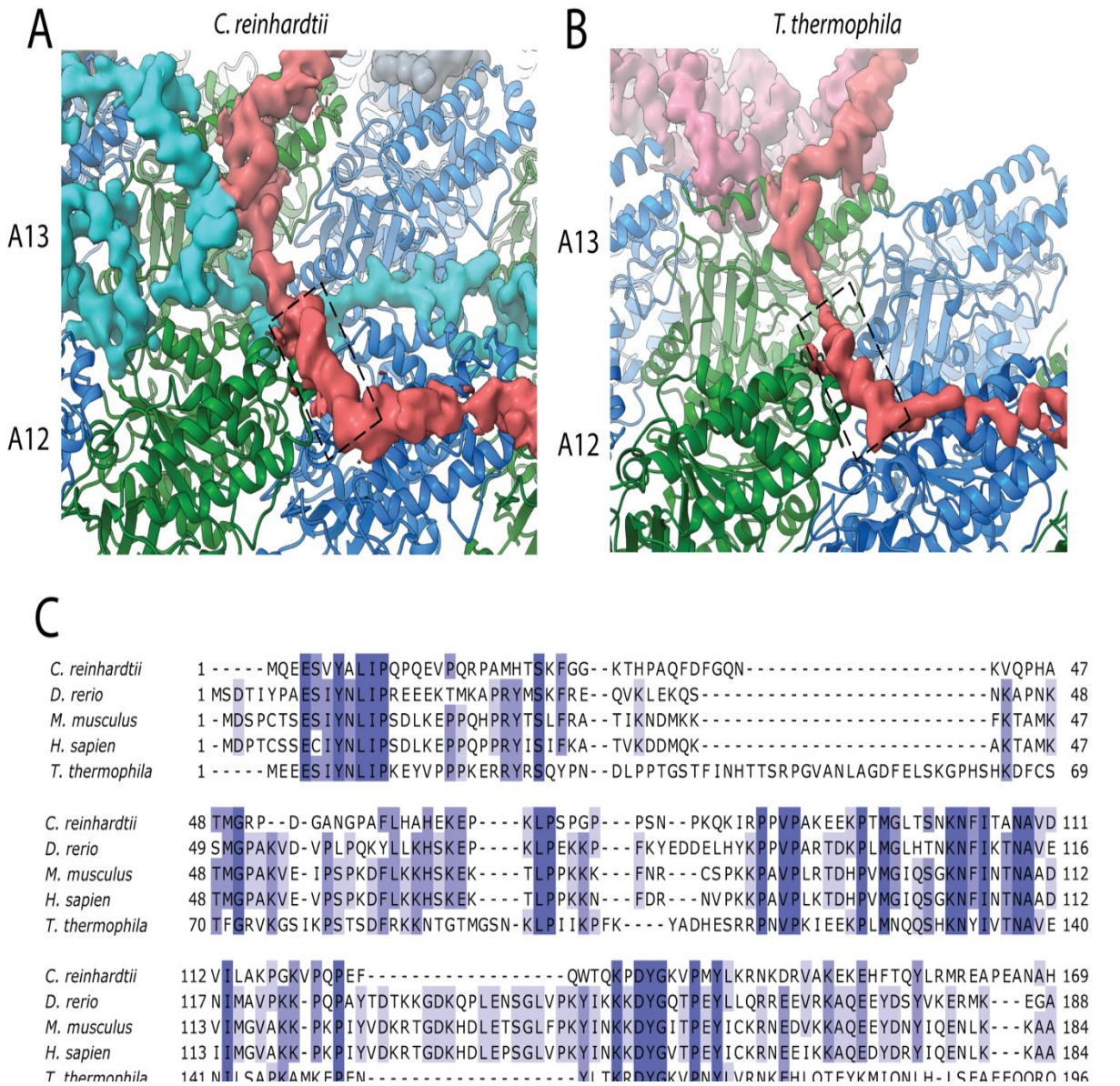

Figure 2.9.5 Data related to the Tether densities.

(A-B) The small helix (indicated by the dashed box) from *Chlamydomonas* (A) and *Tetrahymena* Tether loop appears to interact with α-tubulin. (C) Multiple sequence alignment of FAP106, the candidate for the Tether loop from a few organisms. (D) Secondary structure prediction of FAP106. The big cylinder represents helical prediction. Some of the beta-sheets are omitted since it is not easy to match beta-sheet with densities.

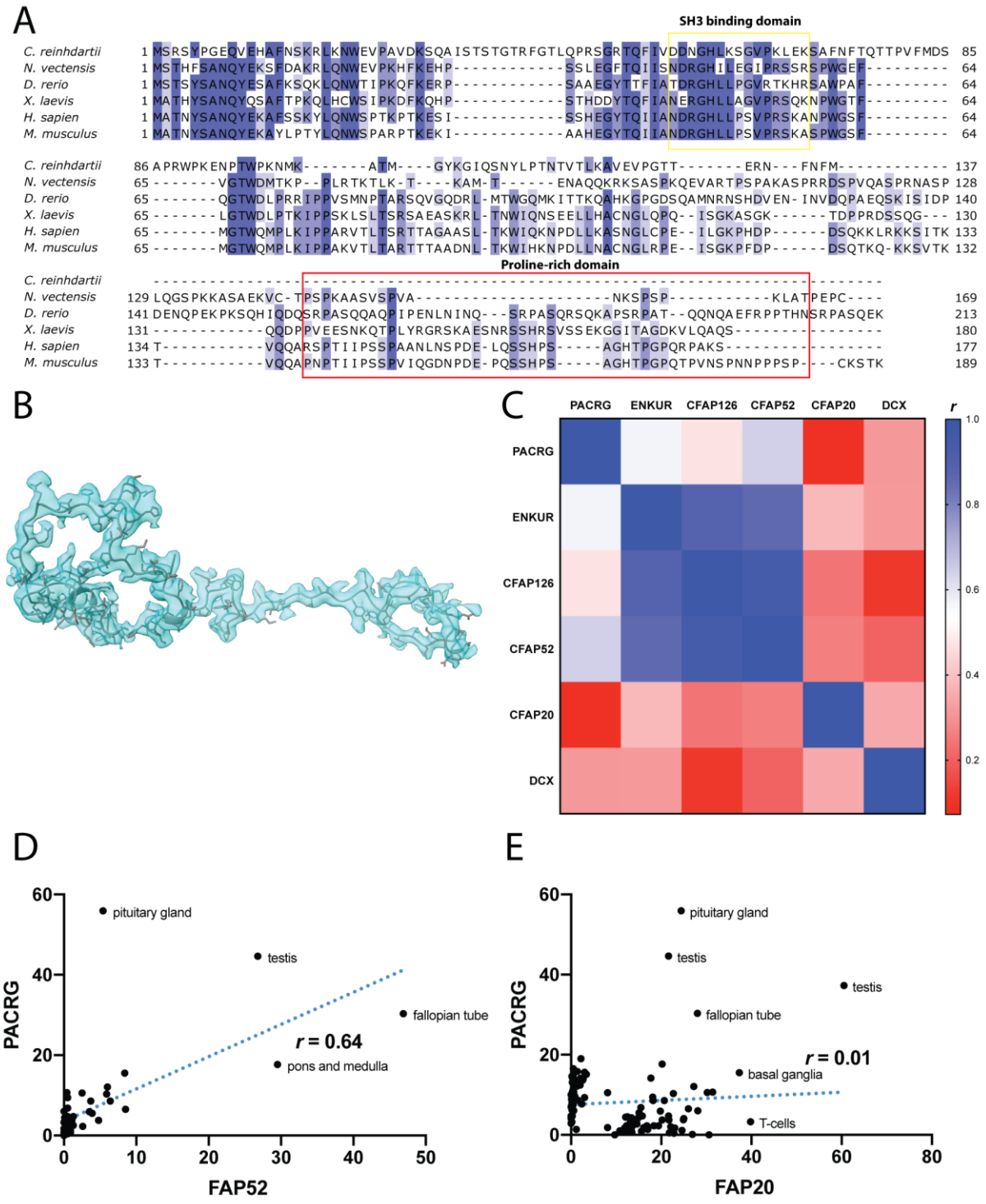

Figure 2.9.6 Data related to FAP126.

(A) Multiple sequence alignment of FAP126 from a few organisms. FAP126 of *Chlamydomonas* still have the SH3 binding domain while lacks the proline-rich region compared to other species.

(B) Atomic model of FAP126 fitted inside its segmented density. (C) Table of pairwise correlation coefficients between tissue mRNA expression levels, color-coded from low (red) to high (blue) values. ENKUR is the homolog of FAP106 in human. DCX is a microtubule associated protein in neuron, picked as a control. (D) Correlation graphs of consensus normalized expression levels for two selected pairs of genes (PACRG/FAP20 and PACRG/FAP52). Tissues showing high levels of expression of one or both genes are labeled. Correlation coefficients (*r*) are indicated.

Supplementary Table 1: Significantly reduced or missing proteins in FAP52 compared to WT using relative mass spectrometry quantification.

Names	Uniprot ID	**WT** exclusive unique peptide counts (quantitative values after normalization)	**FAP52** exclusive unique peptide counts (quantitative values after normalization)	**FAP52/WT ratio** (quantitative values were used)	**p-values (WT vs FAP52)**	**Log2(Fold Change (FAP52/WT))**
FAP20	**A8IU92**	**14, 10, 12 (27, 19, 33)**	**14, 12, 13 (33, 17, 18)**	**0.86**	**0.65**	**-0.31**
FAP45	**A8I9E8**	**31, 27, 12 (60, 37, 33)**	**31, 30, 30 (48, 43, 40)**	**1.01**	**0.96**	**0.016**
PACRG	**A8I2Z6**	**13, 9, 10 (41, 26, 48)**	**15, 13, 13 (70, 42, 38)**	**1.30**	**0.38**	**0.38**
Tektin	**A8J8F6**	**20, 22, 14 (60, 61, 52)**	**29, 24 24 (74, 45, 43)**	**0.88**	**0.74**	**-0.096**
ARL3	A8ISN6	2, 2, 1 (2, 1, 2)	0, 0, 0 (0, 0, 0)	0.0	0.0013	-10.0
CHLREDRAFT_171815	A8HQQ4	2, 6, 1 (2, 5, 2)	0, 0, 0 (0, 0, 0)	0.0	0.035	-10.0
CHLREDRAFT_156073	A8I1U2	1, 1, 1 (2, 1, 2)	0, 0, 0 (0, 0, 0)	0.0	0.024	-10.0
FAP276	A8J9P2	3, 3, 2 (8 ,7, 14)	0, 0, 0 (0, 0, 0)	0.0	0.015	-10.0
CFAP52	A8ILK1	27, 21, 15 (59, 73, 105)	0, 0, 0 (0, 0, 0)	0.0	0.0046	-10.0
FAP36	A8IZX7	3, 3, 1 (3, 3, 2)	0, 0, 0 (0, 0, 0)	0.0	0.0023	-10.0
CrCDPK1	A8IHF4	3, 5, 2 (3, 4, 4)	0, 0, 0 (0, 0, 0)	0.0	<0.0001	-10.0
CHLREDRAFT_176830	A8J922	2, 1, 2 (2, 1, 1)	0, 0, 0 (0, 0, 0)	0.0	0.024	-10.0
FAP173	A8JAF7	3, 3, 1 (5, 3, 2)	0, 0, 0 (0, 0, 0)	0.0	0.012	-10.0
FAP29	A8J3X6	2, 3, 2 (3, 3, 4)	0, 0, 0 (0, 0, 0)	0.0	0.00045	-10.0
CHLREDRAFT_181390	A8JJY2	1, 1, 1 (1, 1, 2)	0, 0, 0 (0, 0, 0)	0.0	0.028	-10.0
ANK2	A8HNK2	1, 2, 1 (1, 1, 2)	0, 0, 0 (0, 0, 0)	0.0	0,0041	-10.0

FAP5	A8JAI0	11, 15, 7 (23, 22, 23)	2, 0, 0 (1, 0, 0)	0.014	<0.0001	-5.5
FAP164	A8JC79	4, 5, 1 (6, 4, 2)	0, 0, 1 (0, 0, 0)	0.0	0.022	-5.1
FAP288	A8IJV3	13, 12, 9 (18, 14, 23)	2, 1, 1 (1, 0, 0)	0.018	0.0021	-4.6
CHLREDRAFT_177061	A8J9A4	7, 7, 2 (8, 6, 4)	0, 1, 1 (0, 0, 0)	0.0	0.0071	-4.5
TEF20	A8IL00	2, 1, 1 (2, 1, 2)	0, 1, 0 (0, 0, 0)	0.0	0.036	-3.6
CHLREDRAFT_191579	A8J3S1	2, 4, 2 (3, 4, 4)	1, 0 ,1 (1, 0 , 0)	0.09	0.0003	-3.4
CHLREDRAFT_111330	A8IAY6	2, 2, 1 (3, 1, 2)	1, 0, 0 (1, 0, 0)	0.16	0.03	-3.2
14-3-3	Q7X7A7	9, 9, 3 (15, 10, 6)	5, 0, 1 (4, 0, 0)	0.13	0.03	-3.0
Isocitrate lyase	A8J244	12, 8, 9 (23, 8, 19)	6, 2, 2 (5, 1, 1)	0.14	0.036	-2.9
CHLREDRAFT_141580	A8I9N1	7, 11, 4 (13, 16, 17)	3, 3, 3 (3, 2, 2)	0.19	0.0006	-2.7
Elongation Factor 2	A8JHX9	15,17,5 (27, 22, 10)	3, 6, 6 (3, 3, 3)	0.15	0.026	-2.7
CHLREDRAFT_189452	A8IT59	4, 6, 1 (5, 5, 2)	1, 1, 1 (1, 0, 1)	0.17	0.026	-2.7
CHLREDRAFT_175290	A8J364	4, 3, 2 (5, 3, 6)	1, 2, 2 (1, 1, 1)	0.21	0.014	-2.6
CHLREDRAFT_111269	A8IBY2	1, 4, 1 (1, 3, 2)	0, 2, 1 (0, 1, 0)	0.17	0.045	-2.4
FAP138	A8IUQ2	4, 6, 3 (8, 7, 6)	2, 3, 3 (1, 1, 1)	0.14	0.00046	-2.4
FAP31	A8JDM7	6, 8, 4 (8, 7, 8)	7, 0, 0 (5, 0, 0)	0.21	0.024	-2.2
IFT80	A8IXE2	4, 5, 1 (5, 4, 2)	1, 1, 2 (1, 1, 1)	0.27	0.022	-2.2
CHLREDRAFT_189792	A8HPX1	16, 21, 6 (18, 17, 12)	0, 11, 13 (0, 6, 5)	0.23	0.0096	-2.1
CHLREDRAFT_206178	A8IP72	17, 24, 10 (20, 19,23)	0, 15, 18 (0, 7, 8)	0.24	0.0053	-2.0
GSK3	Q6IV67	4, 3, 2 (5, 2, 4)	2, 2, 1 (1, 1, 0)	0.18	0.030	-1.8
CHLREDRAFT_144025	A8IF86	13, 27, 14 (16, 27, 35)	14, 12, 13 (11, 7, 7)	0.32	0.035	-1.7
FAP148	A8IAT9	29, 41, 11 (44, 52, 27)	14, 22, 26 (14, 12, 15)	0.33	0.022	-1.6

FAP85	A8J250	7, 11, 6 (14, 15, 19)	8, 4, 4 (10, 3, 2)	0.31	0.024	-1.6
Phototropin	A8IXU7	30, 22, 18 (56, 44, 64)	25, 14, 17 (41,12, 13)	0.40	0.041	-1.3
p38	A4PET3	3, 8, 4 (7 ,7, 8)	5, 3, 3 (5, 2, 1)	0.36	0.019	-1.3
FAP39	A8J0V2	6, 10, 4 (13, 11, 8)	9, 5, 4 (7, 4, 3)	0.42	0.022	-1.1

2.10 References

1. Satir, P. and S.T. Christensen, *Overview of structure and function of mammalian cilia.* Annu Rev Physiol, 2007. **69**: p. 377-400.
2. Hurd, T.W. and F. Hildebrandt, *Mechanisms of nephronophthisis and related ciliopathies.* Nephron Exp Nephrol, 2011. **118**(1): p. e9-14.
3. Bui, K.H., et al., *Molecular architecture of inner dynein arms in situ in Chlamydomonas reinhardtii flagella.* J Cell Biol, 2008. **183**(5): p. 923-32.
4. Bui, K.H., et al., *Asymmetry of inner dynein arms and inter-doublet links in Chlamydomonas flagella.* J Cell Biol, 2009. **186**(3): p. 437-46.
5. Bui, K.H., et al., *Polarity and asymmetry in the arrangement of dynein and related structures in the Chlamydomonas axoneme.* J Cell Biol, 2012. **198**(5): p. 913-25.
6. Heuser, T., et al., *The dynein regulatory complex is the nexin link and a major regulatory node in cilia and flagella.* J Cell Biol, 2009. **187**(6): p. 921-33.
7. Ichikawa, M., et al., *Subnanometre-resolution structure of the doublet microtubule reveals new classes of microtubule-associated proteins.* Nat Commun, 2017. **8**: p. 15035.
8. Ichikawa, M., et al., *Tubulin lattice in cilia is in a stressed form regulated by microtubule inner proteins.* Proceedings of the National Academy of Sciences, 2019.
9. Tilney, L.G., et al., *Microtubules: evidence for 13 protofilaments.* J Cell Biol, 1973. **59**(2 Pt 1): p. 267-75.
10. Linck, R.W. and R.E. Stephens, *Functional protofilament numbering of ciliary, flagellar, and centriolar microtubules.* Cell Motil Cytoskeleton, 2007. **64**(7): p. 489-95.
11. Nicastro, D., et al., *Cryo-electron tomography reveals conserved features of doublet microtubules in flagella.* Proc Natl Acad Sci U S A, 2011. **108**(42): p. E845-53.
12. Sun, S., et al., *Three-dimensional architecture of epithelial primary cilia.* Proc Natl Acad Sci U S A, 2019. **116**(19): p. 9370-9379.
13. Euteneuer, U. and J.R. McIntosh, *Polarity of midbody and phragmoplast microtubules.* J Cell Biol, 1980. **87**(2 Pt 1): p. 509-15.
14. Schmidt-Cernohorska, M., et al., *Flagellar microtubule doublet assembly in vitro reveals a regulatory role of tubulin C-terminal tails.* Science, 2019. **363**(6424): p. 285-288.
15. Yanagisawa, H.A., et al., *FAP20 is an inner junction protein of doublet microtubules essential for both the planar asymmetrical waveform and stability of flagella in Chlamydomonas.* Mol Biol Cell, 2014. **25**(9): p. 1472-83.
16. Dymek, E.E., et al., *PACRG and FAP20 form the inner junction of axonemal doublet microtubules and regulate ciliary motility.* Mol Biol Cell, 2019. **30**(15): p. 1805-1816.
17. Kitada, T., et al., *Mutations in the parkin gene cause autosomal recessive juvenile parkinsonism.* Nature, 1998. **392**(6676): p. 605-8.
18. West, A.B., et al., *Identification of a novel gene linked to parkin via a bi-directional promoter.* J Mol Biol, 2003. **326**(1): p. 11-9.
19. Thumberger, T., et al., *Ciliary and non-ciliary expression and function of PACRG during vertebrate development.* Cilia, 2012. **1**(1): p. 13.
20. Lorenzetti, D., C.E. Bishop, and M.J. Justice, *Deletion of the Parkin coregulated gene causes male sterility in the quaking(viable) mouse mutant.* Proc Natl Acad Sci U S A, 2004. **101**(22): p. 8402-7.
21. Wilson, G.R., et al., *Deletion of the Parkin co-regulated gene causes defects in ependymal ciliary motility and hydrocephalus in the quakingviable mutant mouse.* Hum Mol Genet, 2010. **19**(8): p. 1593-602.
22. Laligne, C., et al., *Bug22p, a conserved centrosomal/ciliary protein also present in higher plants, is required for an effective ciliary stroke in Paramecium.* Eukaryot Cell, 2010. **9**(4): p. 645-55.

23. Owa, M., et al., *Inner lumen proteins stabilize doublet microtubules in cilia and flagella.* Nat Commun, 2019. **10**(1): p. 1143.
24. Ta-Shma, A., et al., *A human laterality disorder associated with a homozygous WDR16 deletion.* Eur J Hum Genet, 2015. **23**(9): p. 1262-5.
25. Dai, D., et al., *Identification and mapping of central pair proteins by proteomic analysis.* bioRxiv, 2019.
26. Oda, T., et al., *A molecular ruler determines the repeat length in eukaryotic cilia and flagella.* Science, 2014. **346**(6211): p. 857-60.
27. Brouhard, G.J., et al., *XMAP215 is a processive microtubule polymerase.* Cell, 2008. **132**(1): p. 79-88.
28. Leano, J.B. and K.C. Slep, *Structures of TOG1 and TOG2 from the human microtubule dynamics regulator CLASP1.* PLoS One, 2019. **14**(7): p. e0219823.
29. Khan, N., et al., *Crystal structure of human PACRG in complex with MEIG1.* bioRxiv, 2019.
30. Wloga, D., et al., *Posttranslational Modifications of Tubulin and Cilia.* Cold Spring Harb Perspect Biol, 2017. **9**(6).
31. LeDizet, M. and G. Piperno, *Identification of an acetylation site of Chlamydomonas alpha-tubulin.* Proc Natl Acad Sci U S A, 1987. **84**(16): p. 5720-4.
32. Eshun-Wilson, L., et al., *Effects of alpha-tubulin acetylation on microtubule structure and stability.* Proc Natl Acad Sci U S A, 2019. **116**(21): p. 10366-10371.
33. Kellogg, E.H., et al., *Near-atomic model of microtubule-tau interactions.* Science, 2018. **360**(6394): p. 1242-1246.
34. Sutton, K.A., et al., *Enkurin is a novel calmodulin and TRPC channel binding protein in sperm.* Dev Biol, 2004. **274**(2): p. 426-35.
35. Jungnickel, M.K., et al., *The flagellar protein Enkurin is required for mouse sperm motility and for transport through the female reproductive tract.* Biol Reprod, 2018. **99**(4): p. 789-797.
36. Sigg, M.A., et al., *Evolutionary Proteomics Uncovers Ancient Associations of Cilia with Signaling Pathways.* Dev Cell, 2017. **43**(6): p. 744-762 e11.
37. Stauber, M., et al., *Identification of FOXJ1 effectors during ciliogenesis in the foetal respiratory epithelium and embryonic left-right organiser of the mouse.* Dev Biol, 2017. **423**(2): p. 170-188.
38. Gegg, M., et al., *Flattop regulates basal body docking and positioning in mono- and multiciliated cells.* Elife, 2014. **3**.
39. Herve, C., et al., *Carbohydrate-binding modules promote the enzymatic deconstruction of intact plant cell walls by targeting and proximity effects.* Proc Natl Acad Sci U S A, 2010. **107**(34): p. 15293-8.
40. Bechstedt, S. and G.J. Brouhard, *Doublecortin recognizes the 13-protofilament microtubule cooperatively and tracks microtubule ends.* Dev Cell, 2012. **23**(1): p. 181-92.
41. Portran, D., et al., *Tubulin acetylation protects long-lived microtubules against mechanical ageing.* Nat Cell Biol, 2017. **19**(4): p. 391-398.
42. Xu, Z., et al., *Microtubules acquire resistance from mechanical breakage through intralumenal acetylation.* Science, 2017. **356**(6335): p. 328-332.
43. Friedmann, D.R., et al., *Structure of the alpha-tubulin acetyltransferase, alphaTAT1, and implications for tubulin-specific acetylation.* Proc Natl Acad Sci U S A, 2012. **109**(48): p. 19655-60.
44. Kalebic, N., et al., *alphaTAT1 is the major alpha-tubulin acetyltransferase in mice.* Nat Commun, 2013. **4**: p. 1962.
45. Alper, J.D., et al., *The motility of axonemal dynein is regulated by the tubulin code.* Biophys J, 2014. **107**(12): p. 2872-2880.

46. Burton, P.R., *Luminal material in microtubules of frog olfactory axons: structure and distribution.* J Cell Biol, 1984. **99**(2): p. 520-8.
47. Lechtreck, K.F. and S. Geimer, *Distribution of polyglutamylated tubulin in the flagellar apparatus of green flagellates.* Cell Motil Cytoskeleton, 2000. **47**(3): p. 219-35.
48. Pathak, N., et al., *The zebrafish fleer gene encodes an essential regulator of cilia tubulin polyglutamylation.* Mol Biol Cell, 2007. **18**(11): p. 4353-64.
49. Witman, G.B., *Isolation of Chlamydomonas flagella and flagellar axonemes.* Methods Enzymol, 1986. **134**: p. 280-90.
50. Zheng, S.Q., et al., *MotionCor2: anisotropic correction of beam-induced motion for improved cryo-electron microscopy.* Nat Methods, 2017. **14**(4): p. 331-332.
51. Zhang, K., *Gctf: Real-time CTF determination and correction.* J Struct Biol, 2016. **193**(1): p. 1-12.
52. Tang, G., et al., *EMAN2: an extensible image processing suite for electron microscopy.* J Struct Biol, 2007. **157**(1): p. 38-46.
53. Zivanov, J., et al., *New tools for automated high-resolution cryo-EM structure determination in RELION-3.* Elife, 2018. **7**.
54. Vilas, J.L., et al., *MonoRes: Automatic and Accurate Estimation of Local Resolution for Electron Microscopy Maps.* Structure, 2018. **26**(2): p. 337-344 e4.
55. Webb, B. and A. Sali, *Protein structure modeling with MODELLER.* Methods Mol Biol, 2014. **1137**: p. 1-15.
56. Afonine, P.V., et al., *Real-space refinement in PHENIX for cryo-EM and crystallography.* Acta Crystallogr D Struct Biol, 2018. **74**(Pt 6): p. 531-544.
57. Adams, P.D., et al., *PHENIX: a comprehensive Python-based system for macromolecular structure solution.* Acta Crystallogr D Biol Crystallogr, 2010. **66**(Pt 2): p. 213-21.
58. Khan, N., et al., *Crystal structure of human PACRG in complex with MEIG1.* BioRvix, 2019.
59. Emsley, P., et al., *Features and development of Coot.* Acta Crystallogr D Biol Crystallogr, 2010. **66**(Pt 4): p. 486-501.
60. Yang, J., et al., *The I-TASSER Suite: protein structure and function prediction.* Nat Methods, 2015. **12**(1): p. 7-8.
61. Drozdetskiy, A., et al., *JPred4: a protein secondary structure prediction server.* Nucleic Acids Res, 2015. **43**(W1): p. W389-94.
62. Pettersen, E.F., et al., *UCSF Chimera--a visualization system for exploratory research and analysis.* J Comput Chem, 2004. **25**(13): p. 1605-12.
63. Goddard, T.D., et al., *UCSF ChimeraX: Meeting modern challenges in visualization and analysis.* Protein Sci, 2018. **27**(1): p. 14-25.

Preface

In the previous chapter, I showed how MIPs can have varying roles in the ciliary doublet, which complement and strengthen the inner junction structure. The inner junction is made up of a discontinuous arrangement of FAP20-PACRG heterodimers. Other MIPs appear to work synergistically from inside the lumen of the B-tubule to strengthen, stabilize and regulate the interactions at the inner junction. While all these findings certainly address some questions regarding the identity, localization, and structure of the inner junction, it raises questions regarding the role of the MIPs, their order of assembly, their mode of binding and how they maintain their periodicity in the doublet. The results of the previous chapter also suggest a more common role of MIPs in maintaining stability and in working synergistically. But do these roles carry over to other regions of the doublet? Could MIPs roles be further elucidated and validated in the most stable region of the doublet, which is its PF ribbon? This is what I will discuss in the chapter to follow.

Chapter 3: Tubulin Lattice in Cilia is in a Stressed Form Regulated by Microtubule Inner Proteins

Muneyoshi Ichikawa[1§†], Ahmad Abdelzaher Zaki Khalifa[1§], Shintaroh Kubo[3], Kaustuv Basu[2], Daniel Dai[1], Mohammad Amin Faghfor Maghrebi[1], Javier Vargas[1], Khanh Huy Bui[1,*]

[1]Department of Anatomy and Cell Biology, McGill University, Montréal, Québec, Canada, H3A 0C7

[2]Facility for Electron Microscopy Research, McGill University, Montréal, Québec, Canada, H3A 0C7

[3]Department of Biophysics, Graduate School of Science, Kyoto University, Kyoto 606-8502, Japan

[§] These researchers contributed equally to this work

[†]Present address: Department of Systems Biology, Graduate School of Biological Sciences, Nara Institute of Science and Technology, 8916-5, Takayama-cho, Ikoma, Nara 630-0192, Japan

[*] **Corresponding author. E-mail:** huy.bui@mcgill.ca

Short title: Tubulin lattice is regulated by MIPs

Keywords: Rib43a, doublet, microtubule, cilia, axoneme, cryo-electron microscopy

3.1 Preface

In this chapter, I identified and modelled two filamentous electron densities in the lumen of the A-tubule as the two homologues of Rib43a in *Tetrahymena* doublet. Here I present the first atomic models of MIPs that bind *in situ* to the tubulin lattice. The atomic models reveal that the short homolog of Rib43a bind to the taxane-binding pocket, where microtubule stabilizing agents are known to bind. The models further provide direct evidence of a MIP that alters the architecture of the tubulin lattice.

3.2 Abstract

Cilia, the hair-like protrusions that beat at high frequencies to propel a cell or move fluid around are composed of radially bundled doublet microtubules. In this study, we present a near-atomic resolution map of the *Tetrahymena* doublet microtubule by cryo-electron microscopy. The map demonstrates that the network of microtubule inner proteins weaves into the tubulin lattice and forms an inner sheath. From mass spectrometry data and *de novo* modelling, we identified Rib43a proteins as the filamentous microtubule inner proteins in the protofilament ribbon region. The Rib43a-tubulin interaction leads to an elongated tubulin dimer distance every two dimers. In addition, the tubulin lattice structure with missing MIPs by sarkosyl treatment shows a significant longitudinal compaction and lateral angle change between protofilaments. These results are evidence that the MIPs directly affect and stabilize the tubulin lattice. It suggests that the doublet microtubule is an intrinsically stressed filament and that this stress could be manipulated in the regulation of ciliary waveforms.

3.3 Significance Statement

Here, we present the first near-atomic resolution of the *ex vivo* doublet microtubule. This offers new insight into the intricacy of the *in vivo* tubulin lattice. Unlike the *in vitro* reconstituted singlet microtubule, the doublet tubulin lattice exhibits highly heterogeneous conformations and lateral curvatures due to the weaving network of microtubule inner proteins. We also reveal the molecular mechanism of how Rib43a proteins bind inside the lumen and induce significant changes in the tubulin lattice. This is the first time that a native protein is directly observed to bind to the taxane binding pocket of tubulin, similarly to the anti-cancer drug taxol.

3.4 Introduction

Microtubules are tubular structures composed of protofilaments (PFs) of α- and β-tubulin heterodimers in eukaryotes. Microtubules are responsible for structural support, tracks in intracellular transport and organization of organelles. In the cilia, nine doublet microtubules (doublets) are radially bundled to form an axonemal structure. The doublet is made up of a complete 13-PF A-tubule and an incomplete 10-PF B-tubule (Figure 3.10.1A). The doublet is the scaffold where ciliary proteins, such as axonemal dyneins and radial spokes, are periodically docked [1]. These proteins are important to initiate and regulate the bending motion of the cilia. The doublet also serves as the tracks for motor proteins kinesin-2 and dynein-2 carrying intraflagellar transport cargoes towards the distal tip and back [2]. Defects in ciliary proteins cause abnormal motility and function, hence, leading to cilia-related diseases, such as primary ciliary dyskinesia and Bardet-Biedl syndrome [3].

In contrast to the singlet microtubule (singlet) that shows cycles of growth and shrinkage called dynamic instability [4], the doublet is highly stable both *in vivo* and *ex vivo* [5]. In particular, the PF ribbon region, i.e. the shared region between the A- and B-tubules (Figure 3.10.1A) is stable even after high concentration of sarkosyl treatment [6, 7]. In the lumen of the doublet, microtubule inner proteins (MIPs) bind with a 48-nm periodicity to the tubulin lattice as shown by cryo-electron tomography [8-11]. Subnanometer structure of the isolated doublet by cryo-electron microscopy (cryo-EM) revealed many new MIPs forming an inner sheath inside the doublet. This inner sheath is composed of different classes of MIPs such as globular and filamentous MIPs (fMIPs). The fMIPs are composed of long α-helices running between the inner ridges of neighbouring PF pairs [5]. It is possible that these MIPs can exert its effects on the inherent properties of the doublet such as stability, rigidity, and damage resistance. This is similar to how microtubule-associated proteins affect the properties of singlets.

So far, there are not many well-characterized MIPs. Tektin isoforms in sea urchin sperm flagella are the first characterized PF ribbon proteins [6]. Rib43a, a 43-kDa protein is another PF ribbon candidate identified in the flagella of the green algae *Chlamydomonas reinhardtii*. However, the exact location of both tektin and Rib43a is unknown. Recently, Rib72a and Rib72b were characterized as components of MIPs inside the A-tubule of *Tetrahymena thermophila* [12]. Rib72a/b knockout causes a reduction in swimming speed. FAP45 and FAP52 are MIPs in the B-

tubule of *Chlamydomonas* [13]. The B-tubules of FAP45 and FAP52 double knockout mutants in *Chlamydomonas* are prone to depolymerization. All these MIPs mentioned above are conserved in humans [14]. Mutations in homologs of tektin, Rib72 and FAP52 are associated with diseases in humans [15-17]. Therefore, the MIPs must be important for the motility and stability of the cilia.

To date, there are no studies that reveal how MIPs affect the tubulin lattice at the molecular level. In this study, we obtained near-atomic resolution maps of the doublet and the A-tubule from *Tetrahymena* to understand the influence of MIPs on the tubulin lattice. In addition, we have revealed the molecular mechanism of how Rib43a induces changes in the tubulin lattice.

3.5 Results

3.5.1 The MIPs form a weaving network with the tubulin lattice

To gain insight into the molecular architecture of the *Tetrahymena* doublet, we obtained a cryo-EM map of the 48-nm repeating unit at 4.3 Å resolution (Figure 3.10.1A, B and Figure 3.11.1). This map reveals the intricacy of MIPs inside the doublet at a near-atomic level (Figure 3.10.1B to J). Even though each designated MIP density in Figure 3.10.1A and B contain multiple polypeptides, they are named and colored based on our previous work [5] (Figure 3.10.1A).

Instead of simply binding on the luminal surface of the doublet, MIPs consist of many branches, which weave into the tubulin lattice (Figure 3.10.1C-G). For instance, the previously identified MIP2 density consists of two long α-helices that extend from the inside of the A-tubule to the lumen of the B-tubule (Figure 3.10.1C, D). These helices appear to connect with densities from MIP7 at the outer junction.

MIP branches can lace through the A- and B-tubules to the outside of the doublet, a phenomenon that has never been observed with other microtubule-associated proteins. For instance, a part of MIP2 reaches through the lateral gap of PFs A10, A11 and B1 to the outside (Figure 3.10.1E). The branch of fMIP-A6A7 also weaves through the tubulin lattice and comes into contact with the outside filament-A6A7 (red arrowhead in Figure 3.10.1G). It is possible that the outside filament-A6A7 is a part of the outer dynein arm complex [18] due to its proximity and matching periodicity (24-nm). This suggests that there is a coordination between proteins inside and outside of the doublet.

Outside the B-tubule, there are many globular densities in the grooves between PFs B3 to B9. These densities are either protrusions from the fMIPs or densities binding outside (Figure 3.10.1A, B, I). However, this region has a lower signal-to-noise ratio due to lower resolution than the rest of the doublet (Figure 3.11.1F).

The previously described molecular ruler, referred to as "outside filament-A2A3" (Figure 3.10.1B, blue arrowhead) has been shown to determine the periodicity of axonemal proteins on the surface of the doublet [19] . However, we did not observe any connections between the MIPs and outside filament-A2A3.

The weaving network of MIPs is more complex in the A-tubule than the B-tubule. The A-tubule consists of laterally connected globular MIPs and fMIPs, while the B-tubule contains mainly fMIPs with fewer lateral contacts (Figure 3.10.1B, C, J). After sonication, singlet A-tubules with their B-tubule physically broken were observed together with doublet fragments (Figure 3.11.1A, C). Treatment of the doublet with 0.2% sarkosyl disintegrated the B-tubule but not the A-tubule (Figure 3.11.1A, B, D). The higher stability of the A-tubule compared to the B-tubule [20] may be attributed to such MIP interactions. This illustrates the importance of the MIPs in stabilizing the tubulin lattice.

3.5.2 The PF ribbon region displays a bimodal pattern of tubulin dimer distances

One unique feature of the doublet map is that it contains a 48-nm periodicity defined by the MIPs. We clearly distinguished α- and β-tubulins in the map and therefore, confirmed the microtubule seam between PFs A9 and A10 (Figure 3.11.2A-C). There are variations in dimer distances among PFs (Figure 3.10.2C, D). This heterogeneity even extends to the dimer distances within the same PF. This leads to an extremely heterogenous tubulin lattice relative to the singlet (Figure 3.10.2A-E). This should be a direct result of the weaving network of MIPs lacing into the tubulin lattice at different locations.

The lattice length of the B-tubule is slightly shorter than the A-tubule as in Figure 3.10.2D. The averaged dimer distance in the B-tubule is 82.4 Å, which translates as being 0.78% shorter compared to the A-tubule (83.1 Å). Since there are less MIPs in the B- than the A-tubule, this observation can be explained by the number of MIP insertions into the tubulin lattice. Indeed, the

B-tubule was previously proposed to be shorter than the A-tubule as the doublet from sea urchin sperm was found to form spring-like structure upon separating from the flagella [21].

The PF ribbon region (PFs-A1, A11-13) show a clear bimodal distribution with an oscillatory pattern of long and short dimer distances. Some PFs show rather uniform dimer distances such as PFs A2 and A3 (Figure 3.10.2E). Specifically, PFs A11-A13 shows a large difference of ~2 Å between the long and short dimer distances.

Recently published structures of singlets show that changes in the longitudinal tubulin dimer distance depend on the nucleotide states of β-tubulin [22-26]. Stable singlets in GTP state have an elongated dimer distance while the less stable GDP-state singlets have a compacted dimer distance [27]. In the doublet, the tubulins are in GDP state since we observed densities of GTP and GDP in the α- and β-tubulins respectively (Figure 3.11.2F-H). The averaged dimer distance of the 13-PF A-tubule of the doublet measured 83.1 Å (Table S1), which is closer to the elongated GTP-type distance (83.95 Å) than the compacted GDP-type distance (81.8 Å) in singlets from *Sus scrofa* [25]. We hypothesized that this elongated dimer distance is the result of the weaving network of the MIPs. In addition, the heterogeneity of dimer distances within and between the PFs suggest that the tubulin lattice of the doublet is inherently stressed by the insertion of MIPs.

3.5.3 Rib43a proteins are the fMIPs at the PF ribbon region

In order to investigate the molecular mechanism for the bimodal distribution, we looked at the currently known candidates for the PF ribbon associated proteins. Three possible candidates are tektin, Rib72 and Rib43a. *Tetrahymena* lacks a homolog of tektin. The predicted secondary structure of Rib72 is inconsistent with the long α-helical fMIP densities. Therefore, the fMIPs in the PF ribbon region are unlikely to be tektin or Rib72, but rather Rib43a. *Tetrahymena* has two Rib43a homologs (Unitprot ID: A4VDZ5, 142 amino acids and Q240R7, 280 amino acids). For convenience, we refer to the two *Tetrahymena* Rib43a homologs as Rib43a-S (A4VDZ5) and Rib43a-L (Q240R7) from now on.

Previously, both Rib43a proteins were detected in the mass spectrometry of the doublet [5]. In the 0.2% sarkosyl treated doublet, which contains mainly A-tubules, both Rib43a-S and Rib43a-L were also detected (Figure 3.11.3A). This indicates that both proteins exist in the A-tubule.

To improve the resolution of the PF ribbon region, we performed focused refinement to obtain a 4.16 Å resolved map of this region (Materials & Methods). By tracing the fMIP densities in the PF ribbon region, we were able to distinguish two unique peptide densities: a short 16-nm helical density (light blue in Figure 3.10.2F-K) and a long 32-nm density (orange in Figure 3.10.2F-K). In each 48-nm repeating unit, the fMIP-A12A13 comprises three copies of the short 16-nm helical density arranged in a head-to-tail fashion. The fMIP-A11A12 consists of the short 16-nm helical density (light blue in Figure 3.10.2F, K) and the long 32-nm filament (orange in Figure 3.10.2 F-K). The observed secondary structures of the short and long filament densities match the secondary structure prediction of Rib43a-S and Rib43a-L, respectively (Figure 3.10.3A). Rib43a-S is composed of a continuous stretch of α-helix of about 100 amino acids, referred to as the H1 region, while Rib43a-L contains two long stretches of α- helices of about 100 and 80 amino acids each (H1 and H2), connected by a linker region (Figure 3.10.3A).

We performed *de-novo* modelling of the short and long filament densities using the sequences of Rib43a-S and Rib43a-L. For Rib43-S, we were able to model almost the entire protein from residues 2 to 138. Residues 60 to 172 could only be modelled for Rib43a-L due to lower resolution. The secondary structure pattern and amino acid side chains unambiguously match the density signature (Figure 3.10.3B-D and Figure 3.11.2C, D). Therefore, we confirm that per 48nm repeat, the fMIPs in the PF ribbon region consists of four copies of Rib43a-S and one copy of Rib43a-L (Figure 3.10.2K).

3.5.4 Rib43a recognizes β-tubulin and induces the bimodal dimer distance

The N-terminus of the Rib43a-S inserts into the inter-tubulin dimer interface, in between helix H2 of β-tubulin and T7 loop of α-tubulin (Figure 3.10.3E-G). This leads to a longer dimer distance every two tubulin dimers in PF A13 and consequently, the bimodal pattern mentioned above. In addition, residue Y8 from Rib43a-S seems to interact with GDP of β-tubulin (Figure 3.11.3F). The N-terminus of the Rib43a-L does not insert into the inter-dimer interface but instead folds back onto helix H1 (Figure 3.10.2H and Figure 3.11.3C). We also observed densities that insert into the dimer interface at the N-terminal region and the linker region between H1 and H2 helices of Rib43a-L (Figure 3.10.2H and Figure 3.11.3E).

The consensus sequence GEDL of the Rib43a family is located at the N-terminus of helix H1 of both proteins (Figure 3.10.3A, D and Figure 3.11.3J). This region inserts into the S9-S10 loop of β-tubulin, which comprises the taxane binding pocket [28] (Figure 3.10.3D, H, Figure 3.11.3H, I). In α-tubulin, the S9-S10 loop is longer and would prevent the binding of Rib43a-S and Rib43a-L (Figure 3.11.2A). Therefore, we can conclude that the conserved motif GEDL of Rib43a is a β-tubulin binding motif at the taxane binding pocket. The main chain of residues 21 to 27 of Rib43a-S has a similar topology to the anti-cancer drug taxol, which binds at the taxane binding pocket (Figure 3.10.3H). In particular, the benzyl of F27 of Rib43a-S has a similar conformation to the 2-benzyol of taxol [28]. Although this F27 residue is not present in Rib43a-L, it is conserved in the Rib43a family (Figure 3.11.3J). Taxol selectively binds to β-tubulin and stabilizes the lateral interaction in the microtubule [28]. Therefore, it is possible that the binding of Rib43a-S to the tubulin lattice might have a similar stabilizing effect.

The helical region of Rib43a spans the M-loop of two longitudinal tubulin dimers. In the presence of Rib43a, the side chain of Y282 of α_1 and α_2-tubulins adopts a rotamer conformation at about a 90-degree rotation from its normal position (Figure 3.10.3I, J). This rotamer conformation is observed in all M-loops of α-tubulin in the presence of Rib43a. The conformation of Y282 in the absence of Rib43a such as PFs A10-A11 is consistent with what is observed in singlets [23]. In the PF ribbon region (A11-A12 and A12-A13), the normal conformation of Y282 will result in steric clash with the helices H1 and H2 of Rib43a. Therefore, it has to adopt a different rotamer conformation. This conformation might allow Y282 to interact with K60 from H2-S3 loop of the neighbouring α-tubulin, leading to a stronger lateral interaction. This observation suggests that Rib43a may play a role in restricting PF curvatures, consistent with the low curvatures observed in the PF pairs A11/A12 and A12/A13 [5].

With the extensive binding interface of both the N-terminal and the α-helical regions, we expect that Rib43a-S stabilizes the tubulin lattice. To test that hypothesis, we performed MD simulations of a short PF consisting of three tubulin dimers with and without Rib43a-S (Figure 3.11.3K-N). First, we compared the free energy at the inter-dimer interfaces to assess the effect of Rib43a-S on stability. The binding of the N-terminus of Rib43a-S greatly shifts the free energy of the inter-dimer interaction to a lower state, i.e. higher stability (Figure 3.11.3L). Although the effect of the α-helical region on stability is rather mild (Figure 3.11.3M), this stabilization effect would be much

stronger *in vivo* with the consecutive head-to-tail arrangement of Rib43a-S along the PF ribbon region. This is consistent with previous biochemical studies showing that the PF ribbon region is the most stable part of the doublet [7]. Next, we examined the effect of Rib43a-S on the elasticity of the PF. Without Rib43a-S, the free energy increases (less stable) at higher vibration angles (Figure 3.11.3N). In the presence of Rib43a-S, the PF maintains a low free energy even at higher vibration angles. This result demonstrates that Rib43a-S makes the PF more elastic, rather than rigid.

3.5.5 Removal of some MIPs impacts the compaction state and curvature of the doublet

We wanted to investigate whether removing MIPs would impact the tubulin lattice. Using micrographs of sonicated and sarkosyl treated fractions, we obtained two types of A-tubule maps: sonicated and sarkosyl A-tubules at 4.4 and 4.9 Å resolution respectively (Figure 3.10.4A-B). While the sonicated A-tubule map retains all the MIPs inside, the sarkosyl A-tubule map has missing MIP densities (Figure 3.10.4C). Multiple densities at the MIP4 and parts of the MIP6 areas are affected by the sarkosyl treatment (Figure 3.10.4D, E and Figure 3.11.4A, B). Other MIP densities inside the sarkosyl A-tubule are less-well resolved, suggesting they were partially removed or became flexible (Figure 3.10.4C).

Next, we wanted to see whether the lack of the B-tubule and the MIPs impact the dimer distances. The tubulin lattice of the sonicated A-tubule is almost identical to the doublet, except for the lack of the B-tubule (Figure 3.11.5A and Table S1). The tubulin lattice of the sarkosyl A-tubule showed a significant compaction compared to the doublet (Figure 3.10.5A-E; Figure 3.11.4C-F; Table S1). The averaged dimer distance measured 81.1 Å, which is similar to a GDP-type compacted lattice [23]. Therefore, this compaction can be attributed to the loss of the MIPs, but not the lack of the B-tubule. Both Rib43a-S and Rib43a-L were not removed by the sarkosyl treatment (Figure 3.10.4D). Therefore, the bimodal pattern was still maintained in the sarkosyl A-tubule (Figure 3.11.5A).

In addition to the lattice compaction, we also observed changes in the inter-PF angles (Figure 3.10.5F and Figure 3.11.5B). Unlike the 13-PF singlet, which forms a near perfect circle, the A-tubule of the doublet shows a squashed cross-sectional curvature with a variety of inter-PF angles (Figure 3.10.5F). Compared to the doublet, the inter-PF angles from the sarkosyl A-tubule show significant changes at PF pairs A1/A2 and A12/A13 (Figure 3.10.5F and Table S3). The MIPs are

missing at these PF pairs accordingly (Figure 3.10.4C-E). The PF pair-A12/A13 of the sarkosyl A-tubule, where several MIP4 densities are lost, shows the largest change of angle (Figure 3.10.5F and Figure 3.11.5B). The lateral curvature between PF pairs-A12/A13 of the doublet is equivalent to the curvature of a 22-PF singlet. This curvature is energetically unfavorable as 11 to 16 PF singlets are generally formed by *in vitro* reconstitution [29]. With the loss of MIP4, the curvature shifts towards a more relaxed conformation comparable to an 18-PF singlet (Figure 3.10.5F-H). PF pair-A9/A10 also shows a slight change in the angle without any MIPs missing (Figure 3.10.5F). This is the location of the seam [5] where the lateral interaction is the weakest [23]. Thus, this slight angle change could be the result of the tubulin lattice accommodating the local angle changes.

3.6 Discussion

In this paper, the *ex vivo* structure of the doublet offers insight into the structural intricacies and complex interplay between MIPs and the tubulin lattice. Our results are the direct evidence that the MIPs influence the tubulin lattice architecture.

The MIPs work in a coordinated fashion to keep the doublet in a stable and squashed cross-section. This likely facilitates the specific and proper formation of the B-tubule [5]. The network of MIPs prevents the loss of tubulin and spontaneous breakage by weaving into the tubulin lattice as an integrated layer (Figure 3.10.6A). For a singlet, mechanical stress from repeated cycles of bending and release is shown to induce local damage [30]. Motile cilia are under even higher mechanical stress due to high-frequency beating. Nevertheless, they are protected by the weaving network of MIPs. The doublet has been *in vitro* reconstituted from tubulin that have its flexible C-terminus cleaved by subtilisin [31]. This suggests that the MIPs can limit the C-terminal conformation *in vivo* for the initial assembly of the B-tubule. Therefore, the MIPs might play an important role in facilitating the assembly of the doublet.

We also reveal that two Rib43a homologs, Rib43a-S and Rib43a-L, are the fMIPs in the PF ribbon region. By performing MD simulation, we gained insight into how Rib43a stabilizes the tubulin lattice at the molecular level. The Rib43a-S induces the bimodal distance in the ribbon region by inserting into the interdimer interface every two dimers. Both Rib43a proteins bind consecutively

to form a 48-nm fMIP-A11A12. In *Chlamydomonas* and other species, Rib43a exists as a ~43-kDa protein, with a secondary structure prediction of three long helices (equivalent to roughly 48-nm in length). Therefore, Rib43a might be the inside molecular ruler for the 48-nm periodicity of the doublet lumen, a role similar to the outside molecular ruler, FAP59 and FAP172 [19]. Previously, tektin was proposed to regulate the complex spacing inside the doublet [10, 32]. However, as tektin is not present in *Tetrahymena*, it is likely that Rib43a is the primary inside ruler. It might then act as an assembly scaffold with specific binding domains for recruiting other MIPs and establishing distinct periodicities. In addition, the tight interaction of the Rib43a-S to the tubulin lattice suggests that it might be co-assembled with tubulin during ciliogenesis.

The taxane binding site is known to be used by small molecules, such as paclitaxel, zampanolide [28] and epothilone A [33]. Previously, tau was reported to bind to the taxane-binding pocket by visualization of nanogold conjugation [34], however this finding was not reproduced in a more recent high resolution study [35]. Our work provides direct evidence that a native protein is using the taxane-binding pocket to stabilize the tubulin lattice. In addition, taxol is shown to induce deformation in the microtubule wall [28]. This effect can also be exerted by Rib43a to induce low curvatures at the PF ribbon region. There could be other proteins utilising the same approach to stabilize the microtubule lattice not only in cilia but also in cytoplasmic microtubules. Finding such proteins using bioinformatic approaches can be a first step towards understanding how microtubules are stabilized by regulatory proteins.

Recent studies demonstrate that the elongation and compaction of the tubulin lattice plays an important role in the dynamic instability of singlet microtubules [22-26]. Microtubule-associated proteins can have a direct effect on the lattice compaction and, hence, microtubule dynamics [26]. Our results suggest that the MIPs, in particular Rib43a, function as a molecular jack to regulate the tubulin lattice in an elongated state (Figure 3.10.6B). This points to a common mechanism where the lattice maintenance is used to regulate stability and properties such as ciliary waveform. A previous study showed that doublets purified from sea urchin sperm flagella form spring-like structures, the shape of which, depends on the pH or calcium ion concentration [21]. This implies that the degree of inherent tension inside the doublet can be tweaked by external cues. Coincidentally, Rib72a [12] and FAP85 [36] are two MIP candidates that have calcium binding

domains. Thus, MIPs could manipulate tubulin conformations as a way to modify the rigidity and elasticity of the doublet and, thus, ciliary bending (Figure 3.10.6B).

Since Rib43a induces a conformational change in the M-loop region, it can act as a molecular wedge to lock the PF pairs at a low curvature (Figure 3.10.5F, Figure 3.10.6C). Conversely, there may be MIPs, which act as a molecular linker, which results in a high-curvature (Figure 3.10.6C). For example, MIP2 can be a molecular linker as it was shown to insert into the PF pair A9/A10 [5], which has a significantly high curvature (Figure 3.10.5F). Recently, it was reported that the microtubule-binding domain of axonemal dynein DNAH7 could induce large distortions in the microtubule cross-sectional curvature [37]. This suggests that there is a preferential curvature for the microtubule-binding domain of DNAH7. Distortions in the doublet cross-sectional curvature caused by MIPs might then facilitate the axonemal dynein to interact with specific regions.

Herein, we propose a lattice centric model for the cilia in which the tubulin lattice serves as a platform to integrate the binding signals of the MIPs and outer proteins. Binding of the MIPs leads to the local and global lattice rearrangement, which affects the affinity of the outer proteins like axonemal dyneins and radial spokes. This allows the assembly of the complex axoneme in an orderly fashion [1] for proper ciliary function. The unique dimer distances among different PFs and the inside-to-outside connections can influence the binding affinity of the intraflagellar transport motors to the A- or B-tubules selectively [2].

3.7 Acknowledgements

We thank Gary Brouhard, Susanne Bechstedt, Joaquin Ortega, Alba Guarne for helpful discussion and Kelly Sears for editing the manuscript. We thank Facility for Electron Microscopy Research of McGill University. Funding: This work was supported by grants from the Natural Sciences and Engineering Research Council of Canada (Discovery Grant 69462), Canada Institute of Health Research (Project Grant 388933), the Canada Institute for Advanced Research Arzieli Global Scholars Program to KHB and Natural Sciences and Engineering Research Council of Canada (Discovery Grant RGPIN-2018-04813) to JV. MI is supported by JSPS Overseas Research Fellowships. AAZK is a Recipient of the Al Ghurair STEM program scholarship from the Abdulla Al Gurarir Foundation for Education. SK is supported by JSPS Fellowship. We declare no competing financial interests. The electron microscopy maps of the doublet, sonicated A-tubule and sarkosyl A-tubule are available in the EM Data Bank (www.emdatabank.org) under accession numbers EMD-20602, EMD-20603 and EMD-20606. The coordinates of tubulin lattice, Rib43a-S and Rib43a-L are available in PDB under accession number 6U0H, 6U0T and 6U0U.

3.8 Materials and Methods

Sample preparation

Tetrahymena doublet fragments were prepared as in Ichikawa *et al*., [5] (Figure 3.11.1A, B). In brief, *Tetrahymena* cells (SB255 strain) were cultured in 1L of SPP media [1% proteose peptone No.3, 0.2% glucose, 0.1% yeast extract, 0.003% ethylenediaminetetraacetic acid ferric sodium salt (Fe-EDTA)]. Cilia were isolated by dibucaine method [38] and resuspended in cilia final buffer [CFB; 50 mM 4-(2-hydroxyethyl)-1-piperazineethanesulfonic acid (HEPES), pH 7.4, 3 mM MgSO4, 0.1 mM ethylene glycol tetraacetic acid (EGTA), 0.5% Trehalose, 1 mM dithiothreitol (DTT)] containing 1 mM phenylmethylsulfonyl fluoride (PMSF). Cilia were de-membraned by adding NP-40 (final concentration 1.5%), split by adding ATP (final concentration 0.4 mM), and incubated in CFB containing 0.6 M NaCl for 30 min on ice twice to remove dyneins. *Tetrahymena* doublets were dialyzed against low salt buffer [5 mM HEPES, pH 7.4, 1 mM DTT, 0.5 mM ethylenediaminetetraacetic acid (EDTA)] to deplete radial spokes, and then, fragmented by sonication and resuspended in CFB containing 0.6 M NaCl to avoid aggregation of doublet fragments. After sonication, the sample contained short doublet fragments but also A-tubule only fragments.

For the sarkosyl A-tubule, the doublets after twice 0.6 M NaCl treatment and dialysis were incubated with CFB containing 0.2% sarkosyl to remove the B-tubule for 10 min on ice. Sonication was not performed on this sample prior to electron microscopy.

Mass Spectrometry

In previous work, we performed in-gel digestion of stacking gel of the doublet preparation [5] using standard method [39]. In this study, we cut gel bands from different positions in the SDS gel of the sarkosyl A-tubule sample and performed in-gel digestion. The samples were analysed using a Thermo Orbitrap Fusion mass spectrometer with HCD sequencing all peptides with a charge of 2+ or greater. The raw data was searched against the *Chlamydomonas* proteins from Uniprot and then visualized by Scaffold Viewer 4.4.8 (Proteome Sciences) for statistical treatment and data visualization.

Electron Microscopy

3.5 µl of the sample of fragmented doublets (~4 mg/ml) or the sarkosyl A-tubule (~500 µg/ml) was applied to a glow-discharged holey carbon grid (Quantifoil R2/2), blotted and plunged into liquid

ethane using Vitrobot Mark IV (Thermo Fisher Scientific) at 25℃ and 100% humidity with a blot force of 3 or 4 and a blot time of 5 sec. Movies of seven frames were obtained on a Titan Krios (Thermo Fisher Scientific) equipped with Falcon II camera at 59,000 nominal magnification. The calibrated pixel size was 1.375 Å/pixel. Both datasets for the doublet and sarkosyl A-tubule were obtained with a total dose of ~30-45 electrons/Å^2. The defocus range was set to between -1.2 and -3.8 µm.

Image Processing

The movies were motion corrected and dose-weighted using MotionCor2 [40] implemented in Relion3 [41] and the contrast transfer function parameters were estimated using Gctf [42]. After discarding micrographs with apparent drift and ice contamination, bad contrast transfer function estimation, 7,838 micrographs for doublet and 5,179 micrographs for sarkosyl treated A-tubule were used, respectively. The filaments (doublet and A-tubule) were picked using e2helixboxer [43]. Since the preparation of doublet yielded both doublets and A-tubules (Figure 3.11.1A), we also picked the A-tubule from the micrographs for the doublet.

The particles of 512 x 512 pixels were initially picked with 16-nm periodicity and pre-aligned using a modified version of the Iterative Helical Real Space Reconstruction script https://www.nature.com/articles/ncomms15035 - ref37 [44] in SPIDER [45] to work with non-helical symmetry. After that, the particles were separated into three classes by multiple reference projection matching by Frealign [46]. The three classes above are (i) the 48-nm structures of the doublet from Ichikawa et al. [5] and 16-nm shifted structure in the longitudinal axis to the plus end (ii) and minus end (iii). This multiple reference projection matching allowed us to sort the particles belonging to each 48-nm class. The particles were then re-extracted in Relion and rescaled to a pixel size of 1.750 Å/pixel for faster processing. The aligned parameters were converted to Relion star file format for local refinement. In summary, 60,386 and 36,375 particles for doublet and A-tubule yielded maps of 4.7 and 4.8 Å resolution, respectively. 40,850 particles for sarkosyl A-tubule yielded a 5.2 Å resolution map. After iterative per-particles-defocus refinement and Bayesian polishing in Relion 3, the resolutions of the doublet, sonicated A-tubule and sarkosyl A-tubule maps were improved to 4.3, 4.4 and 4.9 Å, respectively. The doublet and sonicated A-tubule maps were sharpened using Relion-3 with a B-factor of -190 and -179 Å^2, respectively.

Since the sarkosyl A-tubule map exhibited a slightly preferred orientation and resolution heterogeneity in the structure, we performed a local restoration and local sharpening to reduce artifact and restore connectivity from preferred orientation and resolution heterogeneity (Figure 3.11.1G-J). To ensure the local restoration and local sharpening did not alter the maps, we performed the local restoration and local sharpening of the doublet and A-tubule. There were no artifacts observed compared with global sharpening.

To improve the resolution of the PF ribbon region, we performed a focused refinement by using a mask covering the PF ribbon region and also PF A9, A10 and B1. The resulting map has a resolution of 4.16 Å.

Local resolution estimation was performed using Monores [47] (Figure 3.11.1F).

Difference Map

To reliably identify the densities missing in the sarkosyl A-tubule, the unsharpened maps of the sonicated and sarkosyl A-tubule were filtered to 6 Å before performing difference mapping in Chimera. After the subtraction, the regions of difference were mapped onto the sarkosyl A-tubule map as shown in Figure 3.10.4C.

Modelling

α-and β-tubulin model of *Tetrahymena* (Uniprot sequence α: P41351, β: P41352) was constructed by homology modeling in Modeller v9.19 [48] using multiple models: 1TUB, 4U3J, 1TVK, 3JAR and 5SYF as templates and for restraints generation for atomic refinement. The restraints were generated in ProSmart [49] and the refinement was conducted iteratively until convergence in Refmac5 [50]. The model was validated using comprehensive validation for cryo-EM in Phenix v1.14 [51].

In order to model Rib43a-S, the candidate density in the ribbon region was traced in Coot v0.8.9.1 [52] and found to have approximately the same length as the “RIB43A protein” (Uniprot code: A4VDZ5). The secondary and tertiary structure prediction of Rib43a-S, using JPred v4 [53] and I-TASSER [54] respectively, were analyzed and confirmed to correspond to the secondary structure regions of the density map: an α-helical region and a coiled region. In order to find the correct amino acid registry, the main bulky residues of the sequence were fitted in the map in both directions of the C- and N- termini and the fit of the rest of the sequence was inspected. The final

model agrees perfectly with the predicted coiled N-terminus and α-helical C-terminus with amino acid side chains that conform perfectly to the density signature in the highlighted ribbon region.

The same methodology was followed for building Rib43a-L. Both models were refined and validated in Refmac5 and Phenix respectively as described for the *Tetrahymena* α-β tubulin model.

Intra and inter-dimer distance measurement

The α- and β-tubulin could be clearly distinguished in the maps using the S9-S10 loop (Figure 3.11.2A-C). We docked in the atomic models of the α- and β-tubulins in the map separately. The intra-dimer distance was measured as the distance between the N9 of GTP in the α-tubulin and GDP in the β-tubulin of the same tubulin dimer in Chimera. The inter-dimer distance was measured between N9 of GDP of the α-tubulin and GDP in the β-tubulin in the next tubulin dimer. The dimer distance was calculated as a sum of the intra- and inter-dimer distances.

PF pair rotation angle (lateral curvature) measurement

The lateral curvature can be represented by the lateral rotation angle between each PF pair. The rotation angles and Z-shift between PF pairs were measured using the 'measure' command from UCSF Chimera [55] according to Ichikawa *et al*., [5].

Secondary structure prediction

Secondary structure prediction of Rib43a-S and Rib43a-L was done using JPRED4 prediction server [53].

Coarse-grained molecular dynamic (MD) simulation

Based on the atomic structures of the three tubulin dimers and Rib43a-S, coarse-grained MD simulation was performed. Since we were able to model almost the entire region of Rib43a-S, this isoform was used for the simulation. In the coarse-grained model, each amino acid was represented as a single bead located at its C position as shown in Figure 3.11.3K. For observing dynamics, we used the energy function AICG2+ [56, 57]. In the AICG2+, the original reference structure was assumed as the most stable structure, and parameters could be modified to represent the interactions in the reference structure. We performed coarse grain MD on three tubulin dimers with and without Rib43a. Four residues (T382, K401, E415 and E433) from the α-tubulin at the minus end side (chain α0 in Figure 3.11.3K) were anchored for convenience of the analysis. It is known that the intra-dimer interaction is much stronger than the inter-dimer interaction. To

replicate this feature in our simulation, we set inter-dimer's non-local native interacting force to 0.1 times of the original value while that of intra-dimer was left as the original value (1.0 times of the original value). Then, we performed the simulation 30 times with and without Rib43a-S using the CafeMol package version 2.1 [58]. Each MD simulation took 107 MD steps with one MD step roughly corresponding to ~1 ps. The MD simulations were conducted by the underdamped Langevin dynamics at a temperature of 300 K. We set the friction coefficient to 0.02 (CafeMol unit), and default values in CafeMol were used for other parameters.

Visualization

The maps and models were segmented, coloured and visualized using Chimera [55] and ChimeraX [59].

Data availability

The dataset analysed and raw data of the measurements are available from the corresponding author upon fair request.

3.9 Author Contributions

KHB and MI designed the experiments and MI performed cell culture, purification, vitrification of cryo grids. MI and KB performed cryo-EM data acquisition. MI, AAZK and KHB performed EM data processing with helps from DD and MAFM. JV did the local restoration and sharpening. AAZK performed modelling. SK performed molecular dynamics. MI, AAZK, SK, DD and KHB interpreted the data and wrote the manuscript.

3.10 Figures

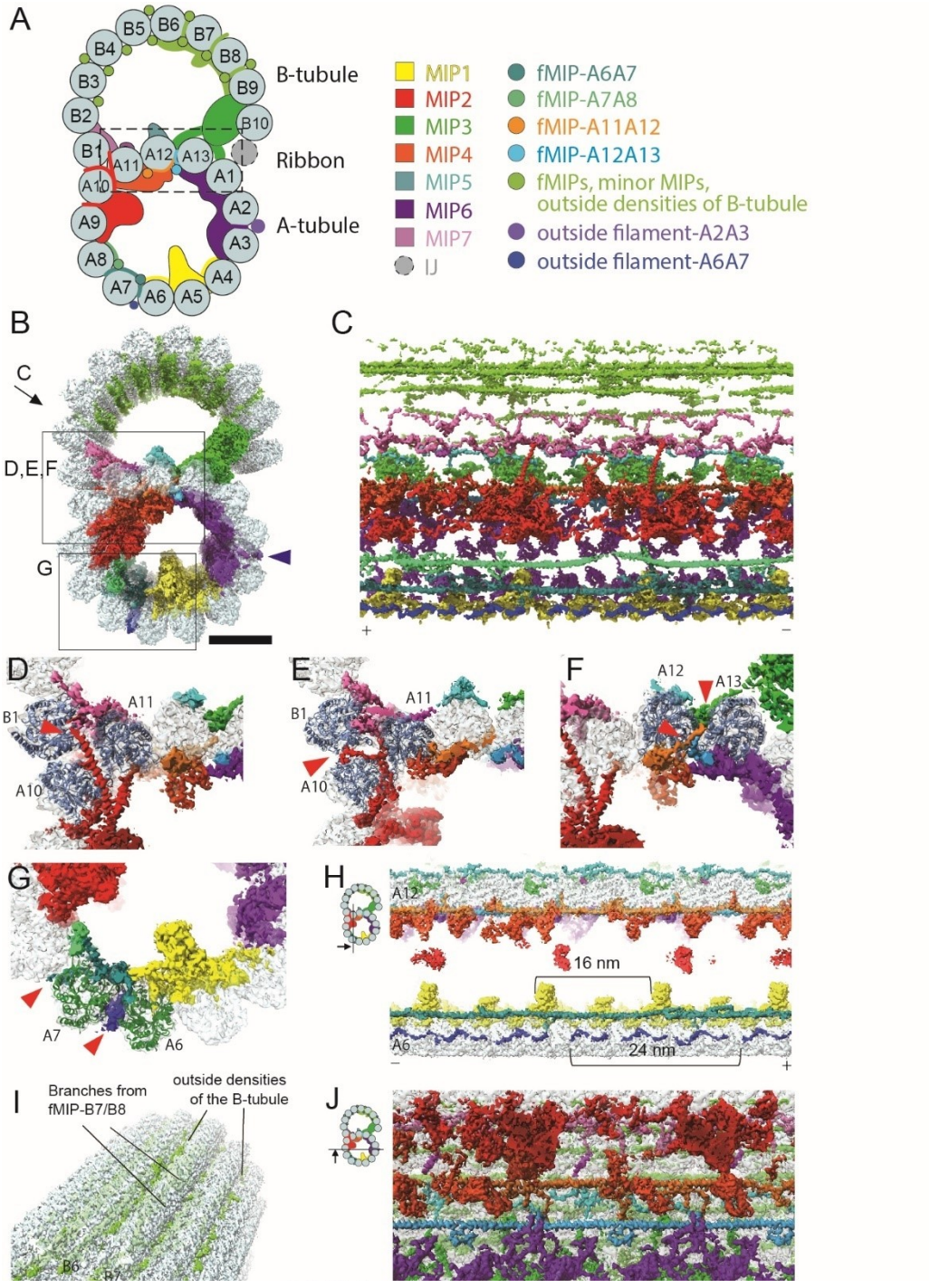

Figure 3.10.1 Network of the MIPs are woven into the tubulin lattice.

(A) Schematic cartoon of the doublet from *Tetrahymena* viewed from the tip of the cilia. PF numbers are shown, and MIPs are colored as the right panel. The PF ribbon region is indicated as

the dashed box. The inner junction (IJ), not presented in our structure, is known to bridge the B- and A-tubules [60]. (B) Surface rendering of the 48-nm unit of the doublet is colored according to (A). Blue arrowhead indicates the outside filament-A2A3/the outside molecular ruler [19]. Scale bar, 10 nm. Views of (C-G) are indicated in (B). (C) The weaving network of MIPs inside the tubulin lattice with tubulin densities removed. Plus and minus ends are indicated by (+) and (-) signs, which will be consistent throughout. (D-G) Insertions of the MIPs into the tubulin lattice. Red arrowheads indicate the insertion densities. (D) α-helical branches from the MIP2 go in-between PFs A10 and A11. (E) A branch of MIP2 (red arrowhead) goes in-between PF pairs-A10/A11 and A10/B1, reaching outside the tubulin lattice. (E) and (D) are both cross-sections with a different depth along the longitudinal axis of the doublet. (F) Branches from fMIPs-A11A12 and A12A13 (red arrowheads) go in-between the tubulin lattice. (G) Branches from fMIP-A6A7 reach the outside surface and contact densities outside (red arrowheads). (H) Sectional view showing the outside filament-A6A7 (blue). Outside filament-A6A7 appears as a 24-nm repeating unit. (I) Outside densities of B-tubules. (J) fMIPs appear as single α-helical structures running in-between the inner ridges of the PF pairs-A11/A12 and A12/A13. The globular MIPs and fMIPs are connected by branches.

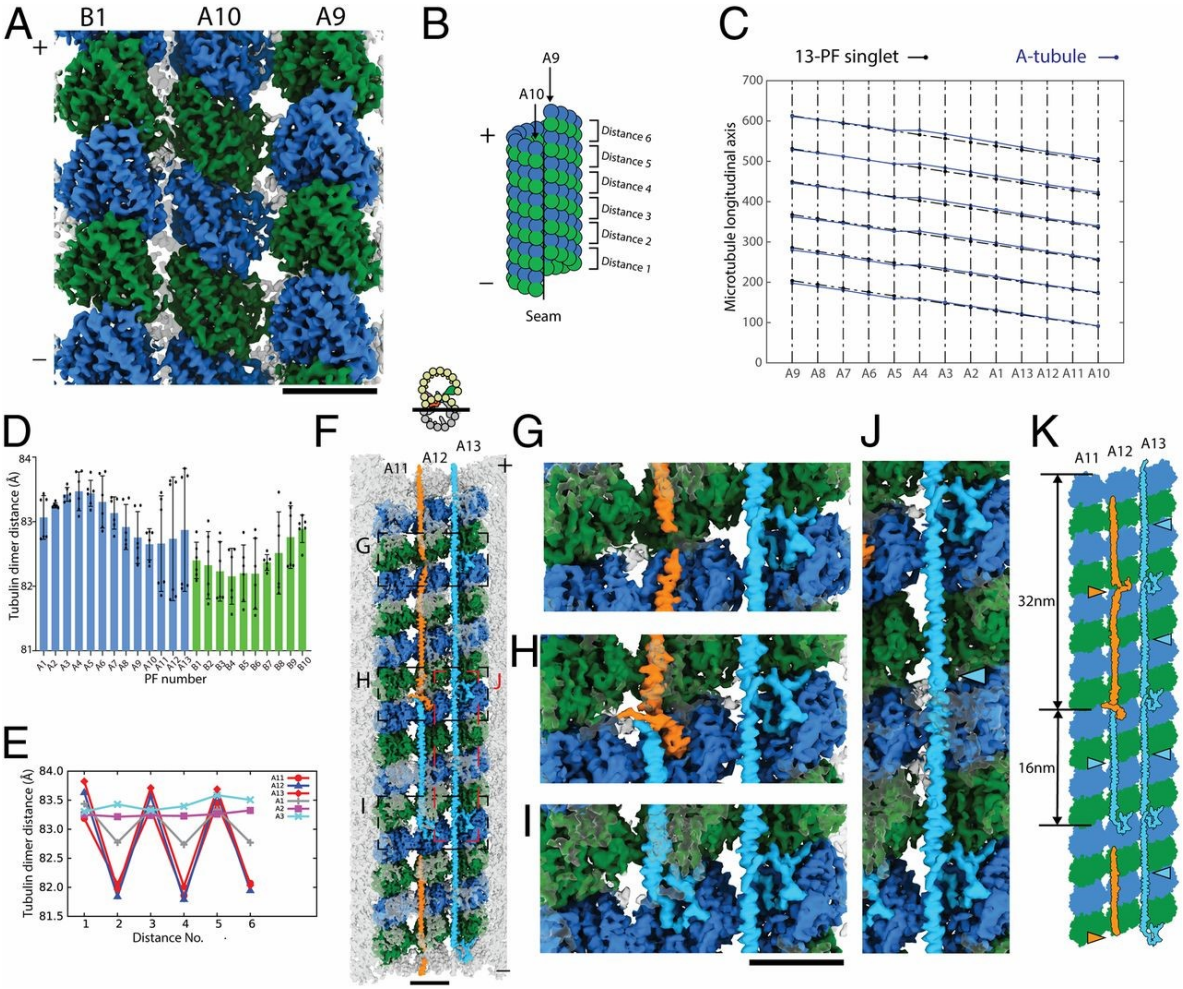

Figure 3.10.2 The complex tubulin lattice within the 48-nm repeating unit of the doublet.

(A) Outside view of surface rendering of the doublet at PFs A9, A10 and B1. α- and β-tubulins are colored as green and blue. (B) Schematic diagram of the A-tubule and the tubulin dimer distance measurement. (C) Two-dimensional plot of the tubulin lattice of the A-tubule of the doublet (blue) and the 13-PF singlet (black) [29]. The tubulin lattice is cut and unfurled at the seam as in (B). Despite having the same 13-3 B-lattice as the 13-PF singlet, the A-tubule of the doublet shows a non-uniform tubulin dimer distance and Z-shift. (D) Plot of the dimer distance measurements among PFs in the doublet. For each PF, six dimer distances within the 48nm repeating unit (illustrated in B) were measured and plotted as dots. Mean value (bar) with standard deviation (error bar) for each PF are shown. (E) Bimodal pattern of the tubulin dimer distances. The dimer distances from PFs-A11 to A13, and A1 to A3 of the doublet were plotted in the same longitudinal order as in the 48-nm unit. The dimer distances of PF A11 to A1 oscillate with every

two tubulin units (~16 nm). (F) Luminal view of the PF ribbon region A11-A13. fMIP densities in the A11-A13 region are now colored based on its tracing and morphology. The short 16-nm filament density is colored in light blue while the longer filament density is colored in orange. Tubulins in PFs A11-A13 are colored while all other densities are transparent. Magnified views of (G-J) are indicated by a dashed box in (F). (K) A schematic diagram of the filament density identified in the PF ribbon region. Per 48-nm, there are three short filaments between PFs A12 and A13 (light blue arrowheads) and there are one short filament (light blue arrowheads) and one longer filament (orange arrowhead) between PFs A11 and A12.

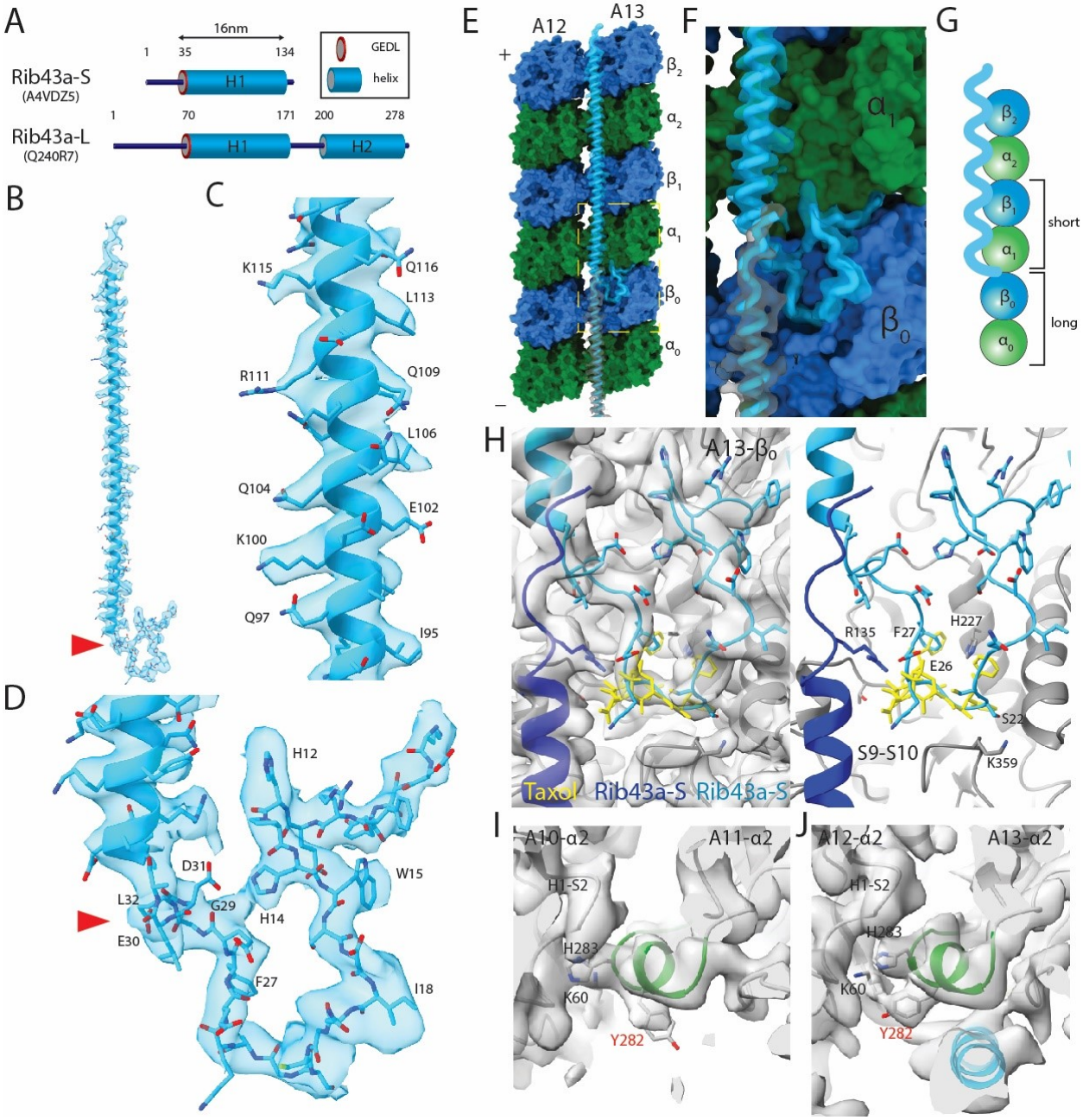

Figure 3.10.3 Rib43a leads to the bimodal distance in the PF regions.

(A) Secondary structure prediction of Rib43a-S and Rib43a-L. Only the large stretch of α-helices more than 20 residues from the structure prediction is shown. The GEDL consensus sequence is a conserved region of Rib43a (PFAM PF05914). (B) Model of the Rib43a-S inside its segmented density. (C-D) Magnified views of the helical region (C) and the N-terminal region (D) of Rib43a-S. The location of the GEDL motif is shown by the red arrowheads in (B) and (D). (E) Model of

Rib43a binds to the PF pair A12/A13. Yellow-dashed box shows the magnified view in (F). (F) The N-terminus of Rib43a-S inserts into the inter-dimer interface in PF A13. (G) Schematic model of how Rib43a-S binds to the PF leading to the bimodal dimer distance pattern. (H) Superimposed views of taxol (PDB: 5SYF, yellow) and Rib43a-S with map (left panel) and without map (right panel) show similar topology. R135 in the C-terminus of the lower Rib43a-S (dark blue) might interact with E26 of the N-terminus of the upper Rib43a-S (light blue) in a head-to-tail dimerization mechanism. (I) and (J) M-loop conformations in the lateral interaction with Rib43a (PFs A12 and A13) and without (PFs A10 and A11). The side chain of Y282 adopts a different conformation in the presence of Rib43a, potentially due to steric clash. In this conformation, Y282 might interact with K60 of the neighbouring α-tubulin.

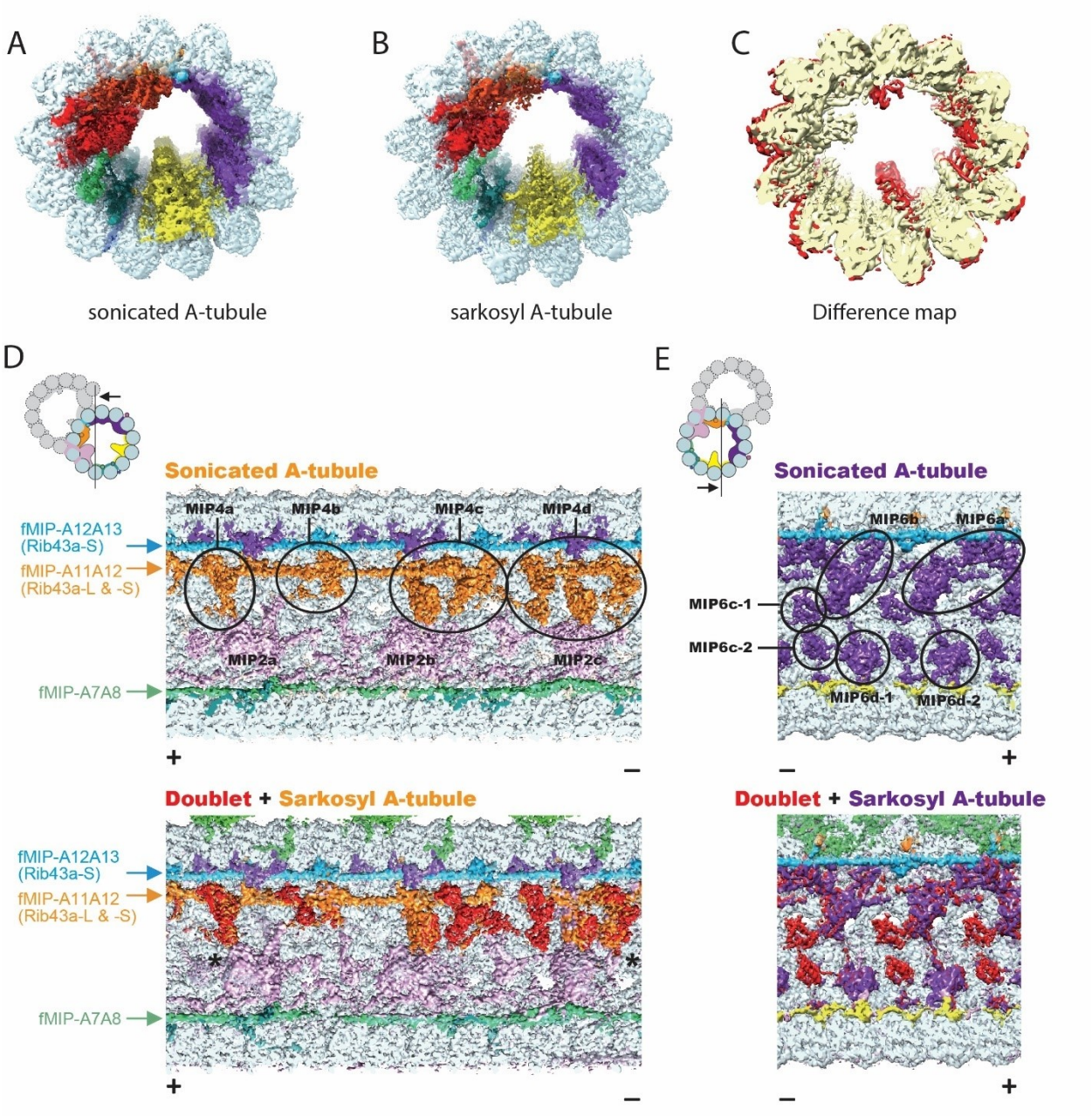

Figure 3.10.4 Sarkosyl treatment removes some MIPs from the doublet.

(A and B) Surface renderings of the sonicated A-tubule (A) and sarkosyl A-tubule (B) maps. (C) Difference map between the sonicated and sarkosyl A-tubule maps. Superimposition of the two maps reveals the missing MIP densities in the sarkosyl A-tubule map (red regions). Parts of the MIP2 and MIP6 are missing in sarkosyl A-tubule map. (D and E) Sonicated A-tubule map (top) and the overlap of doublet and sarkosyl A-tubule maps (bottom). The MIP4 and MIP6 regions of

the doublet (red) are mapped onto corresponding regions from sarkosyl A-tubule map (MIP4 in orange and MIP6 in purple). The views are indicated in the illustrations on the top left. Remaining fMIPs are indicated on the side. The coloring of MIP2 and MIP4 is different from other figures to avoid confusion (see the illustration for the coloring). Some densities at the MIP4 and MIP6 regions are missing after the sarkosyl treatment while the fMIPs appear intact. The slight shifts in MIP4a (indicated by asterisks) at both + and - end are due to lateral compaction of the tubulin lattice.

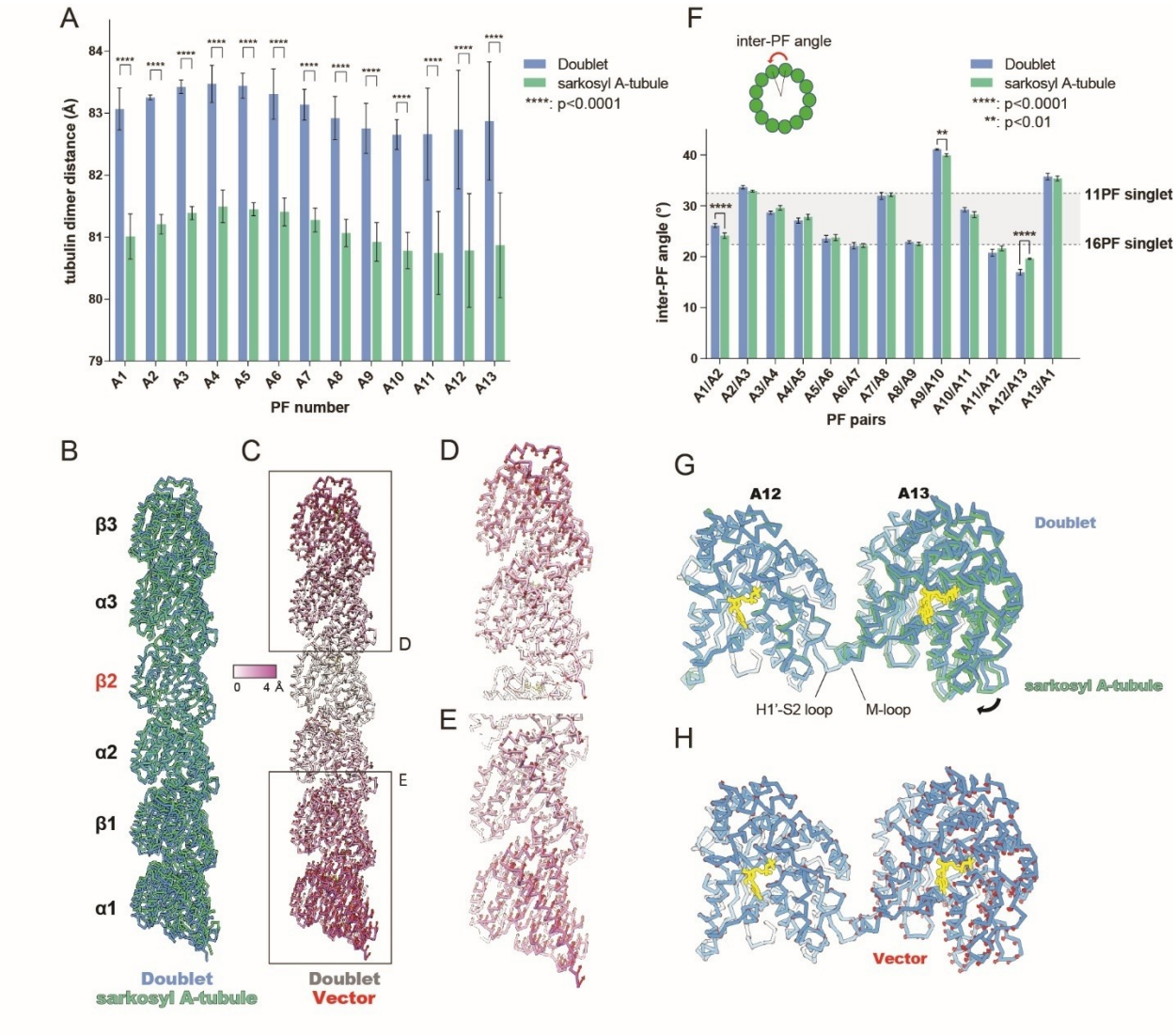

Figure 3.10.5 Longitudinal tubulin lattice length and curvature are regulated by the MIPs.

(A) Plot of tubulin dimer distances from doublet and the sarkosyl A-tubule. Mean values with standard deviation for each PF are shown. The average value of each PF from sarkosyl A-tubule shows a lateral compression of ~2 Å. Statistical analysis was performed by two-way ANOVA, Bonferroni post hoc test (see also Table S2). (B) Comparison of tubulin models refined in PF-A12 from doublet (blue) and sarkosyl A-tubule (green) showing a longitudinal compaction after missing some MIPs. Models were aligned by β2-tubulin. (C) Tubulin models of PF-A12 from the doublet are colored according to the degree of displacement. Vectors of the Cα displacement toward the sarkosyl A-tubule model are shown in red. (D and E) Close-up views of the tubulins from the periphery with vectors. (F) Plot of inter-PF-angles in the doublet and sarkosyl A-tubule.

Inter-PF angles were measured as shown in the schematic diagram on top and mean values were plotted (see also Figure 3.11.5C and Table S3). Error bars represent standard deviation. Two-way ANOVA, Bonferroni post hoc test was performed to compare the mean values. PF pairs with *p*-values smaller than 0.01 are highlighted by asterisks (see also Table S4). The gray area in the plot represents the PF pair angles commonly seen for *in vitro* reconstituted singlets [29]. (G) Alignment of the models of PF pair-A12/A13 from the doublet (blue) and sarkosyl A-tubule (green) based on the tubulin unit of PF-A12 reveals ~3° difference in rotation (black arrow). (H) The model of PFs-A12/A13 from the doublet with the vectors (red) of the displacement of Cα compared to the sarkosyl A-tubule model. Nucleotides: yellow.

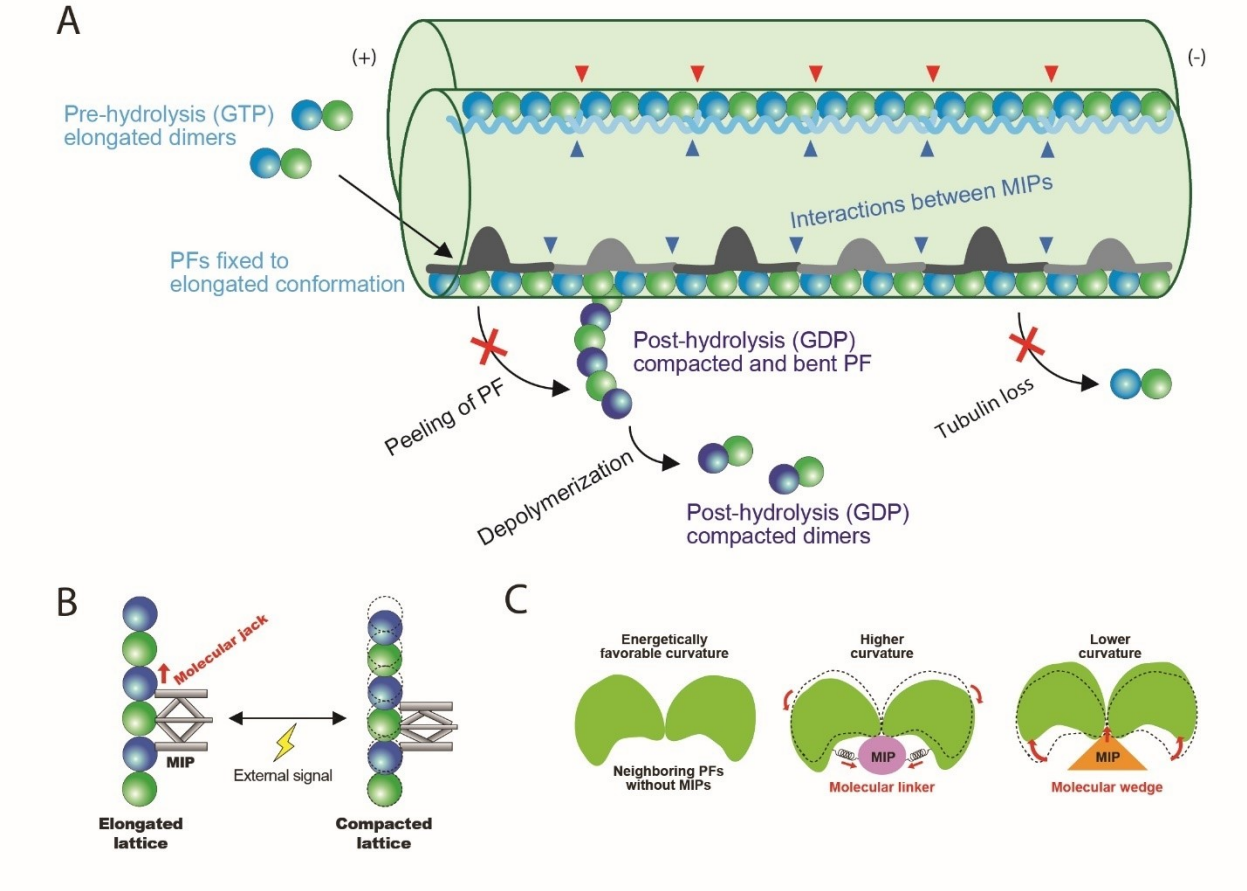

Figure 3.10.6 Model of stabilization mechanisms of the doublet tubulin lattice by MIPs.

(A) Model of the impacts of the MIPs on the doublet. First, elongated tubulin dimers in GTP pre-hydrolysis state are incorporated into the tubulin lattice. This elongated and stable conformation is fixed after assembly into the lattice through the interactions with the MIPs. The network of MIPs (blue arrowheads) also holds the tubulin lattice from the inside to prevent the loss of tubulin or breakage. At the plus end, MIPs prevent the peeling of PFs and depolymerization by keeping PFs in a stable and elongated conformation. Hence, the doublet is stabilized by the MIPs at several different levels to ensure that it can withstand the mechanical stress and prevent catastrophic events for the cilia. Some MIPs, such as Rib43a, have insertions into the tubulin lattice (red arrowheads), causing the larger inter-dimer gap and bimodal dimer distance. (B) Schematic diagram of the function of the MIPs in regulating tubulin lattice length. Some MIPs work as a molecular jack to keep the tubulin lattice elongated. External signals could change the MIP property and thereby the tubulin lattice. (C) MIPs regulate the angles between PFs. Without MIPs, tubulin lattice takes an energetically favorable curvature. Some MIPs work as molecular binders, which hold adjacent

tubulin pairs together so that it will take a higher curvature such as in the PFs A9/A10. Other MIPs, in particular, Rib43a work as molecular wedges and open the PF pairs and induce a lower curvature.

3.11 Supplementary materials

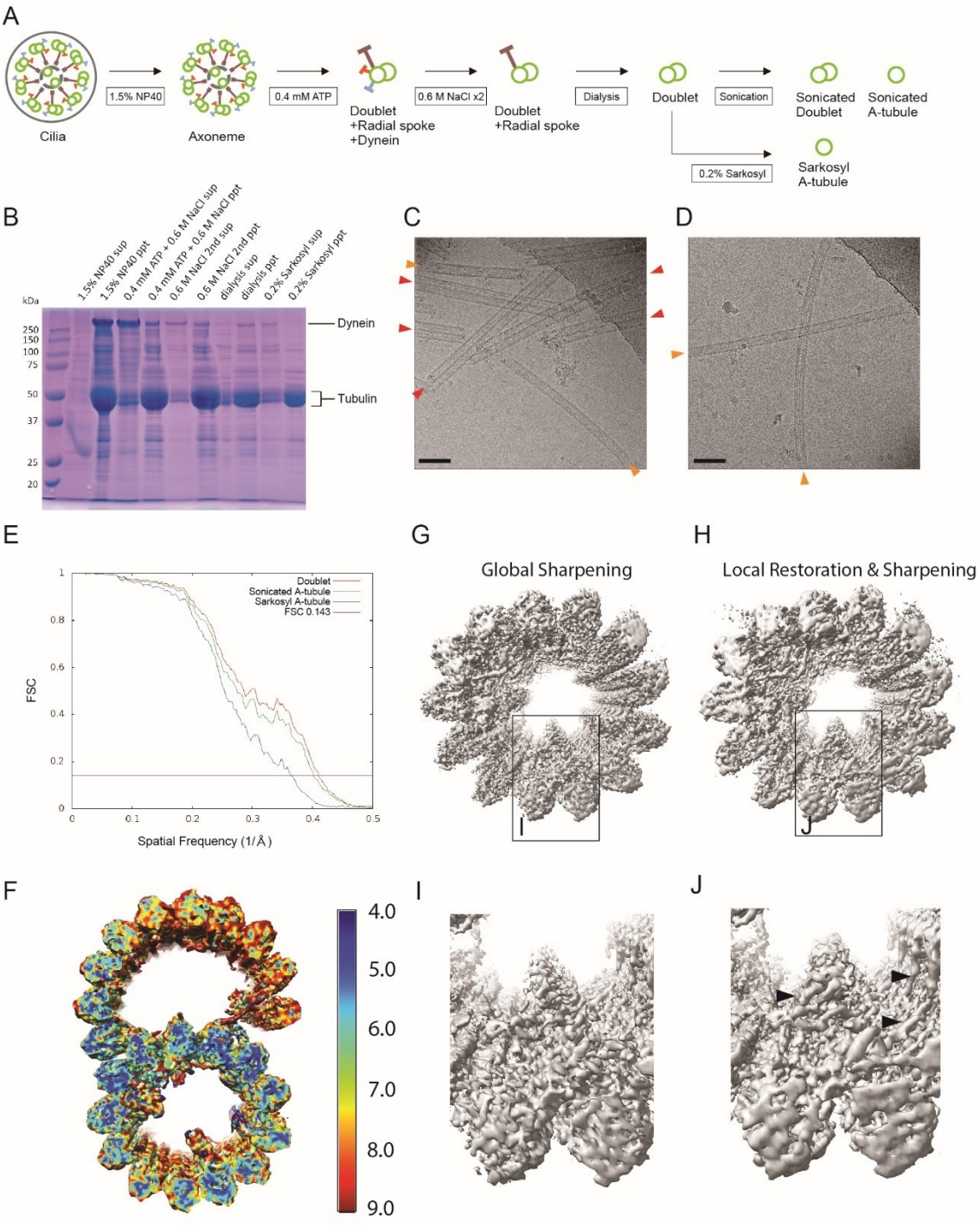

Figure 3.11.1 Data related to doublet microtubule structure.

(A) Schematics of fractionation of the axoneme in this study. Doublets were split from axoneme, and outside proteins were removed to obtain a simpler sample for cryo-EM. A-tubules were obtained by either sonication or sarkosyl treatment. (B) SDS-PAGE gel of the fractionated axoneme. From the gel, the sarkosyl-treated fraction was less complex than the doublet fraction consistent with the missing densities in the EM result. (C) A typical cryo-EM image of the doublet fraction shows both doublets (red arrowheads) and A-tubules (orange arrowheads) due to the sonication process. (D) A representative cryo-EM image of the sarkosyl-treated fraction shows the A-tubules (orange arrowheads). Scale bars in (C and D), 100 nm. (E) Gold-standard Fourier Shell Correlation of the doublet, sonicated and sarkosyl A-tubule maps. (F) Local resolution estimation of the doublet using MonoRes. The A-tubule, in general, has good resolution while the resolution of the B-tubule is lower due to the flexibility without the inner junction. (G) and (H) The sarkosyl A-tubule sharpened globally by Relion and locally by local restoration and sharpening. The magnified views of the structures are shown in (I) and (J). It is clearly shown that local restoration and sharpening improved connectivity in the structure.

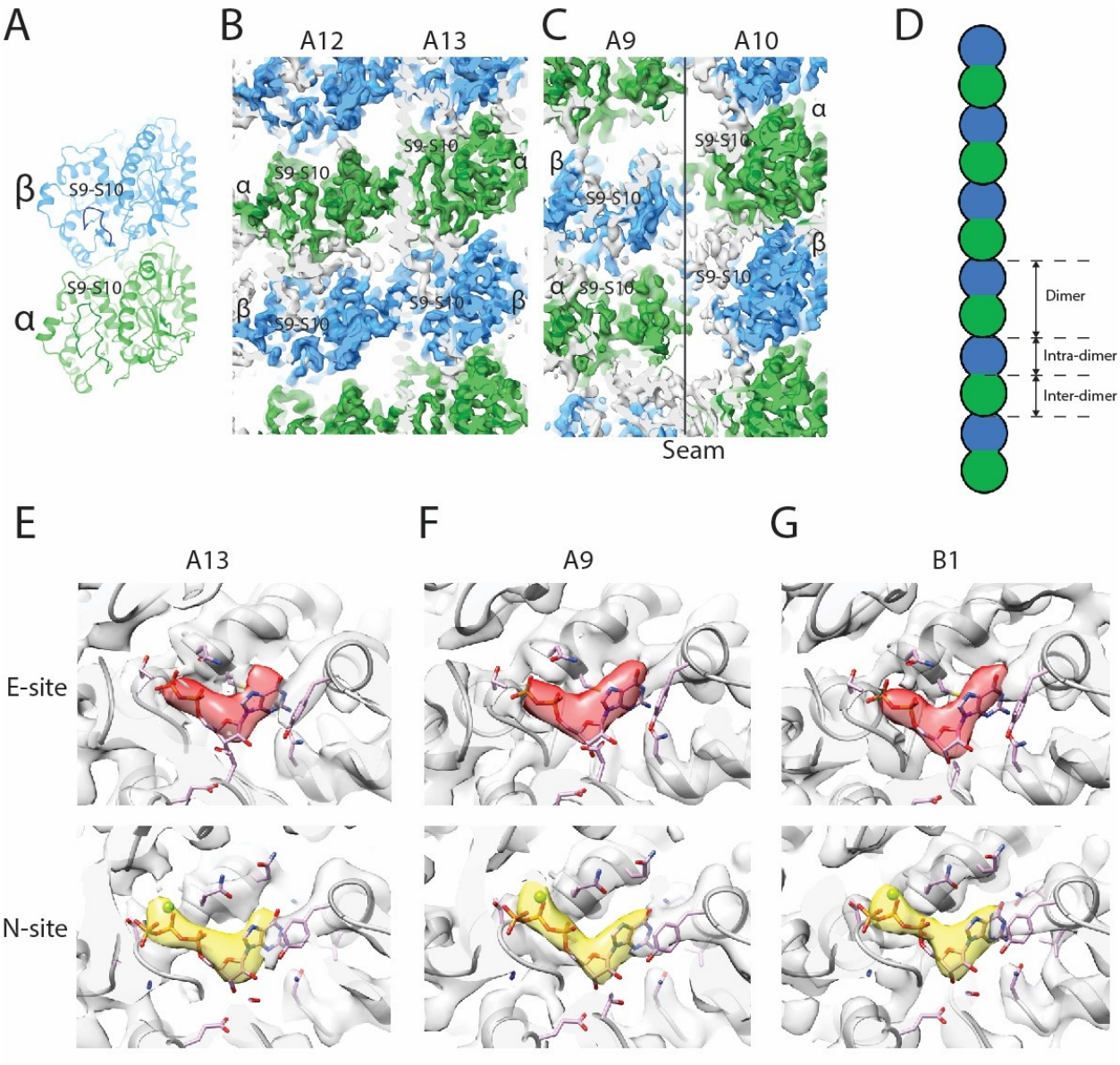

Figure 3.11.2 Determination of α- and β-tubulins and nucleotide states in the doublet.

(A) A view of tubulin model shows the clear difference between the loop S9-S10 of α- and β-tubulins. S9-S10 loop of β-tubulin is much shorter than that of α-tubulin. Luminal views of α- and β-tubulins in PF A12 and A13 (B), and PF A9 and A10 (C) show clear visualization of the S9-S10 loop and also identify the seam between A9 and A10. (D) A schematic of how we measured the dimer distance. (F-H) Nucleotide densities in tubulins. Densities corresponding to GTP are observed in α-tubulins of PF A13 (F), A9 (G) and B1 (H) while densities corresponding to GDP are observed in β-tubulins of PF A13 (F), A9 (G) and B1 (H).

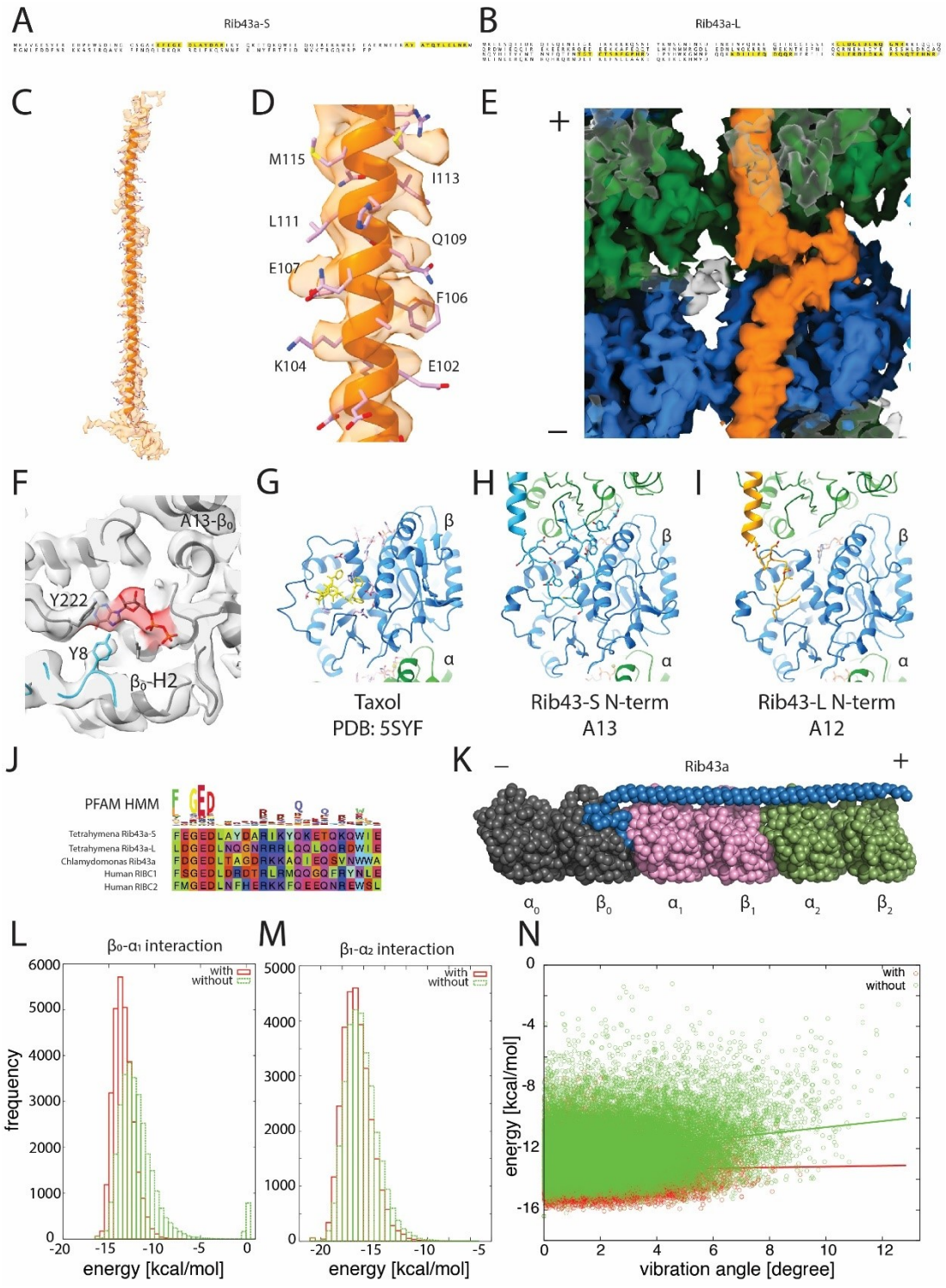

Figure 3.11.3 Data related to Rib43a-S and Rib43a-L.

(A-B) Peptide coverage of Rib43a-S (A) and Rib43a-L (B) from the mass spectrometry of sarkosyl A-tubule. (C) Model of amino acids 60-172 of Rib43a-L inside its segmented density. (D) A close-up of the H1 region of Rib43a-L. (E) The junction region of Rib43a-L is connected using a lower threshold of 0.019. In comparison, the threshold used for the junction region of Rib43a-L in Figure 3.10.3G is 0.04. (F) Residue Y8 from Rib43a-S could interact with GDP from β-tubulin, similar to Y222 of β-tubulin. (G-I) Models of taxol (PDB: 5SYF) (G), N-terminus of Rib43a-S (H) and N-terminus of Rib43a-L (I) bind to β-tubulin. (J) Sequence alignment and Hidden Markov Model [61] of Rib43a from *Tetrahymena*, *Chlamydomonas* and human. (K) Overview of the MD simulation setup. Model of three tubulin dimers (each chain is named as α_0, β_0, α_1, β_1, α_2 and β_2) were analyzed by MD simulation with or without Rib43a-S model. (L-M) Histogram of energy between β_0 and α_1 (L) and between β_1 and α_2 (M) obtained from 30 coarse-grained MD simulations with (red box) and without (green box) Rib43a-S. With Rib43a bound, the energy between β-tubulin of the first dimer and α-tubulin of the second dimer is lower, meaning that the structure is more stable with Rib43a-S. There is an insignificant difference in energy between β_1 and α_2, suggesting that the N-terminus has a stronger effect in stabilizing the tubulin lattice. (N) The correlation of the energy between β_0 and α_1 and the bending angle of the filament from the 30 coarse-grained MD simulations with (red dot) and without (green dot) Rib43a-S. Each of the two straight lines (red and green) is a fitted line between the energy and the angle with and without Rib43a-S by the least-square method ($y = 0.0279x - 13.5$ and $y = 0.199x - 12.6$, respectively). Without Rib43a, tubulins become less stable (higher energy) as the tubulin lattice bends (larger vibration angle). In contrast, when Rib43a is bound, tubulins stay in a rather consistent energy state even with more bending.

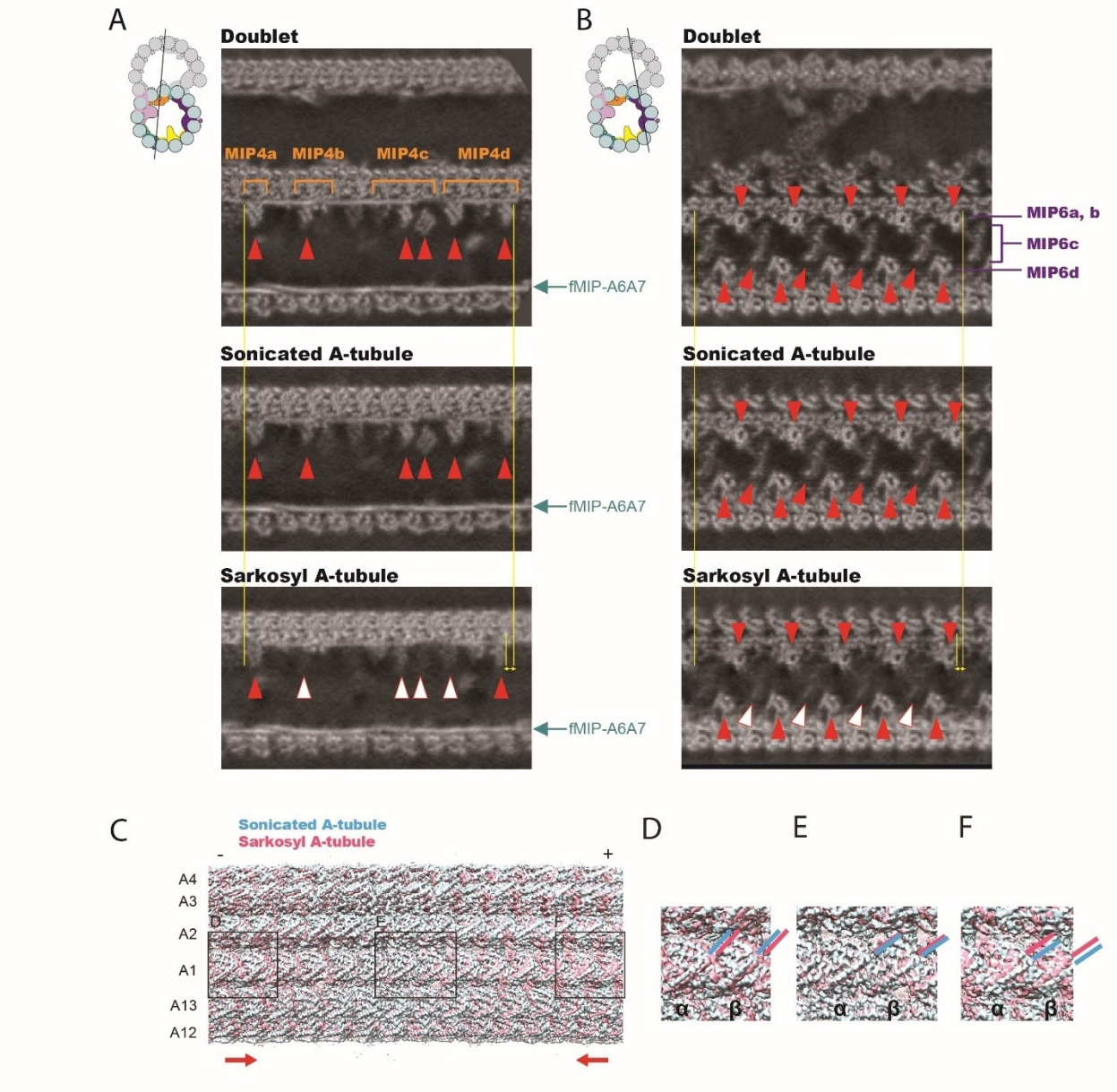

Figure 3.11.4 Comparison of MIPs from the doublet, sonicated A-tubule and sarkosyl A-tubule maps.

(A and B) Slices through the maps of the doublet, sonicated A-tubule and sarkosyl A-tubule. Black lines in the schematics indicate the locations of the slices. MIP4 and MIP6 densities are preserved in the sonicated A-tubule structure as shown by red arrowheads. Missing parts of these MIPs in the sarkosyl A-tubule map are indicated by empty arrowheads. fMIP-A6A7 densities are shown by arrows in (A). Yellow lines and double-headed arrows show the shifts of the MIPs in the longitudinal direction due to compaction of the tubulin lattice in sarkosyl A-tubule. (C-F)

Comparison of the density maps of sonicated and sarkosyl A-tubules. In the middle part, tubulins fit well to the density map as in (E). On the other hand, as it gets closer to both ends, tubulin densities from sarkosyl A-tubule map appear shifted toward the middle (D and F), which means that sarkosyl A-tubule tubulin lattice is shorter than that of sonicated A-tubule. Red arrows indicate the tubulin shift directions from both + and - ends. Locations of helix H12 of tubulin are indicated by pink or blue lines.

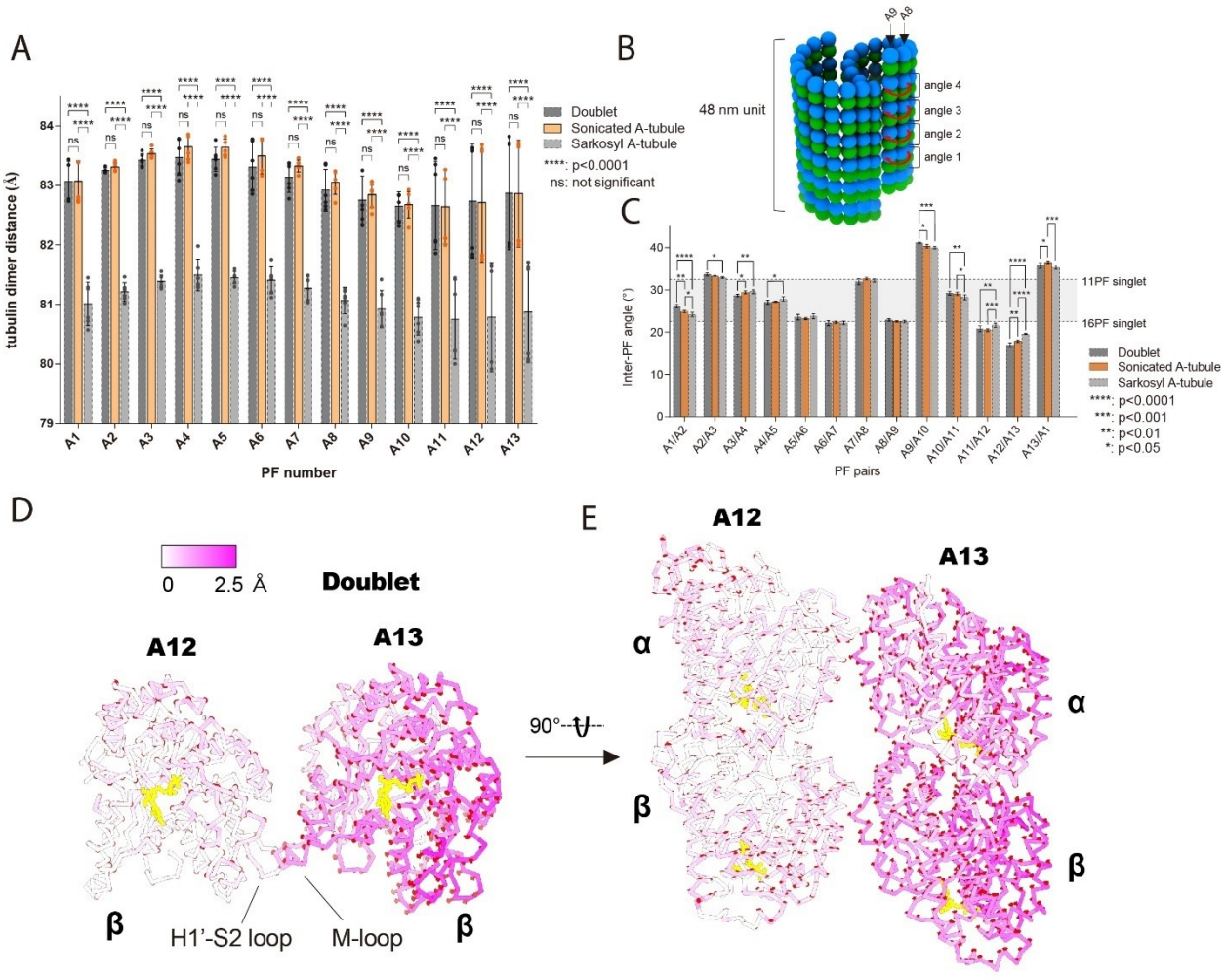

Figure 3.11.5 Data related to longitudinal tubulin dimer distance.

(A) Plot of tubulin dimer distances from the sonicated A-tubule map. Values of the A-tubule from the doublet and sarkosyl A-tubule maps from Figure 3.10.5A are shown in gray for comparison. For statistical analysis, two-way ANOVA followed by Tukey's multiple comparison test was performed. For all PFs, changes between the doublet and sonicated A-tubule are not significant ($p > 0.01$). The sonicated A-tubule also shows a bimodal distribution in the PF ribbon region. (B) Schematic of PF angle measurements. Angles were measured using four tubulin pairs from each PF pair in the 48-nm unit as indicated by red arrows. PF pair-A8/A9 is shown as an example. (C) Plot of inter-PF angles from sonicated A-tubule map. Values of the doublet and sarkosyl A-tubule from Figure 3.10.5F are shown in gray for comparison. Two-way ANOVA followed by Tukey's multiple comparison test was performed for statistical analysis. Curvatures of PFs A5-A9, where

MIPs are preserved are the least affected. (D and E) Comparison of PF pair-A12/A13 models from doublet and sarkosyl A-tubule. View in (D) is the same as Figure 3.10.5G. The models are aligned by the tubulin dimer in PF-A12. The display model is from the PF pair-A12/A13 of the doublet and colored based on the displacement of Cα. The displacement vectors from the doublet to the sarkosyl A-tubule are shown in red. The displacement vectors clearly show the rotation of the tubulin dimer in A13 in the sarkosyl A-tubule. Yellow, nucleotides.

Table S1. Tubulin dimer distances of the A-tubule lattice.

	Dimer distances (intra- / inter-dimer distances) from doublet (Å) (mean ± SD, n = 6)	Dimer distances (intra- / inter-dimer distances) from sonicated A-tubule (Å) (mean ± SD, n = 6)	Dimer distances (intra- / inter-dimer distances) from sarkosyl A-tubule (Å) (mean ± SD, n = 6)
A1	83.1 ± 0.309 (41.8 ± 0.0352 / 41.3 ± 0.299)	83.1 ± 0.313 (41.8 ± 0.222 / 41.3 ± 0.300)	81.0 ± 0.333 (41.1 ± 0.106 / 39.9 ± 0.253)
A2	83.3 ± 0.0354 (41.7 ± 0.0507 / 41.5 ± 0.0636)	83.3 ± 0.0672 (41.8 ± 0.0474 / 41.6 ± 0.0796)	81.2 ± 0.143 (41.0 ± 0.0868 / 40.2 ± 0.0929)
A3	83.4 ± 0.0988 (41.8 ± 0.0242 / 41.6 ± 0.0975)	83.5 ± 0.0696 (41.8 ± 0.0351 / 41.7 ± 0.0549)	81.4 ± 0.0965 (40.8 ± 0.0455 / 40.6 ± 0.0965)
A4	83.5 ± 0.274 (41.8 ± 0.0460 / 41.6 ± 0.255)	83.6 ± 0.195 (41.8 ± 0.0457 / 41.8 ± 0.191)	81.5 ± 0.242 (40.8 ± 0.0511 / 40.7 ± 0.215)
A5	83.4 ± 0.184 (41.9 ± 0.0414 / 41.6 ± 0.199)	83.6 ± 0.127 (41.9 ± 0.0344 / 41.8 ± 0.154)	81.4 ± 0.0944 (40.7 ± 0.118 / 40.7 ± 0.198)
A6	83.3 ± 0.369 (41.8 ± 0.0730 / 41.5 ± 0.345)	83.5 ± 0.271 (41.8 ± 0.0586 / 41.7 ± 0.224)	81.4 ± 0.206 (41.0 ± 0.112 / 40.4 ± 0.216)
A7	83.1 ± 0.228 (41.7 ± 0.0762 / 41.4 ± 0.192)	83.3 ± 0.0896 (41.8 ± 0.558 / 41.5 ± 0.102)	81.3 ± 0.175 (41.0 ± 0.0914 / 40.3 ± 0.109)
A8	82.9 ± 0.319 (41.7 ± 0.0786 / 41.2 ± 0.253)	83.0 ± 0.182 (41.7 ± 0.0337 / 41.3 ± 0.173)	81.1 ± 0.204 (40.8 ± 0.0403 / 40.2 ± 0.207)
A9	82.8 ± 0.367 (41.7 ± 0.0653 / 41.0 ± 0.337)	82.8 ± 0.198 (41.7 ± 0.0650 / 41.1 ± 0.239)	80.9 ± 0.285 (40.9 ± 0.138 / 40.1 ± 0.295)
A10	82.7 ± 0.221 (41.6 ± 0.0545 / 41.0 ± 0.218)	82.7 ± 0.202 (41.7 ± 0.0753 / 41.0 ± 0.226)	80.8 ± 0.268 (40.7 ± 0.104 / 40.1 ± 0.261)
A11	82.7 ± 0.676 (41.7 ± 0.0840 / 41.0 ± 0.649)	82.6 ± 0.575 (41.7 ± 0.0583 / 41.0 ± 0.593)	80.7 ± 0.610 (40.7 ± 0.0681 / 40.0 ± 0.590)
A12	82.7 ± 0.875 (41.6 ± 0.0900 / 41.1 ± 0.960)	82.7 ± 0.912 (41.7 ± 0.0462 / 41.0 ± 0.938)	80.8 ± 0.836 (40.7 ± 0.0542 / 40.1 ± 0.865)
A13	82.9 ± 0.870 (41.7 ± 0.0443 / 41.2 ± 0.908)	82.9 ± 0.820 (41.7 ± 0.0304 / 41.1 ± 0.836)	80.9 ± 0.772 (40.7 ± 0.0775 / 40.1 ± 0.833)
All*	83.1 ± 0.540 (41.7 ± 0.0937 / 41.3 ± 0.516)	83.1 ± 0.546 (41.8 ± 0.0810 / 41.4 ± 0.516)	81.1 ± 0.485 (40.8 ± 0.158 / 40.3 ± 0.483)

*For all PF results, mean values with SD calculated from all PFs (n = 78) are shown.

Table S2. Summary of Bonferroni's multiple comparisons test of tubulin dimer distances comparing doublet and sarkosyl A-tubule.

	Mean differences (Å)	95% confidence intervals of differences	Adjusted *p*-values
A1	2.056	1.255 to 2.857	< 0.00010
A2	2.043	1.243 to 2.844	< 0.00010
A3	2.036	1.235 to 2.837	< 0.00010
A4	1.977	1.176 to 2.778	< 0.00010
A5	1.992	1.191 to 2.793	< 0.00010
A6	1.901	1.100 to 2.702	< 0.00010
A7	1.861	1.060 to 2.662	< 0.00010
A8	1.853	1.052 to 2.653	< 0.00010
A9	1.834	1.033 to 2.635	< 0.00010
A10	1.87	1.069 to 2.671	< 0.00010
A11	1.915	1.114 to 2.716	< 0.00010
A12	1.95	1.149 to 2.751	< 0.00010
A13	2.005	1.204 to 2.806	< 0.00010

Table S3. Angles between PFs.

	Doublet (°) (mean ± SD, n = 4)	Sonicated A-tubule (°) (mean ± SD, n = 4)	sarkosyl A-tubule (°) (mean ± SD, n = 4)
A1/A2	26.1 ± 0.341	24.9 ± 0.231	24.2 ± 0.448
A2/A3	33.7 ± 0.303	33.3 ± 0.0913	32.9 ± 0.159
A3/A4	28.7 ± 0.273	29.4 ± 0.295	29.6 ± 0.410
A4/A5	27.1 ± 0.426	27.2 ± 0.125	27.8 ± 0.458
A5/A6	23.6 ± 0.571	23.2 ± 0.211	23.8 ± 0.505
A6/A7	22.2 ± 0.542	22.3 ± 0.245	22.2 ± 0.358
A7/A8	32.0 ± 0.596	32.6 ± 0.261	32.2 ± 0.304
A8/A9	22.9 ± 0.229	22.6 ± 0.115	22.5 ± 0.254
A9/A10	41.1 ± 0.122	40.3 ± 0.351	40.0 ± 0.243
A10/A11	29.2 ± 0.367	29.1 ± 0.336	28.3 ± 0.523
A11/A12	20.8 ± 0.577	20.5 ± 0.291	21.7 ± 0.393
A12/A13	16.9 ± 0.480	17.9 ± 0.241	19.6 ± 0.115
A13/A1	35.8 ± 0.542	36.5 ± 0.286	35.4 ± 0.414

Table S4. Summary of Bonferroni's multiple comparisons test of PF-pair angles comparing doublet and sarkosyl A-tubule.

	Mean differences (°)	95% confidence intervals of differences	Adjusted *p*-values
A1/A2	1.96	0.9693 to 2.951	< 0.00010
A2/A3	0.7659	-0.2249 to 1.757	0.3111
A3/A4	-0.9081	-1.899 to 0.08273	0.1015
A4/A5	-0.7241	-1.715 to 0.2667	0.422
A5/A6	-0.2226	-1.214 to 0.7682	> 0.9999
A6/A7	-0.06678	-1.058 to 0.9241	> 0.9999
A7/A8	-0.2326	-1.223 to 0.7582	> 0.9999
A8/A9	0.3308	-0.6600 to 1.322	> 0.9999
A9/A10	1.172	0.1816 to 2.163	0.0092
A10/A11	0.9591	-0.03173 to 1.950	0.0659
A11/A12	-0.8835	-1.874 to 0.1073	0.1243
A12/A13	-2.658	-3.649 to -1.667	< 0.00010
A13/A1	0.38	-0.6109 to 1.371	> 0.9999

Table S5. Tubulin dimer distances of the B-tubule from doublet.

	Dimer distances from doublet B-tubule (Å) (mean ± SD, n = 6)
B1	82.4 ± 0.258
B2	82.3 ± 0.476
B3	82.2 ± 0.422
B4	82.2 ± 0.395
B5	82.2 ± 0.401
B6	82.2 ± 0.502
B7	82.4 ± 0.111
B8	82.5 ± 0.581
B9	82.8 ± 0.443
B10	82.9 ± 0.195
All*	82.4 ± 0.468

*For all PF results, mean values with SD calculated from all PFs (n = 60) are shown.

3.12 References

1. Bui, K.H., et al., *Polarity and asymmetry in the arrangement of dynein and related structures in the Chlamydomonas axoneme.* J Cell Biol, 2012. **198**(5): p. 913-25.
2. Stepanek, L. and G. Pigino, *Microtubule doublets are double-track railways for intraflagellar transport trains.* Science, 2016. **352**(6286): p. 721-4.
3. Fliegauf, M., T. Benzing, and H. Omran, *When cilia go bad: cilia defects and ciliopathies.* Nat Rev Mol Cell Biol, 2007. **8**(11): p. 880-93.
4. Akhmanova, A. and M.O. Steinmetz, *Tracking the ends: a dynamic protein network controls the fate of microtubule tips.* Nat Rev Mol Cell Biol, 2008. **9**(4): p. 309-22.
5. Ichikawa, M., et al., *Subnanometre-resolution structure of the doublet microtubule reveals new classes of microtubule-associated proteins.* Nat Commun, 2017. **8**: p. 15035.
6. Pirner, M.A. and R.W. Linck, *Tektins are heterodimeric polymers in flagellar microtubules with axial periodicities matching the tubulin lattice.* J Biol Chem, 1994. **269**(50): p. 31800-6.
7. Norrander, J.M., et al., *The Rib43a protein is associated with forming the specialized protofilament ribbons of flagellar microtubules in Chlamydomonas.* Mol Biol Cell, 2000. **11**(1): p. 201-15.
8. Nicastro, D., et al., *The molecular architecture of axonemes revealed by cryoelectron tomography.* Science, 2006. **313**(5789): p. 944-8.
9. Nicastro, D., et al., *Cryo-electron tomography reveals conserved features of doublet microtubules in flagella.* Proc Natl Acad Sci U S A, 2011. **108**(42): p. E845-53.
10. Sui, H. and K.H. Downing, *Molecular architecture of axonemal microtubule doublets revealed by cryo-electron tomography.* Nature, 2006. **442**(7101): p. 475-8.
11. Pigino, G., et al., *Comparative structural analysis of eukaryotic flagella and cilia from Chlamydomonas, Tetrahymena, and sea urchins.* J Struct Biol, 2012. **178**(2): p. 199-206.
12. Stoddard, D., et al., *Tetrahymena RIB72A and RIB72B are microtubule inner proteins in the ciliary doublet microtubules.* Mol Biol Cell, 2018. **29**(21): p. 2566-2577.
13. Mikito Owa, T.U., Haruaki Yanagisawa, Takashi Yamano, Hiro Iguchi, Hideya Fukuzawa, Ken-ichi Wakabayashi, Toshio Ando, Masahide Kikkawa, *Inner lumen proteins stabilize doublet microtubules in cilia/flagella.* BioRvix, 2018.
14. Ichikawa, M. and K.H. Bui, *Microtubule Inner Proteins: A Meshwork of Luminal Proteins Stabilizing the Doublet Microtubule.* Bioessays, 2018. **40**(3).
15. King, S.M., *Axonemal protofilament ribbons, DM10 domains, and the link to juvenile myoclonic epilepsy.* Cell Motil Cytoskeleton, 2006. **63**(5): p. 245-53.
16. Ryan, R., et al., *Functional characterization of tektin-1 in motile cilia and evidence for TEKT1 as a new candidate gene for motile ciliopathies.* Hum Mol Genet, 2018. **27**(2): p. 266-282.
17. Ta-Shma, A., et al., *A human laterality disorder associated with a homozygous WDR16 deletion.* Eur J Hum Genet, 2015. **23**(9): p. 1262-5.
18. Kangkang Song, Z.S., Xiaofeng Fu, Xiaochu Lou, Nikolaus Grigorieff, Daniela Nicastro, *Structure of the ciliary axoneme at nanometer resolution reconstructed by TYGRESS.* BioRvix, 2018.
19. Oda, T., et al., *A molecular ruler determines the repeat length in eukaryotic cilia and flagella.* Science, 2014. **346**(6211): p. 857-60.
20. Linck, R.W., *Flagellar doublet microtubules: fractionation of minor components and alpha-tubulin from specific regions of the A-tubule.* J Cell Sci, 1976. **20**(2): p. 405-39.
21. Miki-Noumura, T. and R. Kamiya, *Conformational change in the outer doublet microtubules from sea urchin sperm flagella.* J Cell Biol, 1979. **81**(2): p. 355-60.
22. Alushin, G.M., et al., *High-resolution microtubule structures reveal the structural transitions in alphabeta-tubulin upon GTP hydrolysis.* Cell, 2014. **157**(5): p. 1117-29.

23. Zhang, R., et al., *Mechanistic Origin of Microtubule Dynamic Instability and Its Modulation by EB Proteins.* Cell, 2015. **162**(4): p. 849-59.
24. Manka, S.W. and C.A. Moores, *The role of tubulin-tubulin lattice contacts in the mechanism of microtubule dynamic instability.* Nat Struct Mol Biol, 2018. **25**(7): p. 607-615.
25. Zhang, R., B. LaFrance, and E. Nogales, *Separating the effects of nucleotide and EB binding on microtubule structure.* Proc Natl Acad Sci U S A, 2018. **115**(27): p. E6191-E6200.
26. Zhang, R., et al., *Structural insight into TPX2-stimulated microtubule assembly.* Elife, 2017. **6**.
27. Manka, S.W. and C.A. Moores, *Microtubule structure by cryo-EM: snapshots of dynamic instability.* Essays Biochem, 2018. **62**(6): p. 737-751.
28. Kellogg, E.H., et al., *Insights into the Distinct Mechanisms of Action of Taxane and Non-Taxane Microtubule Stabilizers from Cryo-EM Structures.* J Mol Biol, 2017. **429**(5): p. 633-646.
29. Sui, H. and K.H. Downing, *Structural basis of interprotofilament interaction and lateral deformation of microtubules.* Structure, 2010. **18**(8): p. 1022-31.
30. Schaedel, L., et al., *Microtubules self-repair in response to mechanical stress.* Nat Mater, 2015. **14**(11): p. 1156-63.
31. Schmidt-Cernohorska, M., et al., *Flagellar microtubule doublet assembly in vitro reveals a regulatory role of tubulin C-terminal tails.* Science, 2019. **363**(6424): p. 285-288.
32. Norrander, J.M., et al., *Structural comparison of tektins and evidence for their determination of complex spacings in flagellar microtubules.* J Mol Biol, 1996. **257**(2): p. 385-97.
33. Prota, A.E., et al., *Molecular mechanism of action of microtubule-stabilizing anticancer agents.* Science, 2013. **339**(6119): p. 587-90.
34. Kar, S., et al., *Repeat motifs of tau bind to the insides of microtubules in the absence of taxol.* EMBO J, 2003. **22**(1): p. 70-7.
35. Kellogg, E.H., et al., *Near-atomic model of microtubule-tau interactions.* Science, 2018. **360**(6394): p. 1242-1246.
36. Kirima, J. and K. Oiwa, *Flagellar-associated Protein FAP85 Is a Microtubule Inner Protein That Stabilizes Microtubules.* Cell Struct Funct, 2018. **43**(1): p. 1-14.
37. Lacey, S.E., et al., *Cryo-EM of dynein microtubule-binding domains shows how an axonemal dynein distorts the microtubule.* bioRxiv, 2019.
38. Witman, G.B., *Isolation of Chlamydomonas flagella and flagellar axonemes.* Methods Enzymol, 1986. **134**: p. 280-90.
39. Shevchenko, A., et al., *In-gel digestion for mass spectrometric characterization of proteins and proteomes.* Nat Protoc, 2006. **1**(6): p. 2856-60.
40. Zheng, S.Q., et al., *MotionCor2: anisotropic correction of beam-induced motion for improved cryo-electron microscopy.* Nat Methods, 2017. **14**(4): p. 331-332.
41. Zivanov, J., et al., *New tools for automated high-resolution cryo-EM structure determination in RELION-3.* Elife, 2018. **7**.
42. Zhang, K., *Gctf: Real-time CTF determination and correction.* J Struct Biol, 2016. **193**(1): p. 1-12.
43. Tang, G., et al., *EMAN2: an extensible image processing suite for electron microscopy.* J Struct Biol, 2007. **157**(1): p. 38-46.
44. Egelman, E.H., *The iterative helical real space reconstruction method: surmounting the problems posed by real polymers.* J Struct Biol, 2007. **157**(1): p. 83-94.
45. Frank, J., et al., *SPIDER and WEB: processing and visualization of images in 3D electron microscopy and related fields.* J Struct Biol, 1996. **116**(1): p. 190-9.
46. Grigorieff, N., *FREALIGN: high-resolution refinement of single particle structures.* J Struct Biol, 2007. **157**(1): p. 117-25.

47. Vilas, J.L., et al., *MonoRes: Automatic and Accurate Estimation of Local Resolution for Electron Microscopy Maps.* Structure, 2018. **26**(2): p. 337-344 e4.
48. Webb, B. and A. Sali, *Protein structure modeling with MODELLER.* Methods Mol Biol, 2014. **1137**: p. 1-15.
49. Nicholls, R.A., F. Long, and G.N. Murshudov, *Low-resolution refinement tools in REFMAC5.* Acta Crystallogr D Biol Crystallogr, 2012. **68**(Pt 4): p. 404-17.
50. Murshudov, G.N., et al., *REFMAC5 for the refinement of macromolecular crystal structures.* Acta Crystallogr D Biol Crystallogr, 2011. **67**(Pt 4): p. 355-67.
51. Adams, P.D., et al., *PHENIX: a comprehensive Python-based system for macromolecular structure solution.* Acta Crystallogr D Biol Crystallogr, 2010. **66**(Pt 2): p. 213-21.
52. Emsley, P., et al., *Features and development of Coot.* Acta Crystallogr D Biol Crystallogr, 2010. **66**(Pt 4): p. 486-501.
53. Drozdetskiy, A., et al., *JPred4: a protein secondary structure prediction server.* Nucleic Acids Res, 2015. **43**(W1): p. W389-94.
54. Yang, J., et al., *The I-TASSER Suite: protein structure and function prediction.* Nat Methods, 2015. **12**(1): p. 7-8.
55. Pettersen, E.F., et al., *UCSF Chimera--a visualization system for exploratory research and analysis.* J Comput Chem, 2004. **25**(13): p. 1605-12.
56. Li, W., et al., *Energy landscape and multiroute folding of topologically complex proteins adenylate kinase and 2ouf-knot.* Proc Natl Acad Sci U S A, 2012. **109**(44): p. 17789-94.
57. Li, W., W. Wang, and S. Takada, *Energy landscape views for interplays among folding, binding, and allostery of calmodulin domains.* Proc Natl Acad Sci U S A, 2014. **111**(29): p. 10550-5.
58. Kenzaki, H., et al., *CafeMol: A Coarse-Grained Biomolecular Simulator for Simulating Proteins at Work.* J Chem Theory Comput, 2011. **7**(6): p. 1979-89.
59. Goddard, T.D., et al., *UCSF ChimeraX: Meeting modern challenges in visualization and analysis.* Protein Sci, 2018. **27**(1): p. 14-25.
60. Yanagisawa, H.A., et al., *FAP20 is an inner junction protein of doublet microtubules essential for both the planar asymmetrical waveform and stability of flagella in Chlamydomonas.* Mol Biol Cell, 2014. **25**(9): p. 1472-83.
61. El-Gebali, S., et al., *The Pfam protein families database in 2019.* Nucleic Acids Res, 2019. **47**(D1): p. D427-D432.

Chapter 4: General discussion, summary and conclusion

At the start of my degree, only FAP20 was confirmed as an inner junction protein [33]. During the duration of my thesis, two independent studies were able to identify PACRG as an inner junction protein [34] and FAP52 [7] as the density proximal to the inner junction that lies on PF B10. In the second chapter, I revealed the complete identity of the *Chlamydomonas* inner junction by identifying two previously unknown MIPs, FAP276 and FAP106, as inner junction proteins and another previously unknown MIP, FAP126, as an inner junction-associated protein. The atomic modeling of all such proteins provided new insights into the doublet architecture and the role of the MIPs in the cilia. In the third chapter, I provided new insight on a potential mechanism of how the PF ribbon is stabilized. The identification and the molecular modeling of the two homologs of the Rib43a proteins provide the first atomic models of MIPs. The atomic models revealed that the N-terminus of Rib43a-S bind to the taxane-binding pocket, where taxol and other microtubule stabilizing drugs are known to bind.

In this second chapter, I showed that the inner junction of the doublet is made up of a discontinuous arrangement of FAP20-PACRG heterodimers. I also showed that other inner junction associated MIPs appear to work synergistically from inside the lumen of the B-tubule to strengthen, stabilize and regulate the interactions at the inner junction. FAP52, a WD40 repeat protein, acts as an interaction hub, connecting many MIPs together at the inner junction. Tubulin's interactions with FAP52 itself are mediated by FAP276, which provide support and strong anchorage to the tubulin lattice. FAP126 forms an extensive binding surface with tubulin which further strengthens the inner junction structure by physically linking the A and B-tubules together. FAP106 is a disordered protein that occupies the wedge between PF A12 and A13, which has a 16 nm periodicity alternating with FAP106.

Previous studies showed that microtubules possess certain mechanical properties of flexibility and rigidity, which allow them to function properly inside the cell [61, 62]. The assembly of PACRG-FAP20 as discontinuous heterodimers could be an important factor in maintaining a certain degree of flexibility between the A- and B-tubules. This is further supported by the numerous interaction

nodes at the inner junction, which would provide flexibility and further compensatory means in case of defects or unusual external stresses in the external environment.

The proposed role of FAP52 as an interaction hub is in agreement with previous literature describing WD40 repeat proteins as platforms for protein-protein interactions [63]. Given its structure and interactions, it could also play a role during assembly. However, previous studies showed that Fap52 knockout had a similar phenotype to wild type, making FAP52's role in assembly unlikely or limited in extent. Combining FAP52 and FAP20 knockouts gives more drastic phenotypes as explained in the discussion of the second chapter. This indeed supports that i) MIPs perform their function in a synergistic fashion and ii) the multiple nodes of interactions provide compensatory means in case of defects or changes in the external environment. It also further puts forward a new postulate regarding the function of MIPs in the doublet, which is the modulation of its mechanical properties, rather than maintaining its stability; a conclusion that is often drawn from functional studies such as velocity assays, cilia beat frequency and *in vitro* microtubule sliding assay, all in the absence of atomic structures. Maintaining the stability of the doublet can also be seen as a consequence of possessing the right mechanical properties, which can be attributed to the MIPs.

The mechanism of how and what MIPs stabilize the doublet are unanswered questions to date. The identification and the molecular modeling of the two homologs of the Rib43a proteins revealed an overlap between the N-terminus of Rib43a-S and taxol at the taxane-binding pocket. This raised the hypothesis that the N-terminus of Rib43a-S could have a stabilizing effect on the microtubule similar to taxol. Although this effect remains to be directly tested, this finding could pave the road towards new strategies for taxol alternatives in microtubule-based cancer therapy. In addition, the atomic models of the Rib43a proteins provide direct evidence of a MIP that alters the tubulin lattice architecture by introducing a bimodal distribution of inter-tubulin dimer distances and by altering the conformations of the tubulin molecule itself. These findings support a broader regulatory role of the MIPs that might extend beyond modulating its mechanical properties.

Another conclusion from functional studies linked the mouse homolog of FAP106 (Enkurin) to sperm motility [64]. This conclusion seems valid given FAP106 structure and role discussed in the second chapter. However, the conclusion linking FAP126 to basal body docking and planar cell polarity during cilia formation [65] is not immediately obvious. Given its structure and

localization, FAP106 could play two roles. By wedging between and interacting with the tubulin dimers on the outer surface of the A-tubule, it induces a low curvature angle between PF A12 and A13. It was shown previously that inter-PF curvature angles show great variation between one another [66], which can aid in the assembly and binding of other MIPs inside both of the A- and B- tubules. The second role could be an assembly role by aiding in FAP106 recognition and maintaining both proteins' 16 nm periodicity. The conclusion of that study can then be explained as a further downstream effect of a failure in assembly, rather than any direct effect on the basal body, although it could still be possible, however, it requires further testing.

Furthermore, the interactions of the inner junction proteins revealed new insights on the functional flexible elements of the α- and β-tubulin heterodimer, where post-translational modifications are known to occur. These elements i.e. the α- and β-tubulin and the acetylation K40 loop of α- tubulin were never visualized before in past x-ray crystallography and cryo-EM studies of *in vitro* reconstituted microtubules. These interactions suggest a functional role of post-translational modifications in the assembly and function of the doublet. These findings also highlight the limitations of the previously mentioned techniques, which can result in the loss of functional loops due to their flexibility and or isolation from their native environment. Structure determination in the future would benefit from a hybrid approach between cryo-EM of *ex vivo* structures, which are isolated from the cell and the crystallization of recombinant proteins to ultimately decipher protein function.

It is clear that the architecture of the doublet mandates an orderly assembly of its components and their specific bindings onto the tubulin lattice. The atomic structures of FAP20 and PACRG revealed that they likely form and assemble as a heterodimer. The atomic model of FAP20 shows 3D structure homology to carbohydrate-binding modules, which supports its role as an assembly chaperone. Furthermore, the head-to-tail arrangement of the Rib43a proteins indicate that they might play a role in maintaining the periodicity and registry of the doublet during assembly.

Finally, I want to propose a model to explain the heterogeneity of ciliopathies based on i) the regulatory role of MIPs in modulating the mechanical properties of the cilia and 2) the species-specific adaptations of the doublet. It is known that the length, diameter and number of cilia can vary significantly between tissues and organisms. This suggests that the function of cilia is indeed linked to its gross mechanical properties. This puts forward the hypothesis that the extent of

mechanical defect following the same protein mutation in different tissues or organisms is also a function of the mechanical properties of that type of cilia and the external stresses that it has to work against in that particular environment. This hypothesis could explain how the FAP52 knockout in *Chlamydomonas* produces a phenotype similar to the wild type [7], while the gene deletion of the FAP52 human homolog (WDR16) results in situs inversus, heterotaxy and possible infertility [35]. While this model does not provide immediate answers to explain ciliopathies in general, it does call for an effort to continue working on the structure of the cilia, quantify its mechanical properties and build test models that closely simulate its mechanical properties.

In conclusion, the structure of the inner junction has been a long-standing question in biology [52]. In the second chapter of this thesis, I revealed the complete identity, localization and structure of the *Chlamydomonas* inner junction, thus successfully tackling the first objective of my thesis. Due to the interconnectedness of the doublet structure, which functions as a whole, my first objective expanded into studying other MIPs of the doublet, the α- and β-tubulin heterodimer and the conformations and interactions associated with both. In both the second and third chapter, I successfully tackled the second objective of my thesis by identifying and modeling MIPs at the inner junction and the Rib43a proteins at the PF ribbon, thus providing insight on MIP structure, function and role in doublet architecture and assembly.

References

1. Afzelius, B., *Cilia-related diseases.* The Journal of pathology, 2004. **204**(4): p. 470-477.
2. Fliegauf, M., T. Benzing, and H. Omran, *When cilia go bad: cilia defects and ciliopathies.* Nature reviews Molecular cell biology, 2007. **8**(11): p. 880.
3. Griffiths, G.M., A. Tsun, and J.C. Stinchcombe, *The immunological synapse: a focal point for endocytosis and exocytosis.* The Journal of cell biology, 2010. **189**(3): p. 399-406.
4. Reiter, J.F. and M.R. Leroux, *Genes and molecular pathways underpinning ciliopathies.* Nature reviews Molecular cell biology, 2017. **18**(9): p. 533.
5. Cavalier-Smith, T., *The phagotrophic origin of eukaryotes and phylogenetic classification of Protozoa.* International journal of systematic and evolutionary microbiology, 2002. **52**(2): p. 297-354.
6. Schmid, F., S.T. Christensen, and L.B. Pedersen, *Cilia and Flagella*, in *Encyclopedia of Cell Biology*. 2016, Academic Press: Waltham. p. 660-676.
7. Owa, M., et al., *Inner lumen proteins stabilize doublet microtubules in cilia and flagella.* Nature Communications, 2019. **10**(1): p. 1143.
8. Ichikawa, M. and K.H. Bui, *Microtubule inner proteins: a meshwork of luminal proteins stabilizing the doublet microtubule.* BioEssays, 2018. **40**(3): p. 1700209.
9. Hanske, J., Y. Sadian, and C.W. Müller, *The cryo-EM resolution revolution and transcription complexes.* Current opinion in structural biology, 2018. **52**: p. 8-15.
10. Hryc, C.F., D.-H. Chen, and W. Chiu, *Near-atomic resolution cryo-EM for molecular virology.* Current opinion in virology, 2011. **1**(2): p. 110-117.
11. Grigorieff, N. and S.C. Harrison, *Near-atomic resolution reconstructions of icosahedral viruses from electron cryo-microscopy.* Current opinion in structural biology, 2011. **21**(2): p. 265-273.
12. Zhang, X., et al., *Near-atomic resolution using electron cryomicroscopy and single-particle reconstruction.* Proceedings of the National Academy of Sciences, 2008. **105**(6): p. 1867-1872.
13. Zhang, X., et al., *3.3 Å cryo-EM structure of a nonenveloped virus reveals a priming mechanism for cell entry.* Cell, 2010. **141**(3): p. 472-482.
14. Manuell, A.L. and S.P. Mayfield, *A bright future for Chlamydomonas.* Genome Biology, 2006. **7**(9): p. 327.
15. Eisen, J.A., et al., *Macronuclear genome sequence of the ciliate Tetrahymena thermophila, a model eukaryote.* PLoS Biol, 2006. **4**(9): p. e286.
16. Ibañez-Tallon, I., et al., *Dysfunction of axonemal dynein heavy chain Mdnah5 inhibits ependymal flow and reveals a novel mechanism for hydrocephalus formation.* Human molecular genetics, 2004. **13**(18): p. 2133-2141.
17. Dasgupta, A. and J.D. Amack, *Cilia in vertebrate left–right patterning.* Philosophical Transactions of the Royal Society B: Biological Sciences, 2016. **371**(1710): p. 20150410.
18. Goetz, S.C. and K.V. Anderson, *The primary cilium: a signalling centre during vertebrate development.* Nature reviews genetics, 2010. **11**(5): p. 331.
19. Mitchison, H.M. and E.M. Valente, *Motile and non-motile cilia in human pathology: from function to phenotypes.* The Journal of pathology, 2017. **241**(2): p. 294-309.
20. Vincensini, L., T. Blisnick, and P. Bastin, *1001 model organisms to study cilia and flagella.* Biology of the Cell, 2011. **103**(3): p. 109-130.
21. Shinohara, K., et al., *Absence of radial spokes in mouse node cilia is required for rotational movement but confers ultrastructural instability as a trade-off.* Developmental cell, 2015. **35**(2): p. 236-246.

22. Heuser, T., et al., *The dynein regulatory complex is the nexin link and a major regulatory node in cilia and flagella.* The Journal of cell biology, 2009. **187**(6): p. 921-933.
23. Satir, P., *Studies on cilia: III. Further studies on the cilium tip and a" sliding filament" model of ciliary motility.* The Journal of cell biology, 1968. **39**(1): p. 77-94.
24. Sung, C.-H. and M.R. Leroux, *The roles of evolutionarily conserved functional modules in cilia-related trafficking.* Nature cell biology, 2013. **15**(12): p. 1387.
25. Ishikawa, H. and W.F. Marshall, *Ciliogenesis: building the cell's antenna.* Nature reviews Molecular cell biology, 2011. **12**(4): p. 222.
26. Taschner, M. and E. Lorentzen, *The intraflagellar transport machinery.* Cold Spring Harbor perspectives in biology, 2016. **8**(10): p. a028092.
27. Tokuyasu, K. and E. Yamada, *The fine structure of the retina studied with the electron microscope: IV. Morphogenesis of outer segments of retinal rods.* The Journal of Cell Biology, 1959. **6**(2): p. 225-230.
28. Reiter, J.F., O.E. Blacque, and M.R. Leroux, *The base of the cilium: roles for transition fibres and the transition zone in ciliary formation, maintenance and compartmentalization.* EMBO reports, 2012. **13**(7): p. 608-618.
29. Barr, M.M. and P.W. Sternberg, *A polycystic kidney-disease gene homologue required for male mating behaviour in C. elegans.* Nature, 1999. **401**(6751): p. 386-9.
30. Hildebrandt, F., T. Benzing, and N. Katsanis, *Ciliopathies.* New England Journal of Medicine, 2011. **364**(16): p. 1533-1543.
31. Waters, A.M. and P.L. Beales, *Ciliopathies: an expanding disease spectrum.* Pediatric nephrology (Berlin, Germany), 2011. **26**(7): p. 1039-1056.
32. Horani, A., et al., *Genetics and biology of primary ciliary dyskinesia.* Paediatric respiratory reviews, 2016. **18**: p. 18-24.
33. Yanagisawa, H.-a., et al., *FAP20 is an inner junction protein of doublet microtubules essential for both the planar asymmetrical waveform and stability of flagella in Chlamydomonas.* Molecular biology of the cell, 2014. **25**(9): p. 1472-1483.
34. Dymek, E.E., et al., *PACRG and FAP20 form the inner junction of axonemal doublet microtubules and regulate ciliary motility.* Molecular biology of the cell, 2019. **30**(15): p. 1805-1816.
35. Ta-Shma, A., et al., *A human laterality disorder associated with a homozygous WDR16 deletion.* European Journal of Human Genetics, 2015. **23**(9): p. 1262.
36. Sui, H. and K.H. Downing, *Structural basis of inter-protofilament interaction and lateral deformation of microtubules.* Structure (London, England : 1993), 2010. **18**(8): p. 1022-1031.
37. LeDizet, M. and G. Piperno, *Identification of an acetylation site of Chlamydomonas alpha-tubulin.* Proceedings of the National Academy of Sciences, 1987. **84**(16): p. 5720-5724.
38. Wloga, D., E. Joachimiak, and H. Fabczak, *Tubulin Post-Translational Modifications and Microtubule Dynamics.* International journal of molecular sciences, 2017. **18**(10): p. 2207.
39. Tilney, L.G., et al., *Microtubules: evidence for 13 protofilaments.* The Journal of cell biology, 1973. **59**(2): p. 267-275.
40. Witman, G.B., et al., *Chlamydomonas flagella: I. Isolation and electrophoretic analysis of microtubules, matrix, membranes, and mastigonemes.* The Journal of Cell Biology, 1972. **54**(3): p. 507-539.
41. Peters, A., C.C. Proskauer, and I.R. Kaiserman-Abramof, *The small pyramidal neuron of the rat cerebral cortex: the axon hillock and initial segment.* The Journal of cell biology, 1968. **39**(3): p. 604-619.
42. Echandía, E.R., R. Piezzi, and E. Rodriguez, *Dense-core microtubules in neurons and gliocytes of the toad Bufo arenarum Hensel.* American Journal of Anatomy, 1968. **122**(1): p. 157-167.

43. Burton, P.R., *Luminal material in microtubules of frog olfactory axons: structure and distribution.* The Journal of cell biology, 1984. **99**(2): p. 520-528.
44. Hoops, H.J. and G.B. Witman, *Outer doublet heterogeneity reveals structural polarity related to beat direction in Chlamydomonas flagella.* The Journal of cell biology, 1983. **97**(3): p. 902-908.
45. Nicastro, D., et al., *The molecular architecture of axonemes revealed by cryoelectron tomography.* Science, 2006. **313**(5789): p. 944-948.
46. Sui, H. and K.H. Downing, *Molecular architecture of axonemal microtubule doublets revealed by cryo-electron tomography.* Nature, 2006. **442**(7101): p. 475.
47. Pigino, G., et al., *Comparative structural analysis of eukaryotic flagella and cilia from Chlamydomonas, Tetrahymena, and sea urchins.* Journal of structural biology, 2012. **178**(2): p. 199-206.
48. Ichikawa, M., et al., *Subnanometre-resolution structure of the doublet microtubule reveals new classes of microtubule-associated proteins.* Nature Communications, 2017. **8**(1): p. 15035.
49. Linck, R., et al., *Insights into the structure and function of ciliary and flagellar doublet microtubules: tektins, Ca2+-binding proteins, and stable protofilaments.* The Journal of biological chemistry, 2014. **289**(25): p. 17427-17444.
50. Kirima, J. and K. Oiwa, *Flagellar-associated Protein FAP85 Is a Microtubule Inner Protein That Stabilizes Microtubules.* Cell Structure and Function, 2018. **43**(1): p. 1-14.
51. Stoddard, D., et al., *Tetrahymena RIB72A and RIB72B are microtubule inner proteins in the ciliary doublet microtubules.* Molecular biology of the cell, 2018. **29**(21): p. 2566-2577.
52. Nicastro, D., et al., *Cryo-electron tomography reveals conserved features of doublet microtubules in flagella.* Proceedings of the National Academy of Sciences, 2011. **108**(42): p. E845-E853.
53. Kitada, T., et al., *Mutations in the parkin gene cause autosomal recessive juvenile parkinsonism.* nature, 1998. **392**(6676): p. 605.
54. West, A.B., et al., *Identification of a novel gene linked to parkin via a bi-directional promoter.* Journal of molecular biology, 2003. **326**(1): p. 11-19.
55. Ikeda, T., *Parkin-co-regulated gene (PACRG) product interacts with tubulin and microtubules.* FEBS letters, 2008. **582**(10): p. 1413-1418.
56. Dawe, H.R., et al., *The Parkin co-regulated gene product, PACRG, is an evolutionarily conserved axonemal protein that functions in outer-doublet microtubule morphogenesis.* Journal of cell science, 2005. **118**(23): p. 5421-5430.
57. Wilson, G.R., et al., *Expression and localization of the Parkin co-regulated gene in mouse CNS suggests a role in ependymal cilia function.* Neurosci Lett, 2009. **460**(1): p. 97-101.
58. Lorenzetti, D., C.E. Bishop, and M.J. Justice, *Deletion of the Parkin coregulated gene causes male sterility in the quakingviable mouse mutant.* Proceedings of the National Academy of Sciences, 2004. **101**(22): p. 8402-8407.
59. Wilson, G.R., et al., *Deletion of the Parkin co-regulated gene causes defects in ependymal ciliary motility and hydrocephalus in the quakingviable mutant mouse.* Hum Mol Genet, 2010. **19**(8): p. 1593-602.
60. Thumberger, T., et al., *Ciliary and non-ciliary expression and function of PACRG during vertebrate development.* Cilia, 2012. **1**(1): p. 13.
61. Kasas, S. and G. Dietler, *Techniques for measuring microtubule stiffness.* Current nanoscience, 2007. **3**(1): p. 79-96.
62. Tuszyński, J., et al., *Anisotropic elastic properties of microtubules.* The European Physical Journal E, 2005. **17**(1): p. 29-35.
63. Zhang, C. and F. Zhang, *The Multifunctions of WD40 Proteins in Genome Integrity and Cell Cycle Progression.* Journal of genomics, 2015. **3**: p. 40-50.

64. Jungnickel, M.K., et al., *The flagellar protein Enkurin is required for mouse sperm motility and for transport through the female reproductive tract.* Biol Reprod, 2018. **99**(4): p. 789-797.
65. Gegg, M., et al., *Flattop regulates basal body docking and positioning in mono- and multiciliated cells.* Elife, 2014. **3**.
66. Ichikawa, M., et al., *Subnanometre-resolution structure of the doublet microtubule reveals new classes of microtubule-associated proteins.* Nature Communications, 2017. **8**: p. 15035.